Low-pressure Metamorphism in the Ryoke Metamorphic belt in the Yanai District, Southwest Japan

A Dissertation submitted to the Hiroshima University for the degree of Doctor of Science

Takamoto OKUDAIRA

Institute of Geology and Mineralogy, Faculty of Science, Hiroshima University, Higashi-Hiroshima 739, Japan

September 1995

ACKNOWLEDGEMENTS

i

ABSTRACT

The Ryoke metamorphic belt is one of the typical low-pressure type metamorphic belts in the world. It is composed of granitoids (Older and Younger Ryoke granitoids) and their associated metamorphic complex (Ryoke metamorphic rocks) of Cretaceous age. The Ryoke metamorphic rocks in the Yanai district, southwest Japan, show three different phases of ductile deformation. During the first phase (D1), a distinct foliation parallel to lithologic layering was formed under the thermal peak conditions of the low-pressure facies series metamorphism, which is probably ascribed to the sheet-like intrusion of the Older Ryoke granitoids. The second phase deformation (D2) led to the formation of mylonitic shear zones and nappes. Deformation of the third phase (D3) was responsible for the formation of the upright folds with E-W trending axes. In the metamorphic rocks of the Tsuzu area, which is placed in the northern part of the Yanai district, there are many melt-filled fractures of minor scales, which cut across their foliation. The deformation related to the formation of these melt-filled fractures resulted commonly from foliation parallel shearing under extensional stress field. The overall movement picture inferred from the melt-filled fractures appears to be top to the N sense of shear, and the deformation related to the formation of the melt-filled fractures was responsible for the formation of the normal fault zones, along which the intrusion of the Older Ryoke granitoids occurred. Asymmetric textures such as extensional crenulation cleavage and rotation of porphyroblasts, which grew under the thermal peak of M1, are also formed in the metapelites. The shear sense read from the asymmetric textures is the top to the north. This is harmonic with the overall movement picture inferred from the melt-filled fractures. Therefore it can be said that the overall movement picture of D1 during and immediately before the intrusion of the Older Ryoke granitoids was of extension tectonics. As inferred from the dislocation densities in quartz grains deformed during D1, strain rate for D1 appears to be high ($\approx 10^{-10} \sim 10^{-7}$ s^{-1}). After D1, the nappes and upright folds of the metamorphic rocks and granitoids were formed during D2 and D3 probably under compressional stress field.

The regional Ryoke metamorphism has been divided into two phases, M0 and M1. The metamorphism of M0 was of nearly medium-pressure facies series ($ca.$ 30°C / km) and that of

M1 was of low-pressure facies series (*ca.* 40 ~ 50°C / km). On the basis of the mineral assemblages crystallized under M1, the Ryoke metamorphic rocks are divided into four metamorphic zones: biotite zone, cordierite zone (460 ~ 590°C, 2.5 ~ 3.5 kbar), sillimanite zone (630 ~ 690°C, 3 ~ 5 kbar), and garnet zone (730 ~ 770°C, 5.5 ~ 6.5 kbar). Because the intrusion of the Older Ryoke granitoids has a strong time and spatial association with M1, it is suggested that the heat sources of M1 are the emplacement of the Older Ryoke granitoids. By using 1-D numerical simulation, the thermal model for M1 was developed by heat conduction with fluid advection caused by intrusion of a granodiorite sheet at intermediate crustal levels. The calculated temperature-time path (*T*-*t* path) for the sillimanite zone during M1 is characterized by a rapid increase of temperature, 0.0017°C / year on average, and a short-period of high-temperature condition (> 600°C), shorter than 0.5 Ma. The results of the thermal model nearly consist with the petrologically estimated highest metamorphic temperatures during M1.

Garnet crystals from the sillimanite zone are chemically zoned and show several kinds of zoning patterns. The patterns systematically vary with grain size, which are between *ca.* 0.1 and 0.5 mm in radius. Large grains (> *ca.* 0.4 mm) show normal zoning and small grains (< *ca.* 0.4 mm) show unzoned or reversely zoned profile in their cores. Observations of the chemical zoning and of the spatial and size distributions of the garnets between *ca.* 0.1 and 0.5 mm in radius suggest that the garnets have been formed by continuous nucleation and diffusion-controlled growth. To examine the validity of the *T*-*t* path for M1, the chemical zonings of garnets with different radii are simulated for the *T*-*t* path using a numerical model of continuous nucleation and diffusion-controlled growth, in combination with intracrystalline diffusion, and are compared with the observed ones. The observed overall zoning patterns in the garnets with different radii are well reproduced by the numerical model, in spite of the fact that the simulated zoning patterns greatly change responding to the subtle changes in the *T*-*t* history. Therefore, these results suggest that the *T*-*t* path gives a good explanation for M1. Therefore, it can be said that the sheet-like Older Ryoke granitoids intruded at intermediate crustal levels (≈ 15-km-depth) are a heat source of M1. In conclusion, the Ryoke metamorphic rocks firstly were heated under medium-pressure facies conditions, and then they were further

heated under low-pressure facies conditions caused by the intrusion of the Older Ryoke granitoids.

CONTENTS

Evolution of the continental crust is a central question of the earth science. In general, active continental margins are composed of granitoids and their associated low-pressure type metamorphic complex (Fig. 1.1: e.g. Miyashiro, 1961, 1994). The granitoids and low-pressure type metamorphic rocks commonly form low-pressure type metamorphic belt (LPM) in the world (Fig. 1.2). To clarify the evolution of the continental crust, it is necessary that the formation processes of LPM are considered especially with reference to two aspects such as a) emplacement mechanism of the granitic magma and b) thermal evolution of the metamorphic rocks as described bellows.

Emplacement mechanism of a granitic magma

Because granitoids are commonly intrusion bodies of large volumes, their emplacement mechanisms have so far been discussed by many authors as so-called "space problem" (e.g. Paterson *et al.*, 1991). Traditionally two main emplacement mechanisms have been emphasized: 1) forceful intrusion, whereby buoyancy-driven magmas physically push the crust aside, giving rise to granitic diapirs and balloons (e.g. Brun and Pons, 1981; Sakurai *et al.*, 1983; Bateman, 1985; Ramsay, 1989); and 2) passive emplacement related to tectonic cavity opening such as great fault and cauldron subsidence with stoping (e.g. Bussell *et al.*, 1976; Pitcher, 1979; Bouchez and Diot, 1990). Furthermore, Guineberteau *et al.* (1987), Hutton (1982), Toyoshima and Hara (1989), Hutton *et al.* (1990), and Shimura (1992) have suggested that granitic magma intruded in the spaces created by transcurrent fault, extensional shear zone, subhorizontal fracture zone, and large-scale detachment fault, respectively. Hutton (1988) suggested that the emplacement mechanism (forceful or passive) depends on the ratio between the rate of buoyant uprise of magma and that of tectonic cavity opening. In the Ryoke metamorphic belt of Japan, Hara *et al.* (1991) and Okudaira *et al.* (1992, 1993) suggested that the Older Ryoke granitoids appear to have intruded as sheet-like intrusions along northward dipping large-scale fracture zones oriented at low angles. While Hayashi (1994) suggested that the Hiroshima granitoids in the Togouch-Yuu-Takehara district, which are shallow facies of the

Ryoke granitoids and have the N-S dimension of *ca.* 50 km on the ground surface, appear to be related to "lateral magma movement" along shallow shear zone with low angle dip. Sakurai *et al.* (1983) indicated that the Younger Ryoke granitoid as stock-like body intruded forcefully based on the structural analysis of related rocks.

Thermal evolution of a low-pressure type metamorphic belt

LPM found in the world is formed under such *P-T* conditions that the pressure is lower than that of the aluminosilicate triple point (about 4 kbar), and the peak temperature ranges between 500 and 700°C (cf. Miyashiro, 1961, 1994; De Yoreo *et al.*, 1991; Spear, 1993 Takeshita and Okudaira, 1994)). Such anomalously high temperatures at relatively shallow depth indicate that the geothermal gradient in the upper crust exceed 50°C km^{-1} at the time of LPM formation. Many processes can generate a low-pressure metamorphism (cf. De Yoreo *et al.*, 1991; Takeshita and Okudaira, 1994). Recent suggestions for the heat sources of low-pressure metamorphism include crustal extension (Wickham and Oxburgh, 1985, 1987), convective thinning of mantle lithosphere (Spohn and Schubert, 1982; Loosveld, 1989a, b), subduction of young oceanic plate or spreading ridge (DeLong *et al.*, 1979; Takeshita and Komatsu, 1990), rapid uplift of doubled continental crust (England and Thompson, 1984; Thompson and England, 1984), increased heat flux at the base of the crust (Oxburgh and Turcotte, 1971), and advective heat transport by hot aqueous fluids (Ferry, 1983, 1986; Hoisch, 1987). However, geologists have recognized a spatial and temporal association of low-pressure metamorphic belts with magmatic arc terranes (cf. Miyashiro, 1961, 1994; Zwart, 1967; De Yoreo *et al.*, 1991). Numerical simulations of the thermal evolution of magmatic arc terranes show that the magmatism can produce regionally extensive belts of low-pressure metamorphism (e.g. Wells, 1980; Lux *et al.*, 1986; Barton and Hanson, 1989; Hanson and Barton, 1989; De Yoreo *et al.*, 1989; Okudaira *et al.*, 1994; Rothstein and Hoisch, 1994).

The Ryoke metamorphic belt of southwest Japan (see Fig. 1.3a) is mainly composed of a large volume of Cretaceous granitoids (Ryoke granitoids) and their associated low-pressure type metamorphic rocks (Ryoke metamorphic rocks), and then has been regarded as a typical example of low-pressure type metamorphic belts. The low-pressure Ryoke metamorphic belt is adjacent to the high-pressure Sambagawa metamorphic belt, separated by the Median Tectonic

2

Line (MTL), in southwest Japan and both are of Jurassic-Cretaceous age (e.g. Hara *et al.*, 1992; Banno and Nakajima, 1992; Nakajima, 1994). The Ryoke granitoids have been divided into sill-like granitoids (Older Ryoke granitoids) and stock-like ones (Younger Ryoke granitoids) on the basis of their intrusion forms (e.g. Hara, 1962; Hara *et al.*, 1980, 1991; Okudaira *et al.*, 1993). Many geological observation, as described in the following paragraphs, indicates that the low-pressure facies series Ryoke metamorphism has a strong spatial and time association with emplacement of the Older Ryoke granitoids.

1) Distribution of the Older granitoids correlates with that of the high-grade metamorphic rocks (e.g. Suwa, 1973; Okudaira *et al.*, 1993).

2) Throughout the higher grade metamorphic zones, distinct contact aureoles caused by the intrusion of the Older granitoids are lacking (e.g. Koide, 1958; Nishimura *et al.*, 1985; Nureki *et al.*, 1992).

3) Isograds of the low-pressure type metamorphism are roughly parallel to the boundaries of the Older granitoids (e.g. Ishioka, 1974; Kutsukake, 1977; Okudaira *et al.*, 1993).

4) Geological and petrological structures of the high-grade metamorphic rocks are compatible with those of the Older granitoids (e.g. Koide, 1958; Okamura, 1960; Nureki, 1960; Hara, 1962; Hara *et al.*, 1991; Okudaira *et al.*, 1993).

5) The formation of the low-grade metamorphic rocks related to crystallization of sillimanite is of the same generation as the intrusion of the Older granitoids (Hara, 1962).

6) Radiometric ages of the metamorphic rocks are roughly compatible with those of the Older granitoids (e.g. Shigeno and Yamaguchi, 1976; Banno and Nakajima, 1992; Nakajima, 1994).

Judging from the above-mentioned observations, some literatures (e.g. Ishioka, 1974; Kutsukake, 1977; Okudaira *et al.*, 1993, 1994; Miyashiro, 1994) have suggested that the Older Ryoke granitoids are syn-metamorphic intrusions and the low-pressure facies series Ryoke metamorphism was resulted form thermal effects of the emplacement of the Older granitoids. In order to clarify this suggestion, the author firstly investigated the tectonic conditions which is probably related to emplacement of the Older granitoids and the low-pressure facies series metamorphism of the Ryoke metamorphic belt in the Yanai district. Secondly, the author tried

3

to make a thermal model using simple 1-D numerical simulation for the low-pressure facies series Ryoke metamorphism, because quantitative modeling of the thermal regime is a powerful tool in the investigation of the genesis and evolution of regional metamorphism (e.g. Furlong *et al.*, 1991; Peacock, 1991; Takeshita and Okudaira, 1994). However, thermal model of regional metamorphic terranes is not panacea for the interpretation of complex petrologic signatures, but when appropriately applied it can prove important constraints (De Yoreo *et al.*, 1991; Furlong *et al.*, 1991; Peacock, 1991). Thus, it is necessary that an evaluation of validity of the thermal model is examined by petrological, geophysical, and geochemical studies. Therefore, I present chemical zoning profile in garnets from the Ryoke metamorphic rocks in the Yanai district, and compare them with numerically simulated zoning pattern of garnets to examine of the validity of the thermal modeling for M1. Then, the temperature-time path (T-t path) of the low-pressure facies series Ryoke metamorphism will be examined. Finally, thermal evolution of the Ryoke metamorphic belt will be discussed.
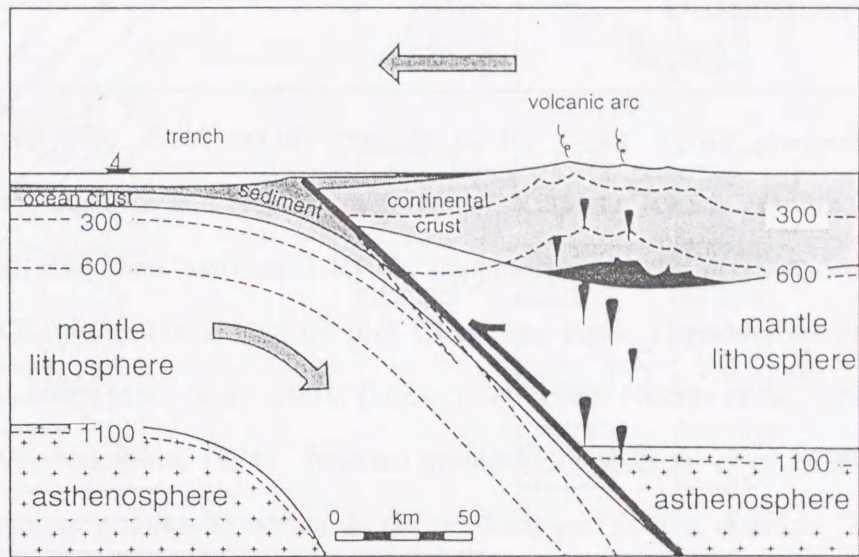
Fig. 1.1. A schematic cross section of an active continental margin. Isotherms are bowed downward in the subduction zone because cool oceanic lithosphere is being subducted. Isotherms in the arc are bowed upward because of the advection of heat by rising magmas. From Ernst (1976).
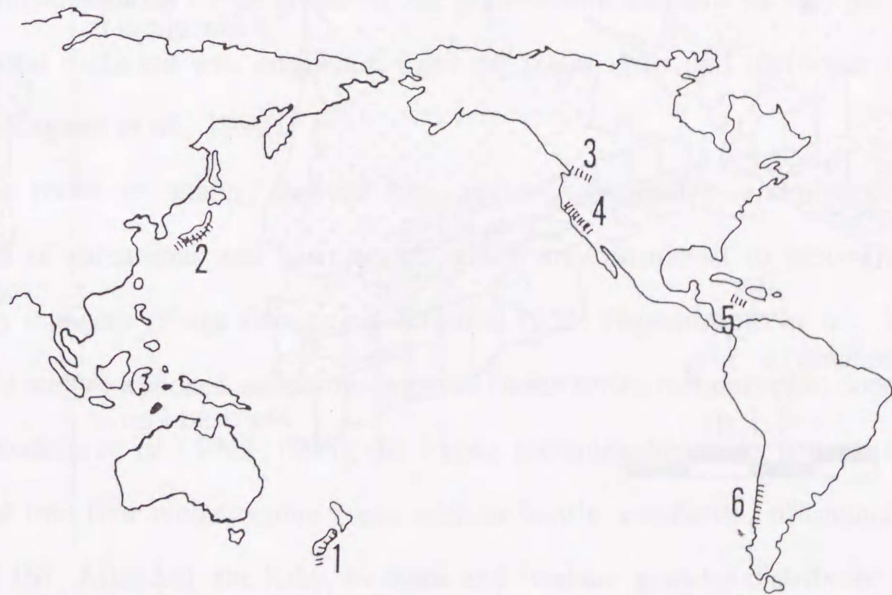
Fig. 1.2. Some of the paired metamorphic belts in the circum-Pacific regions (partly modified from Miyashiro, 1994). 1: Wakatipu and Tasman belts in New Zealand. 2: Sambagawa and Ryoke belts in southwestern Japan. 3: Shuksan and Skagit belts in Washington, USA. 4: Franciscan and Sierra Nevada in California, USA. 5: Mt. Hibernia and Westphalia belts in Jamaica. 6: Pichilemn and Curepto belts in Chile.
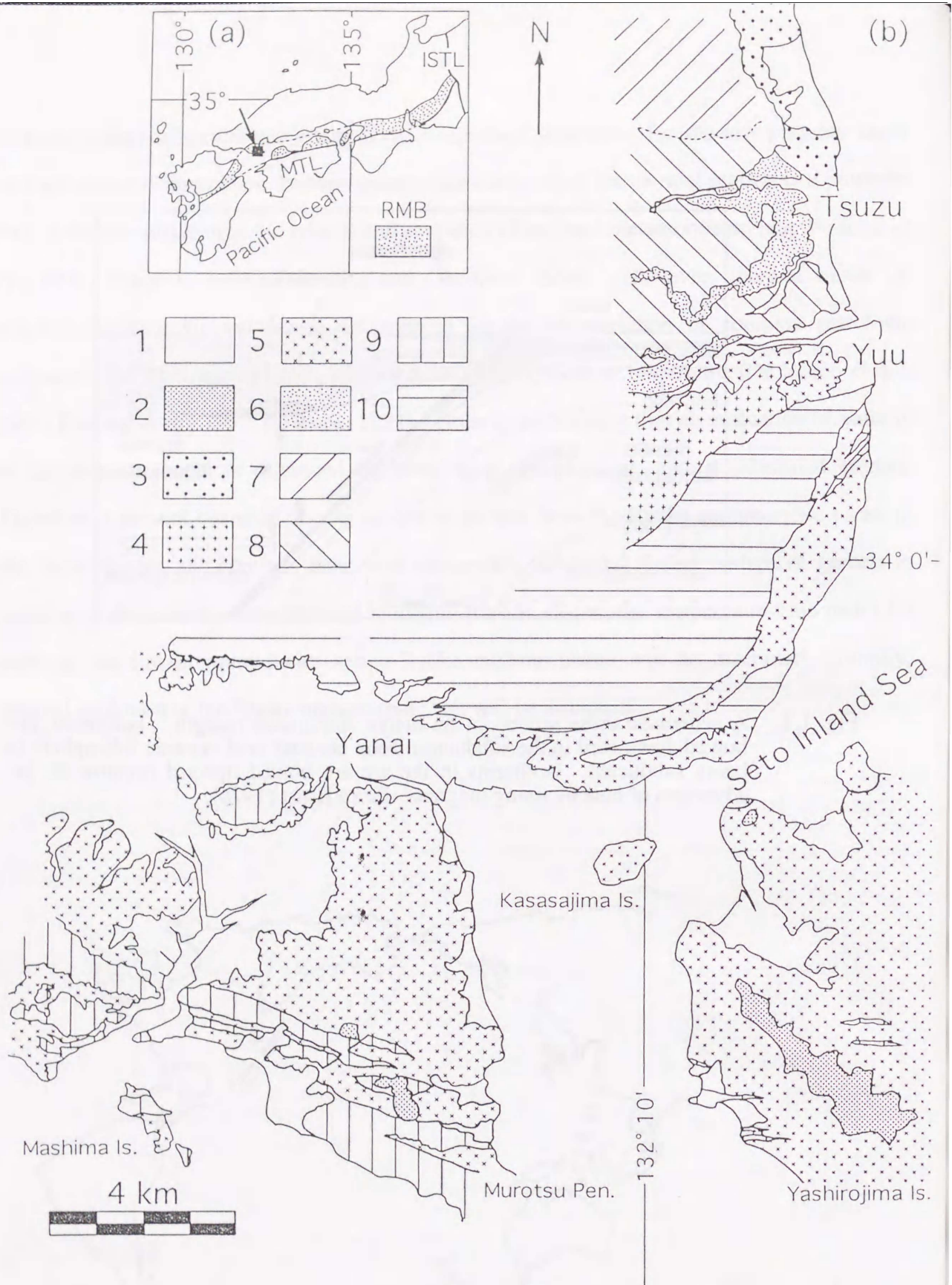
Fig. 1.3. (a) Outline map showing the location of the Ryoke metamorphic belt of southwest Japan. RMB: Ryoke metamorphic belt. MTL: Median Tectonic Line. ISTL: Itoigawa-Shizuoka Tectonic Line. (b) Geological and metamorphic zonation map of the Yanai district, southwest Japan. 1: alluvium. 2: Tertiary volcanics. 3: Hiroshima granitoids. 4: Younger Ryoke granitoids. 5: Older Ryoke granitoids. 6: agmatic migmatite zone. 7 - 10 : Ryoke metamorphic rocks (7 biotite zone, 8 cordierite zone, 9 sillimanite zone, 10 garnet zone).

The Yanai district (Fig. 2.1b) mainly consists of the Older Ryoke granitoids (Gamano granodiorite and Tengatake and Nagano migmatites), Younger Ryoke granitoids (Kibe and Namera granites), and their associated Ryoke metamorphic rocks of Cretaceous age (e.g. Nureki, 1960; Okamura, 1960; Kojima and Okamura, 1968; Higashimoto *et al.*, 1983; Nishimura *et al.*, 1985; Hara *et al.*, 1991; Ikeda, 1991, 1993; Nureki *et al.*, 1992; Okudaira *et al.*, 1993, 1995; Nakajima, 1994). Iwakuni granite (Higashimoto *et al.*, 1983), which is one of the Hiroshima granitoids, occurs in the northern part of the district. The Gamano granodiorite most widely occurs in the district, and is mainly composed of hornblende-biotite tonalite and hornblende-bearing biotite tonalite and granodiorite. The Gamano granodiorite concordantly intruded in the high-grade metamorphic rocks, and its foliation defined by preferred shape orientation of plagioclase, biotite, and hornblende is harmonic in trend with that of the metamorphic rocks. Because the mineralogical and chemical features of the Gamano granodiorite are of metaluminous I-type granitoid, the granodiorite was not *in situ* generated from the middle crustal rocks but was originated from the lower crust and the upper mantle (e.g. Honma, 1974; Kagami *et al.*, 1992).

The metamorphic rocks are mainly derived from pelites, psammites, and cherts, with subordinate amounts of calcareous and basic rocks, which are considered to belong to the Jurassic accretionary complex (Kuga Group: e.g. Kojima, 1953; Higashimoto *et al.*, 1983). They were regionally metamorphosed under low-pressure facies series metamorphic conditions (M1). Following Okudaira *et al.* (1993, 1995), the Ryoke metamorphic rocks formed during M1 has been divided into four metamorphic zones such as biotite, cordierite, sillimanite, and garnet zones (Fig. 2.1b). After M1, the Kibe, Namera, and Iwakuni granites distributed in the north of the studied area (Fig. 2.1b) locally metamorphosed the surrounding rocks (M2).

2.1: Large-scale structures and deformation events

2.1.1: Large-scale structures

On the basis of the features of the large-scale structures, the Ryoke metamorphic belt in the district can be divided into three structural domains such as northern, central and southern domains (Okudaira *et al.* 1993) (Fig. 2.2). The geological structure of the northern domain is characterized by gentle upright folds with a fold axis gently plunging toward ESE (Fig. 2.2). The Tengatake and Nagano migmatites are placed in the northern domain, and intruded cutting across the lithologic layering and foliation in the metamorphic rocks at low angles and across the lower level of lithostratigarphy toward the north (Fig. 2.1b). The geological structure of the southern domain is also characterized by gentle folds in upright fashion and of WNW-ESE to E-W trend (Fig. 2.2). The geological structure of the central domain is characterized by overturned folds which axial surfaces gently dipping toward NNE ~ NE, and therefore significantly differs from that of the northern and southern domains (Fig. 2.2). The Gamano granodiorite intruded in the central and southern domains (Fig. 2.1b). The Gamano granodiorite and the metamorphic rocks of the sillimanite and garnet zones are involved in the overturned folds. When the overturned folds are unfolded to flat-lying state, the Gamano granodiorite is underlain by the metamorphic rocks of the garnet zone, while the former is overlain by the latter of the sillimanite zone (Okudaira *et al.*, 1993). It can be said that the Gamano granodiorite intruded between the garnet and sillimanite zones as sheet-like body.

2.1.2: Deformation events

In the Gamano granodiorite and metamorphic rocks, deformation structures produced during three different phases (D1, D2, and D3) of ductile deformation have been recognized (Okudaira *et al.*, 1993, 1995). D1 and D3 are of the penetrative type, and D2 is of non-penetrative type. A distinct foliation (S1-foliation) parallel to lithologic layering is recognized in all the rocks. Many intrafolial folds (F1-folds) with axial plane parallel to S1-foliation and rotated and non-rotated boudinages are recognized (Fig. 2.3). In the biotite zone, extensional crenulation cleavage (ECC) are also recognized. ECC is considered to be formed under a foliation-parallel extension with some non-coaxial components (e.g. Platt and Vissers, 1980). The composition of ECC-forming biotite coincides with that of S1-forming biotite, the ECC occurred simultaneously with S1-foliation. The S1-foliation and ECC are comparable with Y and R_1 of

Riedel shear fractures, respectively, and then the shear sense inferred from the geometrical relationship between the ECC and S1-foliation is top to the N ~ NNE (Okudaira *et al.*, 1995). The Gamano granodiorite intruded into large-scale extensional fracture zones produced during D1 (Okudaira *et al.*, 1995). In the Gamano granodiorite, S1-foliation defined by shape preferred orientation of plagioclase, biotite, and hornblende are recognized, and general trend of S1-foliation of the Gamano granodiorite is harmonic with that of the metamorphic rocks. D1 is considered to have occurred during M1, while D2 and D3 phases postdate the main crystallization of metamorphic minerals during M1 (Hara *et al*, 1991; Okudaira *et al.*, 1993, 1995). D2 is related to the formation of the overturned folds and basal shear zones in the central domain. The metamorphic rocks and Gamano granodiorite involved in the overturned folds is considered to form a nappe (Hara *et al.*, 1991; Okudaira *et al.*, 1993). The D2-shear zones are recognized as fine-grained layers with distinct foliation (S2) truncating the S1-foliation of the coarse-grained granodiorite (Fig. 2.4). The fine-grained layers consist of new grains produced by dynamic recrystallization of constituents of the coarse-grained granodiorite (Sakurai and Hara, 1990). Asymmetric structures of D2 in the shear zones, as shown in Fig. 2.4, indicate shear sense of top to the WSW ~ SW. D3 is responsible for the formation of the upright folds with E-W trending axes. The upright folds (F3-folds) are comparable with the upright folds developed in left-hand fashion throughout the Paleozoic-Mesozoic accretionary complexes and the Ryoke metamorphic belt in the Inner Zone of southwest Japan (e.g. Hara *et al.*, 1980).

2.2: Regional metamorphism

2.2.1: Low-pressure facies series metamorphism (M1)

Regional metamorphic zonation of the Ryoke metamorphic rocks in the Yanai district has been proposed by many authors (Nureki, 1960; Higashimoto *et al.*, 1983; Nishimura *et al.*, 1985; Ikeda, 1991, 1993; Nureki *et al.*, 1992; Okudaira *et al.*, 1993; Nakajima, 1994). However, the proposed metamorphic zonation slightly differs from each other. In Okudaira *et al.*, (1993, 1995) and this study, on the basis of mineral parageneses of the matrix-forming minerals in pelitic and psammitic rocks, that is, except for cherts and metasomatized rocks, the Ryoke

metamorphic rocks are divided into four metamorphic zones such as biotite, cordierite, sillimanite, and garnet zones. The distribution of those zones are shown in Fig. 2.1b. The biotite and cordierite zones, the sillimanite zone, and the garnet zone are equivalent to the northern, southern, and central structural domains, respectively (see Figs. 2.1b and 2.2). The constituent phases of the pelitic and psammitic rocks are schematically shown in Fig. 2.5, and the critical mineral parageneses, which are occurred as matrix-forming minerals, are as follows:

biotite zone: biotite + muscovite,

cordierite zone: biotite + muscovite + K-feldspar + cordierite ± andalusite,

sillimanite zone: biotite + K-feldspar + sillimanite + garnet or cordierite,

garnet zone: biotite + K-feldspar + cordierite ± garnet.

The first appearance of K-feldspar and cordierite defines the start of the cordierite zone. Andalusite occurs in northern part of the cordierite zone, but sillimanite always mantled by cordierite is often found within and near the Tengatake and Nagano migmatites (Seo, 1987; Okudaira *et al.*, 1993, 1995). Garnet crystals have not been found in metapelites of the biotite and cordierite zones, whereas Ikeda (1991, 1993) reported garnet crystals in metacherts and metapelites of the zones. The sillimanite zone is defined by occurrence of sillimanite as only stable aluminosilicate mineral in matrix. Garnet is often found but does not coexist with cordierite in the rock of the sillimanite zone. The garnet zone is defined by paragenesis of garnet + cordierite. In the garnet zone, sillimanite is not recognized as matrix mineral, but is recognized as inclusion within cordierite porphyroblasts. In the sillimanite and garnet zones, muscovite is not a stable mineral, and is recognized as retrograde mineral.

Textural features observed in pelitic and psammitic rocks of the cordierite and garnet zones are indicative of some prograde metamorphic reactions. In the cordierite zone, cordierite and K-feldspar usually occur as porphyroblast. The cordierite and K-feldspar porphyroblasts mainly include biotite, muscovite, and quartz, which show distinct alignment, as S0-foliation (Fig. 2.6). The S0-foliations within the cordierite porphyroblasts are commonly parallel to S1-foliation, while the S0-foliations within the K-feldspar porphyroblasts are not commonly

parallel to S1-foliation (Fig. 2.6). The occurrences of biotite, muscovite, and quartz within cordierite and K-feldspar porphyroblasts indicate the following prograde reaction (Massonne and Schreyer, 1987):

$$\text{biotite + muscovite + quartz = cordierite + K-feldspar} + H_2O. \tag{2.1}$$
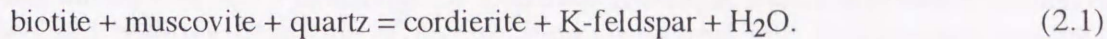
The prograde P-T path of the cordierite zone probably intersects reaction (2.1).

In the garnet zone, cordierite and garnet occur as porphyroblasts. The cordierite porphyroblasts mainly include biotite, quartz, and sillimanite with small amount of hercynite [Fe / (Fe + Mg + Zn): X_{Fe} = 0.70 ~ 0.83] and garnet ($Alm_{76}Pyp_{11}Sps_{11}Grs_2$), showing faint alignment, as S0-foliation which is parallel to S1-foliation (Fig. 2.7a). The garnet porphyroblasts contain quartz, graphite, ilmenite, and biotite, which show no distinct alignment and do not seems to have subjected to any rotation (Fig. 2.7b). These texture is interpreted to have been produced by a high temperature-low pressure static reaction near pluton (Amato *et al.*, 1994). The occurrences of biotite, sillimanite, and quartz within the cordierite porphyroblasts indicate the following prograde reactions:

$$\text{biotite + sillimanite + quartz = cordierite + K-feldspar} + H_2O. \tag{2.2a}$$
$$\text{biotite + sillimanite + quartz = cordierite + K-feldspar + garnet} + H_2O, \tag{2.2b}$$
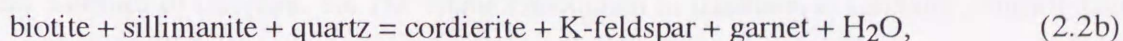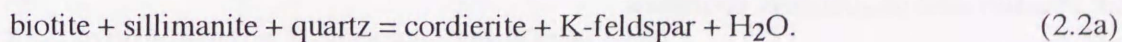
where reactions (2.2a) and (2.2b) are divariant and univariant reactions, respectively (Holdaway and Lee, 1977). The prograde P-T path of the garnet zone probably intersects univariant reaction (2.2b). Hercynite included within cordierite porphyroblasts indicates high-Zn component of (Zn / (Fe + Mg + Zn): X_{Zn} = 0.05 - 0.18. The Zn-rich hercynite has been considered to be a breakdown product of staurolite, because staurolite may be a direct precursor of Zn-rich hercynite (Loomis, 1972; Atkin, 1978; Stoddard, 1979). Although staurolite has not been found in the Yanai district, staurolite as inclusion within biotite and andalusite porphyroblasts has been reported in the Mikawa Plateau (Hazu - Hongu-san area), Aichi

11

Prefecture, central Japan (e.g. Asami, 1971, 1977; Asami and Hoshino, 1980; Seo *et al.*, 1981).

2.2.2: Pre-M1 metamorphism (M0)

Some relict minerals as evidence of pre-M1 have been recognized in a few metapelitic xenoliths of the Tengatake and Nagano migmatites (Fig. 2.8). The xenoliths mainly consist of plagioclase (An_{24-38}), K-feldspar, biotite, muscovite, and cordierite, with a small amount of sillimanite, corundum, Zn-rich hercynite ($X_{Fe} = 0.39 - 0.63$, $X_{Zn} = 0.27 - 0.5$), and garnet (core, $Alm_{69}Pyp_{15}Sps_{14}Grs_2$; rim, $Alm_{66}Pyp_9Sps_{22}Grs_3$). Corundum, sillimanite, Zn-rich hercynite, garnet, and biotite with large grain size are considered to be relict minerals because of their dissolved grain shapes and their grain sizes much greater than other minerals. The other minerals such as plagioclase, K-feldspar, and biotite with small grain size, as well as muscovite and cordierite, correspond with the mineral assemblage crystallized under M1 of the cordierite zone, though quartz is lacking. It can be said that the relict minerals in the xenoliths probably are products of pre-M1 metamorphism (M0) and the xenoliths were re-equilibrated under M1 conditions (Okudaira *et al.*, 1993).

2.2.3: Pressure and temperature estimates

Matrix-forming minerals crystallized in metapelites under M1 are analyzed to estimate the *P-T* conditions for the thermal peak of M1. Garnet-biotite (Thompson, 1976; Holdaway and Lee, 1977; Perchuk, 1977) and two feldspar (Stormer, 1975; Stormer and Whitney, 1977; Haselton *et al.*, 1983) geothermometers are used for temperature estimate, and garnet-cordierite (Aranovich and Podlesskii, 1983) and garnet-aluminosilicate-quartz-plagioclase (GASP: Powell and Holland, 1988) geobarometers are used for pressure estimation. In high-grade metamorphic zones, it is one of difficult works to clarify paragenetic relations between metamorphic minerals in a rocks. The garnets with small grain size (radius: $r < ca.$ 0.4 mm) of the sillimanite zone and almost of garnets of the garnet zones show chemical zoning which consists of unzoned core and reverse zoned rim (Okudaira *et al.*, 1993; Okudaira, 1995a). The composition of unzoned core probably crystallized near the peak metamorphic conditions, while

the that of reverse zoned rim was re-equilibrated during retrograde metamorphism (Okudaira, 1995a). While biotite, cordierite, and plagioclase show no compositional zoning within them. However, biotite shows the variation in Ti content from grain to grain within one thin section (Ikeda, 1991). Ikeda (1991) has suggested that biotite with low-Ti content was synchronously associated with the formation of reverse zoning in garnet during retrograde metamorphism. Therefore, the peak P-T conditions in the sillimanite and garnet zones may be estimated by using the compositions of the unzoned core of garnet and those of biotite, which is not in contact with the garnet and have high Ti contents, cordierite, and plagioclase. The P-T values estimated from the used thermometers and barometers are given in Tables 2.1, 2.2, and 2.3. As inferred from the mineral paragenesis of the cordierite zone, reaction (2.1) curve represents the lower limit of the P-T field of the cordierite zone (Fig. 2.9). Moreover, because aluminosilicate occur as andalusite in the northern part of the cordierite zone, the P-T field of the cordierite zone probably places in the andalusite stability field (Fig. 2.9). Reaction (2.2b) curves represents the upper and lower limits of the P-T fields of the sillimanite and garnet zones, respectively. Because muscovite is a unstable mineral in the sillimanite and garnet zones, the lower limit of the P-T fields of the zones is defined as following reaction:

muscovite + quartz = K-feldspar + sillimanite + H_2O. (2.3)
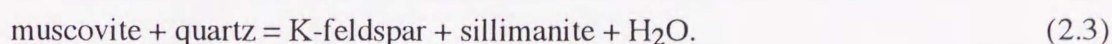
Since muscovite is a stable mineral in the cordierite zone, reaction (2.3) represents the upper limit of the P-T field of the zone (Fig. 2.9).

For the metapelitic xenoliths in the Tengatake and Nagano migmatites, the P-T conditions of M0 are inferred from the core compositions of the relict minerals by using corundum-garnet-sillimanite-spinel geobarometer (Bohlen *et al.*, 1986) and garnet-biotite geothermometers (Thompson, 1976; Holdaway and Lee, 1977; Perchuk, 1977). The pressure and temperature estimated by the relict minerals are *ca.* 6±1 kbar and 700±50°C, respectively (Okudaira *et al.*, 1993). The P-T conditions are comparable with those for a medium-pressure facies series metamorphism (*ca.* 30°C km^{-1}: cf. Miyashiro, 1961, 1994; Spear, 1993). In contrast, the retrograde temperature estimation for the relict garnet rim and matrix-forming biotite have been

calculated to be 530 ~ 560°C by using the garnet-biotite geothermometers (Thompson, 1976; Holdaway and Lee, 1977; Perchuk, 1977) (Okudaira *et al.*, 1993). As mentioned above, the other minerals such as plagioclase, K-feldspar, biotite with a small size, muscovite, and cordierite correspond with the mineral assemblage of the cordierite zone during M1, and their estimated temperatures are comparable with the peak temperatures of the cordierite zone (460 ~ 590°C). Therefore, it is clear that M0 for the xenoliths predates M1. Since the rim of the relict garnet at least was re-equilibrated with the matrix-forming minerals at M1, the pair of the relict garnet rim and the matrix-forming cordierite can estimate the pressure of the cordierite zone at M1. The estimated pressure is estimated to be ca. 2.5 ~ 3.5 kbar by using garnet-cordierite geobarometer (Aranovich and Podlesskii, 1983) (Okudaira *et al.*, 1993).

In summary, the metamorphic *P-T* conditions of the cordierite zone, sillimanite zone, and garnet zone are 460 ~ 590°C at 2.5 ~ 3.5 kbar, 630 ~ 690°C at 3 ~ 5 kbar, and 730 ~ 770°C at 5.5 ~ 6.5 kbar, respectively. The *P-T* fields of the cordierite, sillimanite, and garnet zones are also illustrated in Fig. 2.9. This figure illustrates that the estimated metamorphic temperature continuously increases from the cordierite zone, through the sillimanite zone, to garnet zone. The metamorphic field gradient is *ca.* 40 ~ 50°C km^{-1}, which is comparable with that for the typical low-pressure facies series metamorphism (cf. Miyashiro, 1961, 1994; Spear, 1993).

Table 2.1. *P-T* estimates for the cordierite zone. Methods for *P-T* estimation are as follows: T1 = Stormer (1975); T2 = Stormer and Whitney (1977); T3 = Haselton *et al.* (1983).

| Sample no. | X_{Na}^{Pl} | X_{Ca}^{Pl} | X_{Na}^{Kfs} | X_{K}^{Kfs} | T (P = 3.0 kbar) | | |
					T1	T2	T3
Z-51	0.743	0.249	0.090	0.909	445	490	425
F-8	0.749	0.236	0.133	0.865	503	553	501
E-23	0.732	0.258	0.120	0.878	491	539	485
E-7	0.737	0.251	0.156	0.842	535	589	546
S-1	0.807	0.183	0.161	0.830	517	573	509
F-11	0.610	0.379	0.142	0.856	566	616	589
F-13	0.759	0.231	0.179	0.820	552	612	569

Table 2.2. *P-T* estimates for the sillimanite zone. Methods for *P-T* estimation are as follows: T1 = Thompson (1976); T2 = Holdaway and Lee (1977); T3 = Perchuk (1977); T4 = Indares and Martignole (1985); P1 = Powell and Holland (1988).

| Sample no. | X_{Fe}^{Grt} | X_{Mg}^{Grt} | X_{Ca}^{Grt} | X_{Mg}^{Bt} | X_{Ca}^{Pl} | T (P = 4.0 kbar) | | | P (T = 650°C) |
						T1	T2	T3	P1
911005-04	0.583	0.164	0.038	0.492	0.333	695	695	677	4.3
911113-04	0.657	0.112	0.032	0.560	0.253	622	631	623	4.8
911113-12	0.729	0.111	0.024	0.593	0.279	629	637	629	2.9
921106-10	0.595	0.121	0.028	0.462	0.239	633	640	631	4.5

Table 2.3. *P-T* estimates for the garnet zone. Methods for *P-T* estimation are as follows: T1 = Thompson (1976); T2 = Holdaway and Lee (1977); T3 = Perchuk (1977); T4 = Indares and Martignole (1985); P1 = Aranovich and Podlesskii (1983).

| Sample no. | X_{Fe}^{Grt} | X_{Mg}^{Grt} | X_{Ca}^{Grt} | X_{Mg}^{Bt} | X_{Mg}^{Crd} | T (P = 5.5 kbar) | | | P (T = 750°C) |
						T1	T2	T3	P1
900424-01	0.729	0.168	0.022	0.590	0.547	760	757	724	5.9
900510-04	0.700	0.190	0.021	0.567	0.560	790	783	744	6.4
910430-07	0.732	0.139	0.032	0.362	0.513	755	753	720	5.5
911114-01	0.716	0.178	0.027	0.556	0.581	736	737	707	6.0
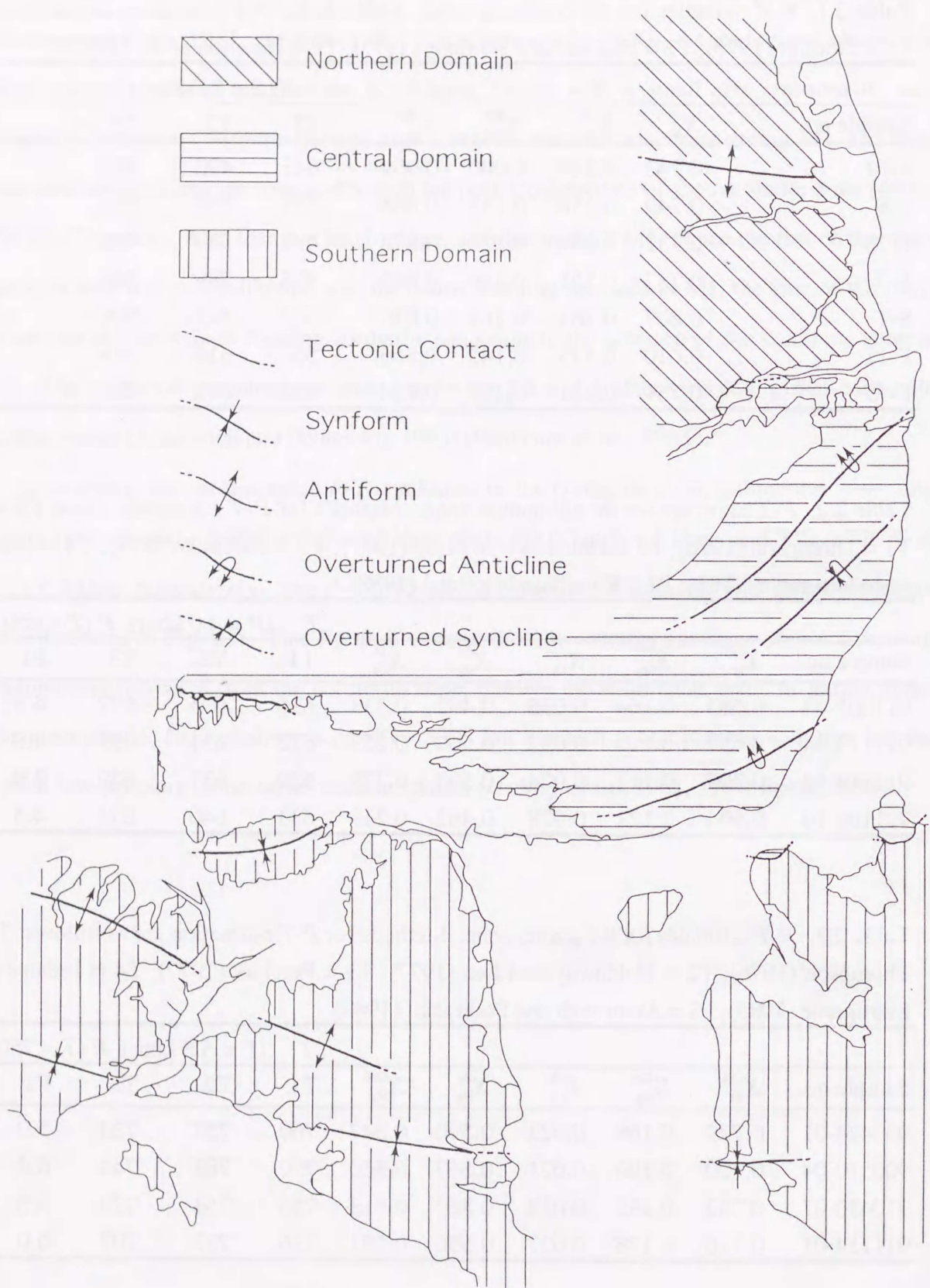
Fig. 2.1 Structural domains (northern, central, and southern domains) in the Yanai district. Axial traces of major folds are also illustrated.
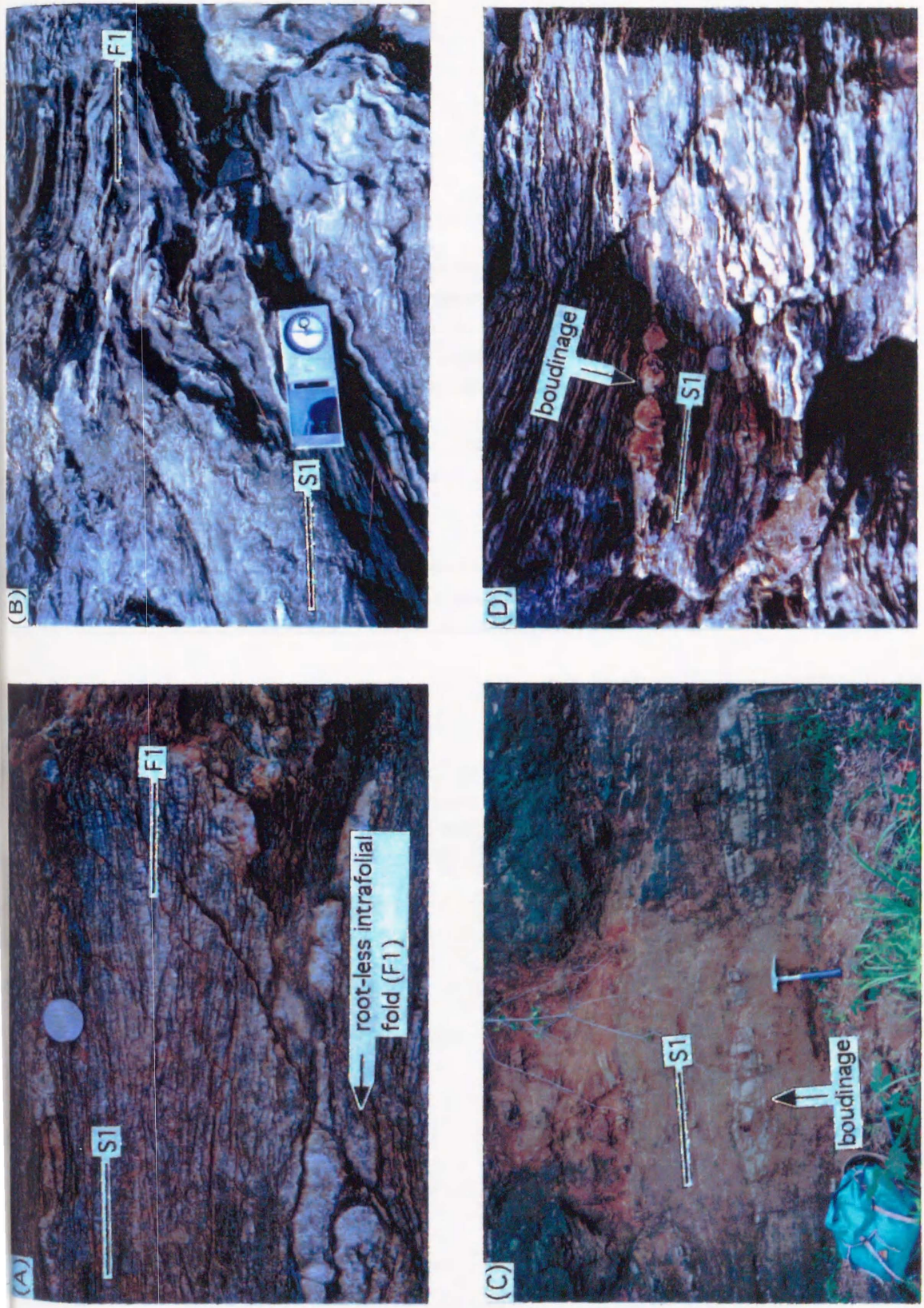
Fig. 2.2   Photographs showing D1 deformation structures on outcrop scale. a) and b) Intrafolial folds (F1) with fold axis parallel to S1-foliation (S1). c) and d) Boudinages of quartzo-feldspathic veins.

	Biotite	Cordierite	Sillimate	Garnet
Ms				
Bt				
Grt				
Crd				
Kfs				
And				
Sil				
Pl				
Qtz				

Fig. 2.3 Stability range of major constituent minerals of metapelitic and metapsammitic rocks. Abbreviations of minerals followed by Kretz (1983).

Fig. 2.4   Microphotographs showing some characteristic textures of pelitic-psammitic metamorphic rocks of the cordierite zone. a) Potash-feldspar porphyroblast (Kfs) containing other kinds minerals such as quartz (Qtz) and biotite (Bt) as inclusions, which form S0-foliation. S0-foliation is oblique at high angles to and discontinuous with S1-foliation. b) cordierite porphyroblast (Crd) containing other kinds minerals such as biotite, quartz, and muscovite (Ms) as inclusions, which form S0-foliation. S0-foliation is nearly parallel to S1-foliation. Crossed polars. Scale bars are 0.5 mm.
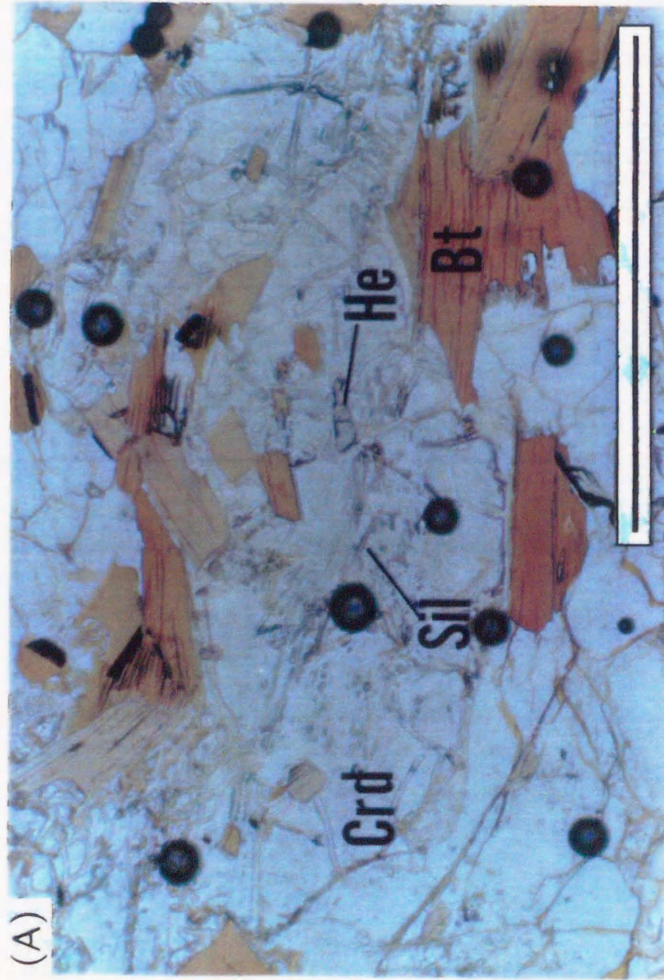
Fig. 2.5   Microphotographs showing some characteristic textures of pelitic-psammitic metamorphic rocks of the garnet zone. a) cordierite porphyroblast containing biotite (Bt), sillimanite, and Zn-rich hercynite (He).   Plane-polarized light.   b) garnet with inclusion quartz.   Matrix-forming biotite flakes are embayed in pressure shadows of garnet. Plane-polarized light. Scale bars are 0.5 mm.
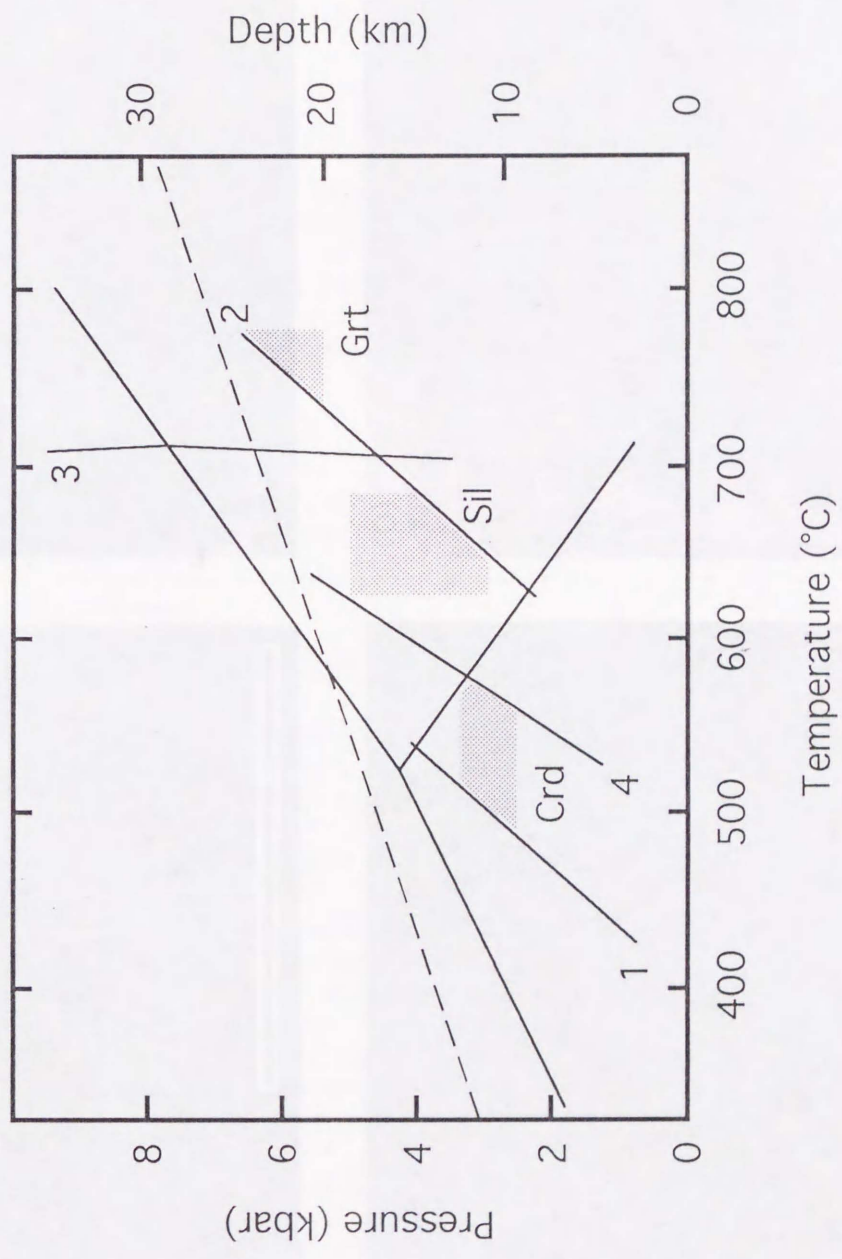
Fig. 2.6 P-T fields of the cordierite, sillimanite, and garnet zones. Reaction curves for aluminosilicate polymorphs after Salje (1986), 1) Ms + Bt + Qtz = Crd + Kfs + H2O after Massonne and Schreyer (1987), 2) Ms + Qtz = Kfs + Sil + H2O after Chatterjee and Johannes (1974), 3) Bt + Sil + Qtz = Crd + Kfs + Grt + H2O after Holdaway and Lee (1977), 4) St = Grt + Sil + He + H2O after Richardson (1968). XH2O = 0.4. Abbreviation of minerals are followed after Kretz (1983).
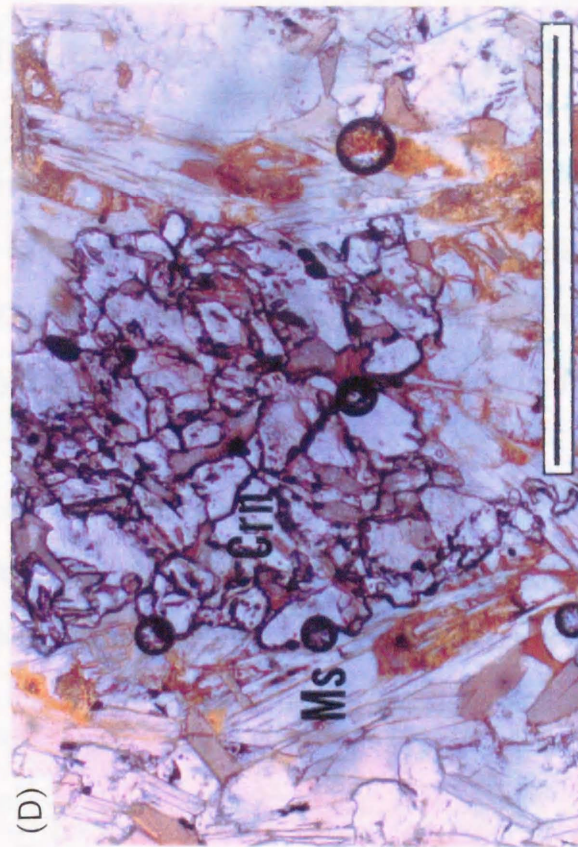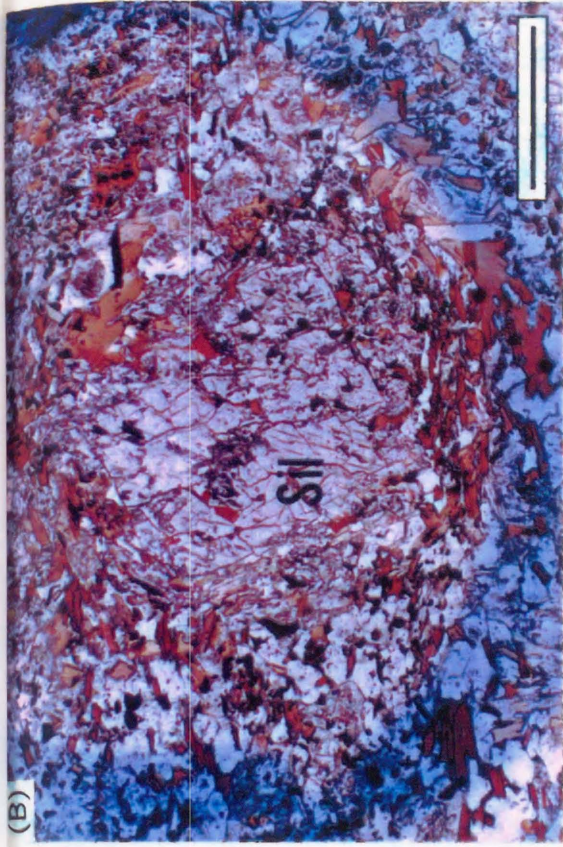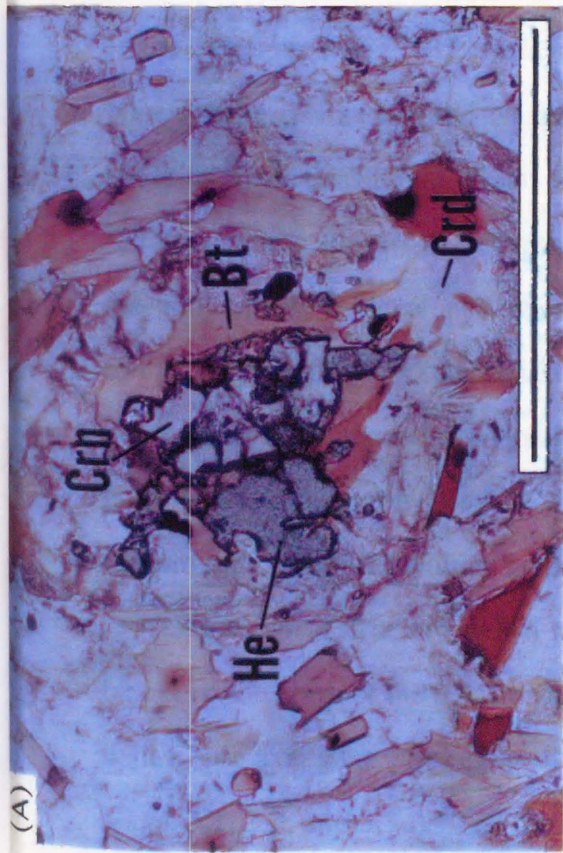
Fig. 2.7 Microphotographs showing some characteristic textures of pelitic-psammitic metamorphic rocks of the corundum rock in the Tengatake migmatite. a) aggregate of corundum (Cm), Zn-rich hercynite (He), and biotite (Bt). It is mantled by cordierite. b) sillimanite porphyroblast mantled by cordierite and biotite. c) garnet with resolved grain boundary and its closely associated biotite. d) relict corundum. Plane-polarized light. Scale bars are 0.5 mm.

The low-pressure Ryoke metamorphism (M1) is closely related to the intrusion of the Older Ryoke granitoids. The intrusion of the Older granitoids is probably related to D1 deformation (Hara *et al.*, 1991; Okudaira *et al.*, 1992, 1993). In order to clarify the intrusion mechanisms of the granitoids, therefore it is necessary that the nature of D1 deformation are clarified.

3.1: Movement picture of D1 deformation in the Tsuzu area

In order to clarify the movement picture of D1 deformation which is probably related to the intrusion of the Older Ryoke granitoids, the author analyzed the geological structures of the Tsuzu area, because in the area is only weakly found the effect of D2 deformation (see also Okudaira *et al.*, 1995a).

3.1.1: Geological structures

In the Tsuzu area (Fig. 3.1), the Ryoke metamorphic belt consists of the Gamano granodiorite, Kibe granite, Tengatake and Nagano migmatites, Iwakuni granites, and Ryoke metamorphic rocks as main constituent rocks. In the Tsuzu area the metamorphic rocks have a distinct foliation, which appears to be in general parallel to the lithologic layering. The Tengatake and Nagano migmatites developed as zones in the metamorphic rocks are intrusive bodies belonging to the member of the Older Ryoke granitoids (Okudaira *et al.*, 1993). The migmatites are developed cutting across the lithologic layering and foliation at low angles and across the lower level of lithostratigarphy toward the north (Fig. 3.2). In the migmatites, there are many metamorphic xenoliths with an agmatic structure (see Fig. 4 in Okudaira *et al.*, 1993).

The geological structure shown by the lithologic layering and foliation in the area (northern block) on the north of the EW trending Tsuzu fault is characterized by an open upright antiform with a fold axis gently plunging toward ESE, though slightly disturbed by high-angle faults (Figs. 3.1, 3.2, and 3.3a). The fold axis is placed near position Z-51 (Figs. 3.1 and 3.2). In the area (southern block) on the south of the Tsuzu fault the lithologic layering and foliation are

as a whole dipping at low to moderate angles toward the north (Figs. 3.1, 3.2, and 3.3b), though locally folded in mesoscopic scale. The π-diagram (Fig. 3.3) for the foliation, which is characterized by a broad single great-circle girdle, suggests the development of mesoscopic-scale folds with the axes gently lying in a trend of WNW-ESE (fold axis (D3) in Fig. 3.3). Such folds are found in upright fashion in many outcrops. The upright folds of various scales in the northern and southern blocks are comparable with the upright folds developed in left-hand fashion throughout the Paleozoic-Mesozoic accretionary complexes and the Ryoke metamorphic belt of the Inner Zone of southwest Japan, which postdated the intrusion of the Older Ryoke granitoids (e.g. Hara et al., 1980).

3.1.2: Metamorphic zonation

The Ryoke metamorphic rocks in the Tsuzu area suffered from two different metamorphism (M0 and M1) and those located near the Younger Ryoke and Hiroshima granitoids are additionally affected by M2 (Okudaira et al., 1993). This area can be divided into two metamorphic zones (biotite and cordierite zones) in terms of the mineral parageneses of pelitic and psammitic rocks formed during M_1 (Okudaira et al., 1993). The typical mineral assemblages are as follows:

Biotite zone:

quartz + plagioclase + biotite + muscovite,

Cordierite zone:

quartz + plagioclase + biotite + muscovite + K-feldspar + cordierite ± aluminosilicate.

Garnet crystals are not found as stable mineral in metapelites and metapsammites, although they are often found in leucosome of the migmatites. This observation suggests that the crystallization of the garnets resulted from assimilation between the metamorphic rocks and granitic materials (Owada, 1989). The regional metamorphic zonation is shown in Fig. 3.4. It is not disturbed around the Tengatake and Nagano migmatites, like the cases which have been described in the Ryoke metamorphic belt of many other districts (e.g. Koide, 1958; Kutsukake, 1977; Seo et al., 1981). Okudaira et al. (1993, 1994) have pointed out that the low-pressure facies series M1 metamorphism is ascribed to the sheet-like intrusion of the Older Ryoke

granitoids. Figure 3.4 also represents contact aureole resulted from intrusion of the Younger Ryoke and Hiroshima granitoids (M2 isograd in Fig. 3.4). The aureole is *ca.* 500 m in width and is characterized by textures of overprint of new crystals, such as muscovite, andalusite, and cordierite.

Metamorphic minerals in metapelites, which appeared under the peak metamorphic condition during M1, are available to estimate its temperature condition by using the two-feldspar (Stormer, 1975; Stormer and Whitney, 1977; Haselton *et al.*, 1983) geothermometers. The inset diagram in Fig. 3.2 represents the temperature variation in the cordierite zone which grades into the biotite zone to the north, and the garnet zone to the south (Okudaira *et al.*, 1995a, b). The metamorphic temperature estimated for sample Z-51 located north of the Tsuzu fault is significantly lower than those estimated for the samples located south of the fault (Fig. 3.2). In the southern block, the temperatures of samples F-8, E-23, and E-7 are slightly lower than those of samples S-1, F-11, and F-13 (Fig. 3.2). It can be therefore said that the metamorphic temperatures increase from north to south with decreasing of structural level.

3.1.3: Movement picture of D1 deformation

In the metamorphic rocks of the southern block and the southern part of the northern block are often found melt-filled fractures of minor scales (Fig. 3.5). Such melt-filled fractures are parallel - subparallel to and oblique to the foliation, and the constituent minerals and minor structures in and around them suggest that they were developed by shearing along the foliation during M1. The foliation-parallel ~ -subparallel fractures and foliation-oblique fractures are respectively comparable with the principle displacement shear Y, the Riedel shear R_1, and the extension fracture T (after Skempton, 1966; Logan *et al.*, 1979; Bartlett *et al.*, 1981; Shimamoto, 1989). The deformation related to the formation of these melt-filled fractures resulted commonly from the foliation parallel extension, as inferred from the orientation pattern of the fractures (Hara *et al.*, 1991).

The melt-filled fractures appear to be especially strongly developed near the migmatites and Gamano granodiorite (Hara *et al.*, 1991; Okudaira *et al.*, 1993, 1995). The metamorphic xenoliths in the migmatites, which are mainly metapelites, commonly have many melt-filled

fractures which are not traced toward their surrounding granitic parts. It is clear that the xenoliths of various scales in the migmatites were derived from fractured blocks of metamorphic rocks. Okudaira *et al.* (1993) clarified that some metamorphic xenoliths came from the much greater depth zone than the surrounding metamorphic rocks. Therefore, the migmatites have been considered by Okudaira *et al.* (1993) to be intrusives along fracture zones, which are of the same generation as the melt-filled fractures of the surrounding metamorphic rocks. The overall movement picture inferred from the melt-filled fractures appears to be of the shear sense for the top to the north (Fig. 3.6). The migmatites are developed cutting across the lower structural level toward the north as is obvious in Figs. 3.1 and 3.2. The deformation related to the formation of the fracture zones, which were responsible for the intrusion of the migmatites and therefore of the Older Ryoke granitoids, would be assumed to be of extension type.

The foliation of the metamorphic rocks in the Tsuzu area shows intrafolial folds of mesoscopic to minor scales. Their axial trends are commonly NS ~ NNW-SSE, though highly dispersed (fold axis (D1) in Fig. 3.3). Figure 3.7 shows the time-relationship between the porphyroblastic growth of metamorphic mineral crystallized during the thermal peak of M1 and D1 folding of intrafolial style. This figure indicates that the axial plane cleavage of crenulation type of D1 fold is masked by the K-feldspar porphyroblast. It can be said that the intrafolial folds with NS ~ NNW-SSE trending axes appear to be parallel to the shear direction inferred from the melt-filled fractures, which is the top to the north, and to have formed during and immediately before M1.

Asymmetric textures such as extensional crenulation cleavage (ECC; Platt and Vissers, 1980) (Fig. 3.8a) and rotation of porphyroblasts (Fig. 3.8b) such as cordierite and K-feldspar, which were crystallized during M1, are often recognized in thin section of metapelites. These asymmetric textures are considered in relation to M1. Figure 3.9 illustrates the chemical compositions of the foliation-forming biotite and the ECC-forming biotite, suggesting that the former and the latter formed under the same metamorphic condition, which corresponds to the condition of M1. The shear sense read from the above-mentioned asymmetric textures is top to the north, though fairly dispersed, as shown in Fig. 3.10. This is harmonic with the overall

movement picture inferred from the melt-filled fractures (see Figs. 3.6 and 3.10). As mentioned above, the formation of the melt-filled fractures was responsible for the intrusion of the Older Ryoke granitoids and for M_1. Therefore it can be said that the overall movement picture of D1 deformation of the metamorphic rocks in the Tsuzu area during and immediately before the intrusion of the Older Ryoke granitoids was of the same style of extension tectonics.

3.2: Deformational conditions of D1 deformation as inferred from naturally deformed quartz in metacherts

Analysis of quartz microtextures provides information of deformational conditions in metamorphic tectonites (e.g. Hara, 1962; Hobbs, 1985; Mainprice and Nicolas, 1989; Takeshita, 1989). Therefore, the deformation microstructures and quartz c-axis fabrics of seven samples from non-folded metacherts in the cordierite and garnet zones have been investigated with petrographic microscope. Furthermore, the analyses of dislocation microstructures with transmission electron microscopy (TEM) have been conducted in order to elucidate the slip direction (i.e., Burgers vector). Based on the analyses, the deformational conditions of D1 deformation are documented (see also Okudaira *et al.*, 1995b).

3.2.1: Background

There are several different families of slip systems in quartz, and different families of slip systems dominate at different physical conditions and environments. The factors that determine the dominant slip systems include temperature (e.g. Tullis *et al.*, 1973), P_{H2O} (e.g. Griggs and Blacic, 1965; Linker *et al.*, 1984), strain rate (e.g. Tullis *et al.*, 1973), pressure (e.g. Kronenberg and Tullis, 1984), and defect chemistries (e.g. Hobbs, 1981, 1984). Among these parameters, temperature could be the most important factor to control the critical resolved shear stress (CRSS) on slip systems in quartz (e.g. Hobbs, 1985; Takeshita and Wenk, 1988; Mainprice and Nicolas, 1989). Since the temperature dependence (activation energy) of CRSS varies for different slip systems, different slip systems become dominant with increasing temperature.

27

Lister (1981) documented that simulated *c*-axis fabrics change from girdle pattern to *X*-maximum pattern (where the *c*-axes are dominantly aligned parallel to the maximum elongation direction) as the dominant slip direction changes from <*a*> to [*c*]. Many natural quartz *c*-axis fabrics reported to date show that slip in the <*a*> direction on cozonal glide planes is the dominant slip system in naturally deformed quartz at low ~ medium temperature condition (e.g. Bouchez and Pêcher, 1981). However, such the *X*-maximum fabric patterns in naturally quartz have been found in granitic rocks naturally deformed at very high-temperature (*ca.* 650 ~ 750°C) which is close to the subsolidus temperature of granite (e.g. Bouchez *et al.*, 1984; Blumenfeld *et al.*, 1986; Gapais and Barbarin, 1986; Mainprice *et al.*, 1986; Garbutt and Teyssier, 1991).

Griggs and Blacic (1965) noted that a dramatic weakening in synthetic quartz occurs at 400°C with increasing temperature. They attributed the weakening to the mechanism switch from basal <a> to prism [c] which has been concluded to be caused by the increasing diffusion of water into the quartz lattice. Furthermore, Linker *et al.* (1984) documented, for a synthetic quartz crystal favorably oriented for both *a* and *c* slips, *c* slip is preferred over *a* slip at temperature condition at 750°C which could be compared with low ~ medium temperature condition at geological strain rates (10^{-16} ~ 10^{-14} s^{-1}). Since the synthetic quartz includes significant amount of water, these facts could suggest that *c* slip is aided by the intracrystalline water, which can more effectively diffuse into the quartz lattice with increasing temperature (Kronenberg and Tullis, 1984). If we can extrapolate the experimental results proposed by Linker *et al.* (1984) to geological strain rates, then the initiation of *c* slip will cause a plastic softening approximately equivalent to an order of magnitude increase in strain rate over <*a*> slip (Mainprice *et al.*, 1986).

3.2.2: Sample description

The microstructures and *c*-axis fabrics of quartz grains in five metacherts (A, B C, D, and E) from the cordierite zone and two samples (F and G) from the garnet zone are described here. Localities of the seven investigated samples are indicated in Fig. 3.11. Figure 3.12 illustrated a schematic cross section of the cordierite zone in order to show the spatial relationship between

the sample localities of microstructural analyses and those of metamorphic temperature analyses. Upper diagram in Fig. 3.12 represents the temperature variation in the cordierite zone. There is the Tsuzu fault (Higashimoto *et al.*, 1983) which divide the cordierite zone into two domains (northern and southern domains) in central part of the zone (Fig. 3.11). Because the southern domain was relatively upheaved to the northern domain, sample Z-51 indicates the lowest temperature in the zone (Fig. 3.11). In the southern domain, the temperatures of samples F-8, E-23, and E-7 are slightly lower than those of samples S-1, F-11, and F-13 (Fig. 3.11). Samples A and B were collected from nearly the same structural position in the uppermost part of the cordierite zone close to the cordierite isograd, and sample E was collected from the lowermost part of the cordierite zone (Fig. 3.11). Although the metachert samples were taken from different structural levels, distribution of the metacharts in the cordierite zone is not sufficient to draw a fabric "isograd", which the case of the Saxony granulite terrain (see Lister and Dornsiepen, 1982). Samples F and G are collected from the garnet zone and their structural positions are situated at a similar level.

The rock sample of the seven metacherts are characterized by a single foliation formed during D1 deformation, which is defined either by the alternation of mica-rich and mica-poor layers or by the preferred shape orientation of mica grains. Since the examined metacherts show no evidence of D2-folding on an outcrop scale, the amount of strain suffered from D2 deformation could be neglected.

Deformation microstructures

Samples A and B consist of many small polygonal and few large quartz recrystallized grains (Fig. 3.13a). The mean grain sizes of small polygonal grains in samples A and B are *ca.* 40 (min.: 15 μm; max.: 65 μm) and 45 μm (min.: 12 μm; max.: 80 μm), respectively, whereas those of large grains are *ca.* 250 (min.: 145 μm; max.: 465 μm) and 145 μm (min.: 90 μm; max.: 275 μm), respectively. The shape of the large grains (open squares in Fig. 3.13a) is more elongated than that of the small grains (closed squares in Fig. 3.13a). Because the larger quartz grains exclusively form veinlets in samples A and B (Fig. 3.13a), it could be considered that these grains did not significantly suffer grain size reduction by dynamic recrystallization

after the vein formation. Sample C shows a weak bimodal grain size distribution (Fig. 3.13b). The mean grain size of smaller grains is *ca.* 250 μm (min.: 75 μm; max.: 540 μm) and that of larger grains is *ca.* 1100 μm (min.: 700 μm; max.: 2480 μm).

Samples D, E, F, and G exhibit essentially the same microstructure (Fig. 3.13c, d). These samples are mainly composed of large recrystallized grains (*ca.* 200 ~ 3700 μm). The mean grain sizes of samples D, E, F, and G are *ca.* 810 μm (min.: 60 μm; max.: 3600 μm), 880 μm (min.: 210 μm; max.: 2300 μm), 1060 μm (min.: 140 μm; max.: 4150 μm), and 1450 μm, respectively, whereas the grain size varies considerably within one thin section for all the samples. In summary, the mean recrystallized grain size of quartz in the cordierite zone increases greatly from sample A (*ca.* 40 μm) to sample E (*ca.* 880 μm) with increasing structural level. Particularly, the abrupt increase in recrystallized grain size from sample B (45 μm) through C (250 μm) to D (810 μm) occurs within the structural distance less than 500 m. Here, the vertical displacement along the Tsuzu fault is assumed to be small. Because the increase in recrystallized quartz grain size is consistent with the rise of the petrologically estimated peak metamorphic temperature of M1, it is concluded that the deformation temperature increases from samples A and B through C to D and E.

Figure 3.14 indicates aspect ratio (ratio of long-axis to short-axis) versus grain size (geometric mean of long-axis and short-axis) of quartz grains in samples A, C, D, and G. The major difference between sample A and samples D and G is that for the former sample the aspect ratio varies greatly from 1 to 6 at a fairly constant grain size, and for the latter samples the grain size varies greatly at a fairly small aspect ratio (around 2). Sample C belongs to the intermediate type between the two. Those results in principle represent a decrease of aspect ratio and an increase of grain size with increasing temperature. The grain boundaries of the recrystallized quartz grains for all the samples, particularly samples C to G composed of larger grain size (> 250 μm), exhibit a cuspate shape indicative of grain boundary migration.

Quartz c-axis fabrics

The *c*-axis orientation of individual grains with respect to the structural reference frame (*X*: parallel to the lineation, *Z*: normal to the foliation, and *Y*: normal to the *X* and *Z* directions) was

determined using a universal stage. Figure 3.15 illustrates the lower hemisphere equal-area projections of quartz c-axis fabrics of the samples from the cordierite zone. Quartz c-axis fabrics in samples A and B, from a low-temperature part of the zone, show a type II crossed girdle pattern (e.g. Lister, 1977; Price, 1985) with half opening angle of 30 ~ 35° (Fig. 3.15a, b), with Y-submaximum for sample B. The c-axis fabric pattern of sample C shows a small circle-girdle around Z with the same half opening angle as those of sample A and B (Fig. 3.15c). On the other hand, quartz c-axis fabrics in samples D and E from a high-temperature part of the zone have a distinct X-maximum which is rotated clockwise by 10 ~ 20° about Y from X. However, both quartz c-axis fabrics exhibit a faint great-circle girdle inclined at 45° to Z, and nearly parallel to Y, as indicated by dashed lines in Fig. 3.12d, e, although any crossed girdle pattern is not apparent. For sample E, Z-maximum is apparent in addition to the above-described fabric components.

Figure 3.13 illustrates quartz c-axis fabrics of the samples from the garnet zone. Sample F represents XY girdle with an X-maximum elongated toward Y and a submaximum at Z (Fig. 3.16a). The c-axis fabric in sample G shows both Y-maximum and X-maximum (Fig. 3.16b).

Subgrain boundaries (SGB's)

During plastic deformation, by a combination of glide and climb, arrays of dislocations form SGB in order to reduce stored elastic strain energy (Ball and Hirsch, 1955). Given that SGB's are lower energy structures than free dislocations, they should be less susceptible to modification by post-deformation annealing (Mainprice *et al.*, 1986). Therefore, SGB in quartz is a useful indicator of operated slip systems during high-temperature plastic deformation.

Quartz grains in samples A, B, and C show little undulatory extinction, and have straight or slightly curved grain boundaries (Fig. 3.13a, b). In these samples, the SGB's are rare and mostly parallel to the c-axes, indicating that the SGB's are in the same zone as that of prismatic planes. On the other hand, in samples D, E, F and G, SGB's are well developed and are irregularly curved or cuspated (Fig. 3.13c, d). In these samples the quartz c-axes in many quartz grains are preferentially oriented parallel to the lineation (Figs. 3.15 and 3.16), and most

31

of the SGB's in such oriented quartz grains are nearly perpendicular to the *c*-axes indicating that the SGB's are parallel, or nearly so, to the basal (0001) plane. Such basal SGB's often form approximately square subgrains with subordinate planar prismatic SGB's (Fig. 3.13c, d).

A statistical analysis for angle between the SGB and *c*-axis was undertaken for the samples having many visible SGB's (Fig. 3.17). In the cordierite zone, samples B and C show high population of prismatic SGB's (Fig. 3.17a, b). On the other hand, in samples D and E, about 20% of the SGB's are in prismatic orientation, while more than 60% in basal to sub-basal one (Fig. 3.17c, d). In the garnet zone, sample F represents that more than 80% of the SGB's are in basal to sub-basal orientations (Fig. 3.17e). Sample G shows that the population is almost entirely represented by basal SGB's (Fig. 3.17f).

TEM observations

Direct observation of dislocations by TEM has been conducted in order to determine the slip systems operated in deformed quartz (e.g. Nicolas and Poirier, 1976). To confirm our understanding of the slip systems which are independently from the pattern of quartz *c*-axis fabric and orientation of SGB, TEM observations were made of samples A, D, and G. Quartz grains containing well-defined SGB's were selected. All observations were carried out with a JEOL JEM-200CX transmission electron microscope at Ehime University using an accelerating voltage of 200 kV. The samples were ion-thinned and carbon coated for the TEM observation.

Observations were made on free dislocations and subgrain boundaries in the samples. In addition, dislocation densities of quartz were measured with TEM. For the determination of dislocation density, the number of free dislocations within 5 areas ranging from about 5.3 x 3.8 to 3.1 x 2.2 μm^2 was counted for each grain. Some typical images of dislocation microstructures are shown in Fig. 3.17. In sample A dislocations are fairly homogeneously distributed (Fig. 3.18a), while in sample G many dislocation loops are observed in addition to curved free dislocations (Fig. 3.18b). The free dislocation densities (ρ) in samples A and G are similar, which are $\rho = (8.9 \pm 1.4) \times 10^8$ cm^{-2} and $\rho = (1.3 \pm 0.4) \times 10^9$ cm^{-2} respectively. In sample D, the subgrain boundaries composed of simple arrays of parallel dislocations which are normal to [0001] direction are common and they are often curved (Fig. 3.18c). These high

densities of dislocation in naturally deformed quartz at high-temperature in this district are comparable to those in the Bergell Alps (Liddell *et al.*, 1976). In samples A and G many bubbles are recognized (Fig. 3.15a, b). The bubbles consist of two sets of lobes symmetrically placed about a line of no contrast. The line of no contrast is always parallel to [0001] in sample G.

Analysis of slip systems was carried out using the standard technique of "invisibility criteria", which had been shown to be effective in quartz (Hirsch *et al.*, 1965; Ardell *et al.*, 1974). For a dislocation to be invisible, the following condition is required, namely the vector products $g \cdot b = 0$ for a pure screw dislocation, and $g \cdot b \times u = 0$ for a edge dislocation, where g is the diffracting vector, b the Burgers vector and u the unit vector along the dislocation line. An image of free dislocation of quartz in sample G is shown in Fig. 3.19. Figure 3.19a shows a bright-field image of free dislocation and Fig. 3.19b represents a dark-field image of the same area. Since the dislocation is almost out of contrast for the diffracting vector $g = [11\bar{2}0]$, [0001] could be a possible Burgers vector for screw dislocation. In fact, since the dislocation line is nearly parallel to [0001], the dislocation could be identified as a [0001] screw dislocation.

3.2.3: Inferred slip systems

Dominant slip systems in quartz polycrystals can be estimated from the pattern of *c*-axis fabrics and preferred maximum orientations (e.g. Lister *et al.*, 1978; Lister and Hobbs, 1980). Moreover, the angle between *c*-axis and SGB in a quartz grain allows us to infer the operating slip system (e.g. Christie and Green, 1964; Trépied *et al.*, 1980; Blumenfeld *et al.*, 1986; Mainprice *et al.*, 1986).

The *c*-axis fabrics in samples A and B show type-II crossed girdle patterns (Fig. 3.15a, b) with half opening angle of 30 ~ 35° with *Y*-submaximum for sample B. The c-axis fabric pattern of sample C shows a small circle-girdle around Z (Fig. 3.15c). The type-II crossed girdle and small circle pattern with large half opening angles can be produced by the dominant activation of basal <*a*> and prism <*a*> slip systems (Lister and Hobbs, 1980; Takeshita and Wenk, 1988; Wenk *et al.*, 1989).

In sample F the pattern of *c*-axis fabric almost shows both *Y*-maximum and *X*-maximum (Fig. 3.16a). The fabric pattern in sample G is characterized by an *X*-maximum elongated toward *Y* (Fig. 3.16b). High concentration of *c*-axes near *X* is ascribed to the dominant activation of prism [*c*] slip systems, which is numerically demonstrated by Lister (1981) and proved for naturally deformed quartz at very high-temperature close to granite subsolidus (Blumenfeld *et al.*, 1986; Mainprice *et al.*, 1986). On the other hand, the high concentration near *Y* is considered to be due to the dominant activation of prism <*a*> slip systems (Wenk *et al.*, 1989). We currently do not have a good explanation for a maximum at *Z* observed for samples E and F. The *Z*-maximum may be related to the grain growth during deformation (Hirth and Tullis, 1992). Consequently, the fabric patterns in the samples F and G can be ascribed to the dominant activation of prism [*c*] slip system, with a subordinate activation of prism <*a*> slip (Lister and Hobbs, 1980; Lister, 1981; Wenk *et al.*, 1989).

The *c*-axis fabric patterns of samples D and E are respectively characterized by a distinct *X*-maximum and a faint great-circle girdle inclined ~ 45° to *Z* and nearly parallel to *Y*. These could be interpreted as a transitional pattern from type-II crossed girdle to *X*-maximum. Therefore, the *c*-axis fabric patterns could have been caused by activation of prism [*c*], prism <*a*>, and basal <*a*> slip systems (cf. Lister, 1981).

Furthermore, the basal SGB's in deformed quartz are exclusively characteristic of *c* slip, whereas the prismatic SGB's indicate the operation of *a* slip (e.g. Christie and Green, 1964; Trépied *et al.*, 1980; Blumenfeld *et al.*, 1986; Mainprice *et al.*, 1986). The high frequency of prismatic SGB's of quartz in samples A, B, and C probably indicates that the slip direction is dominantly in <*a*> (see Fig. 3.17a, b). On the other hand, the dominance of basal SGB's of quartz in samples D, E, F, and G indicates that [*c*] slip predominates over <*a*> slip in these samples (see Fig. 3.17c, d, e, f). However, <*a*> slip indicated by prismatic SGB's (i.e. [*c*] ∧ SGB = 0°) still operated in samples D and E, while the activity of <*a*> slip is negligible for samples F and G. Although the angle between the SGB and *c*-axis theoretically should exhibit 90° for [*c*] slip, the angles in Fig 3.17 distribute over wide range for samples D, E, and F. These basal SGB's are rarely planar and sometimes take a cuspate shape under optical (Fig. 3.13c, d) and under electron microscopes (Fig. 3.18c). These curved and cuspate basal SGB's

are probably caused by subgrain boundary migration during the syn- and/or post-dynamic recrystallization (cf. Urai *et al.*, 1986). Therefore, the sub-basal subgrain boundaries, that is $[c] \wedge SGB = 60 \sim 80°$, could be attributed to the migration of basal SGB's.

The TEM observation in sample G reveals the presence of free dislocations with the [0001] Burgers vector (Fig. 3.19). This glide system is consistent with the presence of (0001) dislocation subgrain boundaries (Fig. 3.18c) in sample D. These observations also indicate that samples D and G are deformed by the dominant $[c]$ slips.

Based on the pattern of *c*-axis fabrics, orientation of SGB's, and TEM observations, it has been shown that samples A, B, and C were deformed by the dominant activation of basal *<a>* and prism *<a>* slip systems, whereas samples D, E, F, and G were deformed by the dominant activation of prism $[c]$ slip systems, with subordinate activation of prism *<a>* slip system. Although $[c]$ slip is dominant in samples D and E, the activation of slip systems is characterized by a transitional type where basal *<a>* and prism $[c]$ both operate. In conclusion, the basal-prism mechanism switch possibly occurred in samples D and E.

3.2.4: Transition conditions from basal *<a>* to prism $[c]$ slip

Quartz *c*-axis fabrics have also been investigated elsewhere in the Ryoke metamorphic belt (e.g. Nureki, 1960; Hara, 1962). In the Kasagi district (Fig. 3.1), Hara (1962) suggests that quartz *c*-axis fabrics characterized by crossed girdle with a distinct *Y*-maximum were developed at temperatures higher than *ca.* 450°C. The fabric patterns suggest that the prism *<a>* and basal *<a>* slip systems were active.

In the cordierite zone of the Yanai district, it has been shown that samples A, B, and C were deformed by the dominant activation of basal *<a>* and prism *<a>* slip systems, whereas samples D and E were deformed by the dominant activation of prism $[c]$ slip systems, with the subordinate activation of prism and basal *<a>* slip, even though these samples occur only *ca.* 400 m apart in structural level and coexist in the zone of same metamorphic grade. In samples F and G from the garnet zone, $[c]$ slip exclusively operates. Therefore, the mechanism switch from basal *<a>* to prism $[c]$ slip systems, as proposed by Lister (1981), could have taken place between samples A, B, and C, and samples D and E from naturally deformed metacherts in the

Ryoke metamorphic belt, although the activation of slip systems in samples D and E is characterized by a transitional type between dominant <a> slip and dominant [c] slip. The temperature condition for the cordierite zone to which the samples all belong is estimated by various geothermometers to range from 460 to 590°C (Table 3.1 and Fig. 3.12). More precisely, the metacherts deformed at *ca.* 460 ~ 550°C (samples A, B, and C) show no evidence of prism [c] slip, those deformed at *ca.* 550 ~ 590°C (samples D and E) show about 75 ~ 80% [c] slip, and those from the garnet zone (samples F and G) show ≅100% prism [c] slip (see Fig. 3.17). Therefore, it can be concluded that the basal - prism mechanism switch probably occurred within the temperature range of 550 ~ 600°C.

The *X*-maximum fabric patterns in naturally deformed quartz were reported only in the rocks deformed under very high-temperature which is close to granite subsolidus (e.g. Bouchez *et al.*, 1984; Blumenfeld *et al.*, 1986; Gapais and Barbarin, 1986; Mainprice *et al.*, 1986; Garbutt and Teyssier, 1991). Mainprice *et al.* (1986) also observed the *X*-maximum *c*-axis fabrics indicative of dominant prism [c] slip in the migmatite and granitic vein naturally deformed at 650 ~ 750°C.

Mainprice *et al.* (1986) emphasized that the association of very high-temperature and humid conditions appears to be the key requirement to active *c* slip. Since quartz crystals have reached the limit of H_2O solubility, they must have been well within the regime of hydrostatic weakening when they were deformed (Griggs and Blacic, 1965). Because the metachert samples consist of hydrous minerals such as biotite and muscovite and these minerals could release a significant amount of water above 500°C (cf., Walther and Orville, 1982), the increase of water content in rock with increasing temperature could cause the activation of *c*-slip. Moreover, the presence of numerous bubbles on TEM observations (Fig. 3.16a, b) indicates that the quartz seems to be "Wet" crystal. The abnormal increase of recrystallized quartz grain size with increasing temperature which is associated with the mechanism switch from <a> to [c] slip, appears to have been accomplished by water-assisted grain boundary migration (growth) (e.g. Urai *et al.*, 1986), in addition to the fact that a critical temperature for grain boundaries to break away from the pinning effects of impurities was exceeded in the metachert samples (cf. Guillope and Poirier, 1979).

36

3.2.5: Strain rates inferred from dislocation density paleopiezometer

It has been known that the dislocation density is only a function of differential stress (σ_1-σ_3). A few empirical relations between differential stress and dislocation density have been obtained as follows:

$$\sigma_1 - \sigma_3 = 1.64 \times 10^{-4} N^{0.66} \qquad \text{(McCormick, 1977)} \qquad (3.1)$$

$$\sigma_1 - \sigma_3 = 6.6 \times 10^{-3} N^{0.5} \qquad \text{(Weathers } et\ al.\text{, 1979)} \qquad (3.2)$$

where N is dislocation density. Plugging the dislocation densities of samples A and G, which are obtained as $(8.8 \pm 1.7) \times 10^8$ cm^{-2} and $(1.0 \pm 0.7) \times 10^9$ cm^{-2} respectively into the Eqs. (3.1) and (3.2), the differential stress for the samples A and G can be calculated as *ca.* 130 and 140 MPa for Eq. (3.1), and *ca.* 200 and 210 MPa for Eq. (3.2), respectively.

Strain rate ($\dot{\varepsilon}$) in the quartz can be estimated by the following equation of power law creep:

$$\dot{\varepsilon} = A\sigma^n \exp(-E/RT) \qquad (3.3)$$

where σ is differential stress, and A, n, and E are experimentally determined constants, namely pre-exponential constant, stress exponent and activation energy, and R and T are gas constant and absolute temperature respectively. Following Koch *et al.* (1989), A, n, and E have been experimentally determined to be 5.05×10^{-6} MPa^{-n} s^{-1}, 2.61, and 145 kJ, respectively. Now, I can calculate strain rate in the samples using Eq. (3.3), assuming that deformation temperatures in the samples are nearly the same as the peak metamorphic temperatures, which are 500°C (cordierite zone) and 750°C (garnet zone), respectively. Then the strain rates of the samples are obtained as (*ca.* 2.7 ~ 7.7) $\times 10^{-10}$ s^{-1} and (*ca.* 0.8 ~ 2.3) $\times 10^{-7}$ s^{-1}, respectively. The strain rates in the samples are much faster than the generally assumed geological strain rate, i.e. 10^{-16} ~ 10^{-14} s^{-1}. Such high strain rates in metamorphic belts are also estimated for other metamorphic belts (e.g. Hacker *et al.*, 1992).

3.3: Concluding remarks for the analysis

Recently, Miyashita and Komatsu (1993, 1994) indicated that the deformation related to the formation of foliation in metamorphic rocks, which has a top to the north ~ northwest sense of shear, is of extension type. The author also concluded that D1 deformation, which was high-temperature deformation with high-strain rate ($\approx 10^{-10} \sim 10^{-7}$ s^{-1}), was operated under extensional stress regime and that the Older Ryoke granitoids intruded in extensional fracture zones at intermediate crustal depths. The tectonic model for the emplacement of the Older Ryoke granitoids is illustrated in Fig. 3.20. The extension tectonics occurred with the tensional stress approximately normal to the general trend of the Ryoke metamorphic belt. Following the tectonics, the Ryoke metamorphic belt suffered compressional deformations (D2 and D3) which was related to the formation of nappes transporting toward the WSW or SW (Okudaira *et al.*, 1992, 1993).
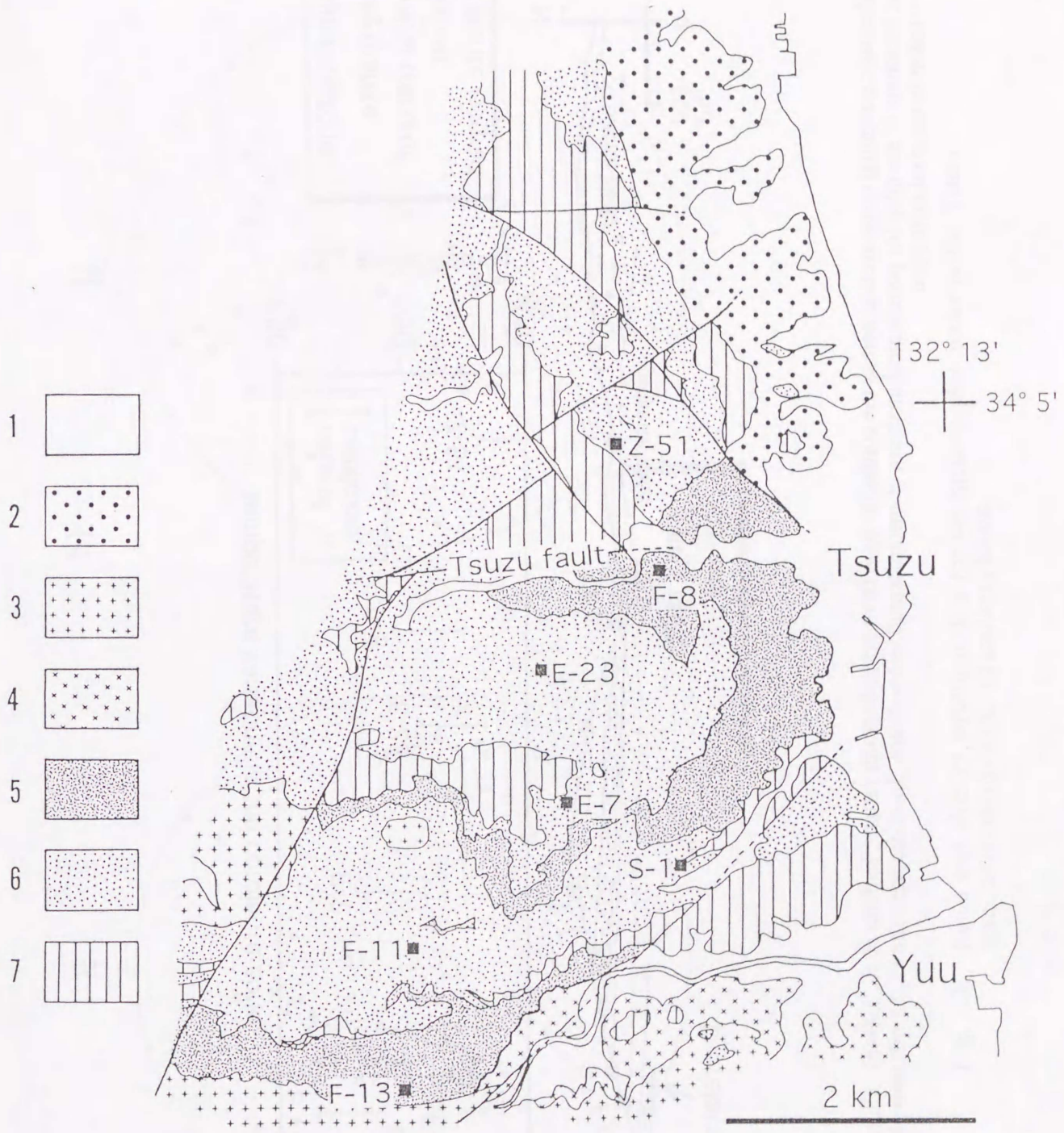
Fig. 3.1. Geological map of the Tsuzu area. 1: alluvium. 2: Hiroshima granites. 3: Younger Ryoke granites. 4: Older Ryoke granites. 5: agmatic migmatite zone. 6: metapelites and metapsammites. 7: metacherts. Closed squares indicate locations of samples using petrologically estimate of metamorphic temperatures.
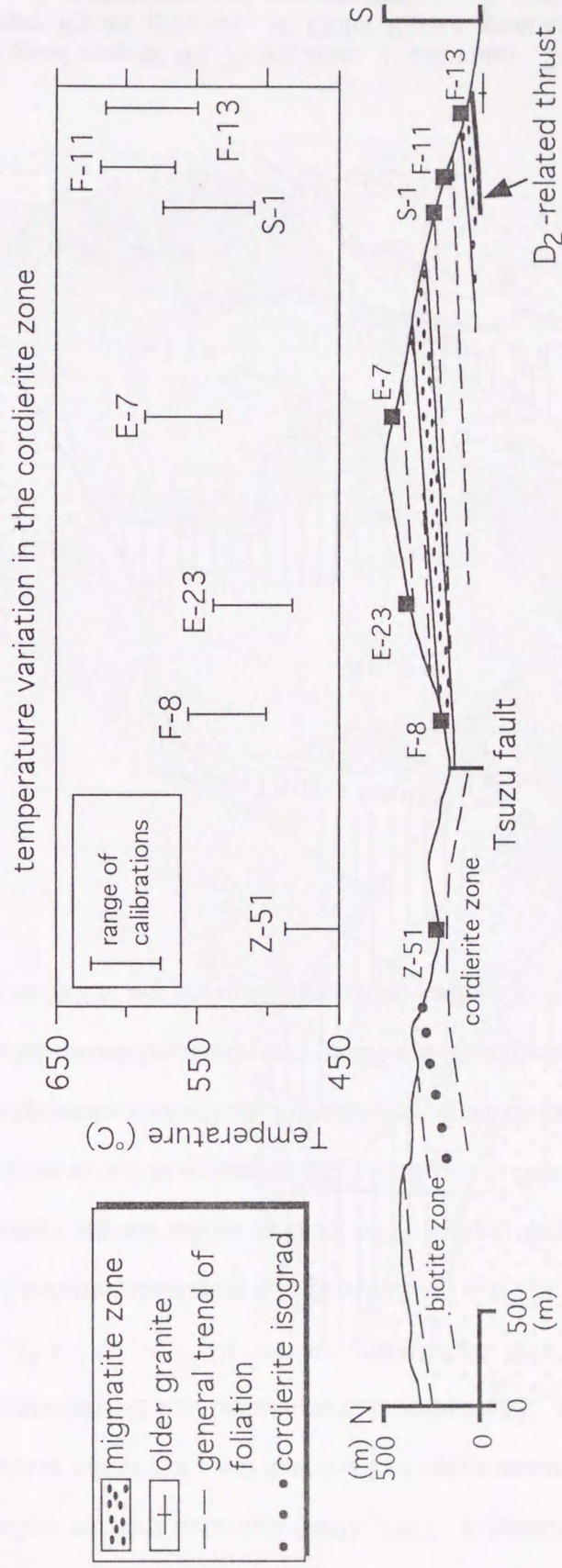
Fig. 3.2. Schematic structural cross section across the cordierite zone from north to south (after Okudaira et al., 1994b). Closed squares indicate the locations of samples for petrological analyses of metamorphic temperature. Inset diagram shows the metamorphic temperature variation in the cordierite zone.
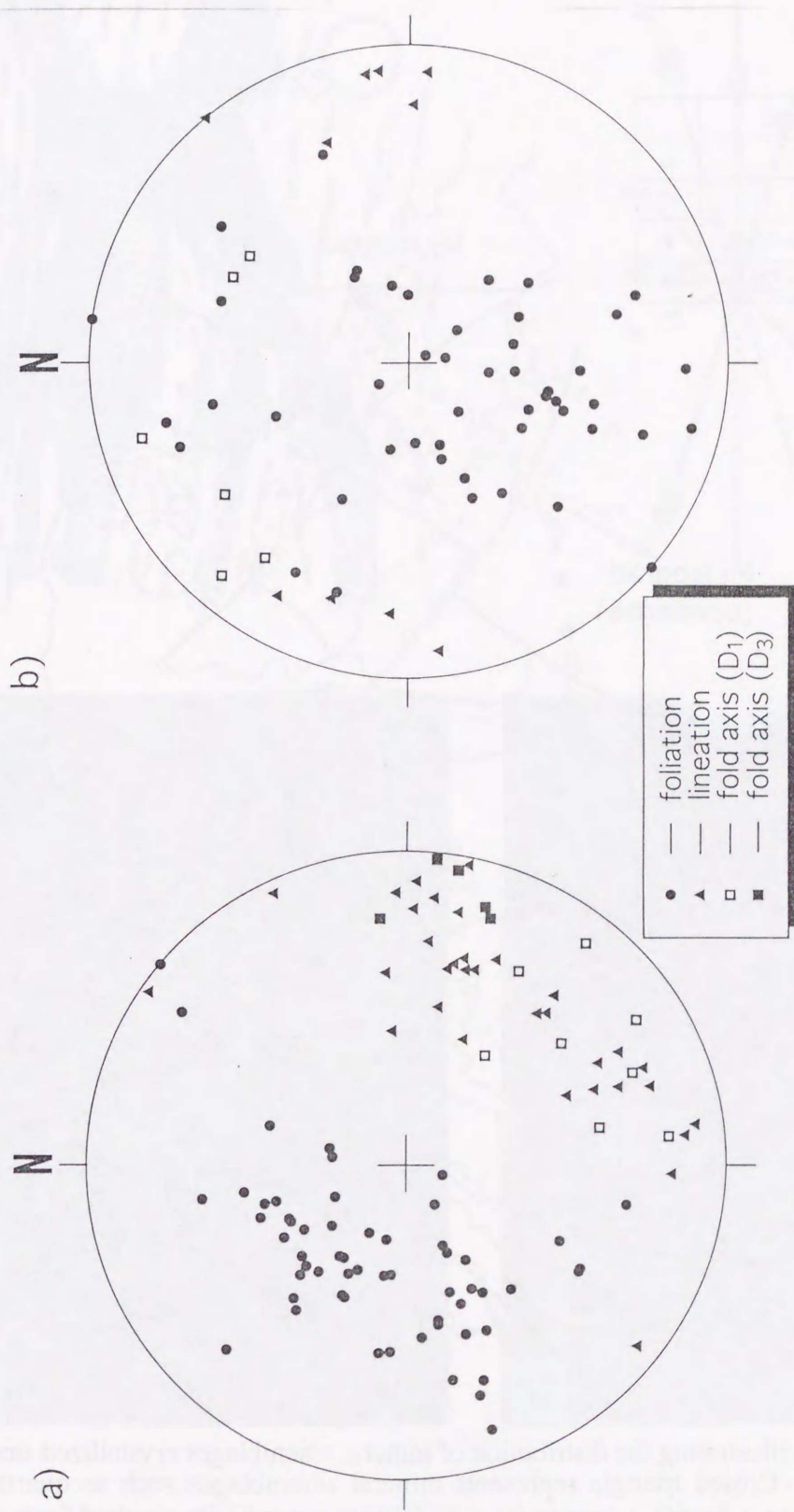
Fig. 3.3.   Equal area plots of structural data for the metamorphic rocks in the Tsuzu area. a) northern block. b) southern block.

Legend:
- foliation
- lineation
- fold axis (D_1)
- fold axis (D_3)

Mineral Assemblage	
Ms+Bt	△
Ms+Bt+Crd I+Kfs	○
Ms+Bt+Crd I+Kfs+And	◑
Ms+Bt+Crd I+Kfs+Sil	◑

M2 isograd

M1 isograd
(cordierite)
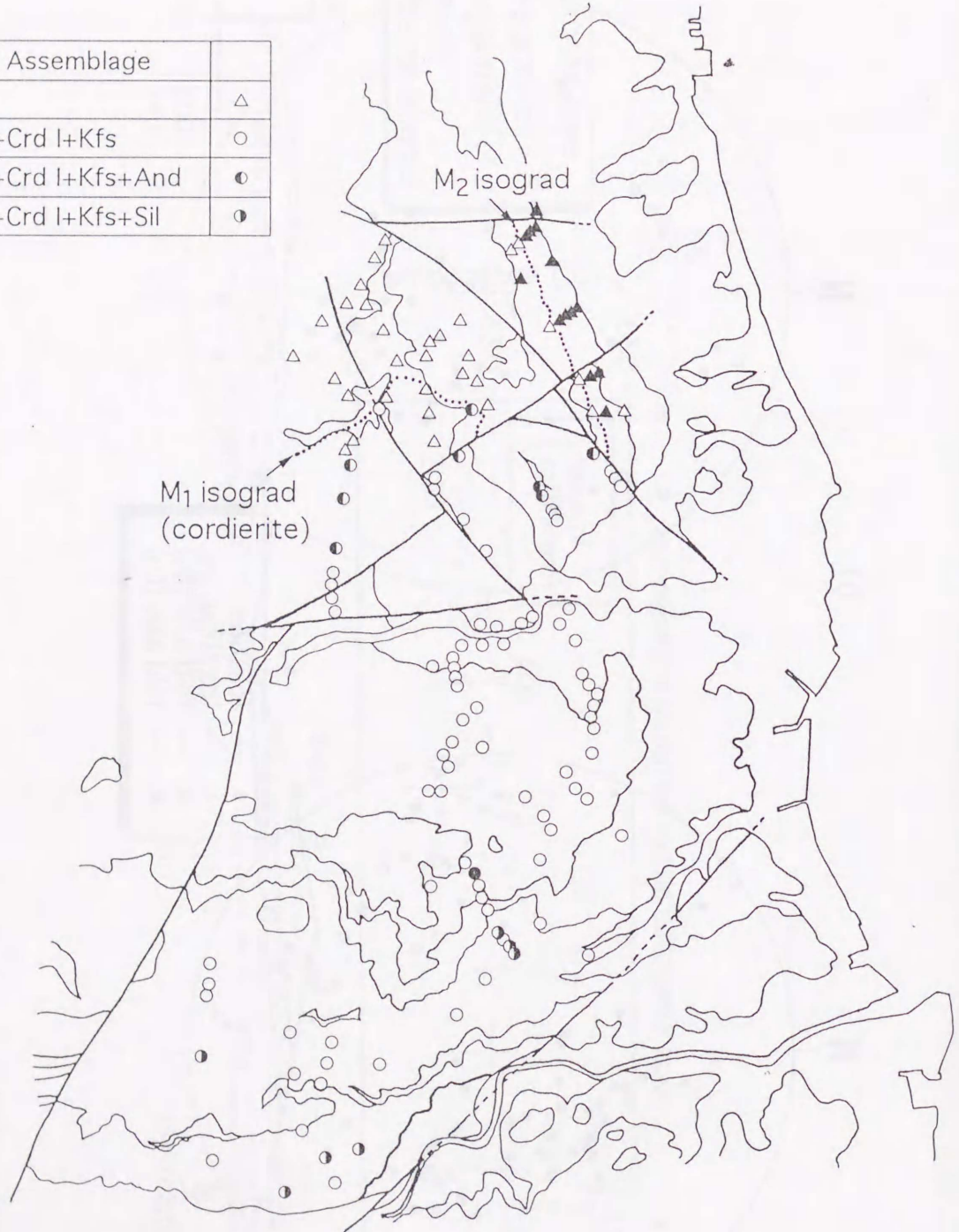
Fig. 3.4. Diagram illustrating the distribution of mineral assemblages crystallized under the M_1. Closed triangle represents mineral assemblages such as quartz + plagioclase + biotite + muscovite ± andalusite ± cordierite resulted from the M_2 metamorphism.
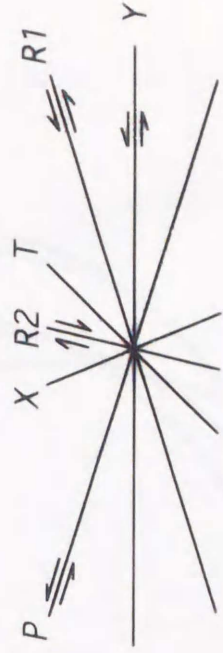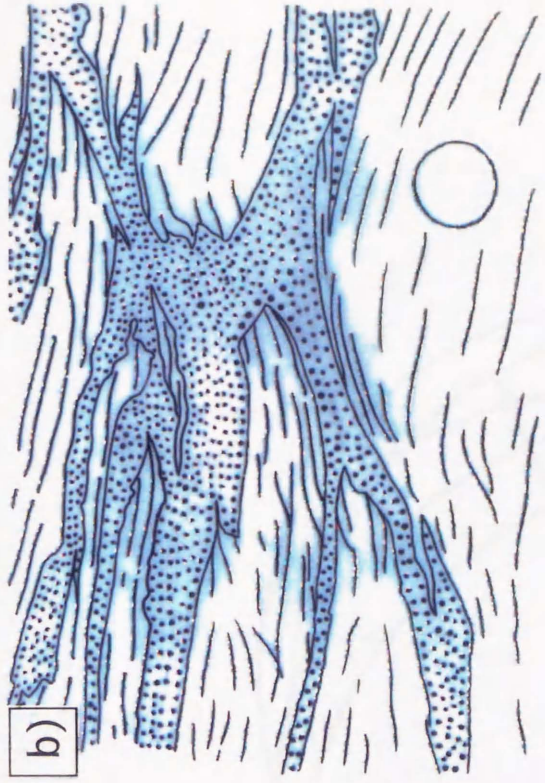
Fig. 3.5. a) Photograph showing the structure of melt-filled fractures around the Nagano migmatite. b) Sketched profile of photograph (a). dot: granitic part. strip: metapelite. c) Photograph showing the structure of melt-filled fractures around the Older Ryoke granite.
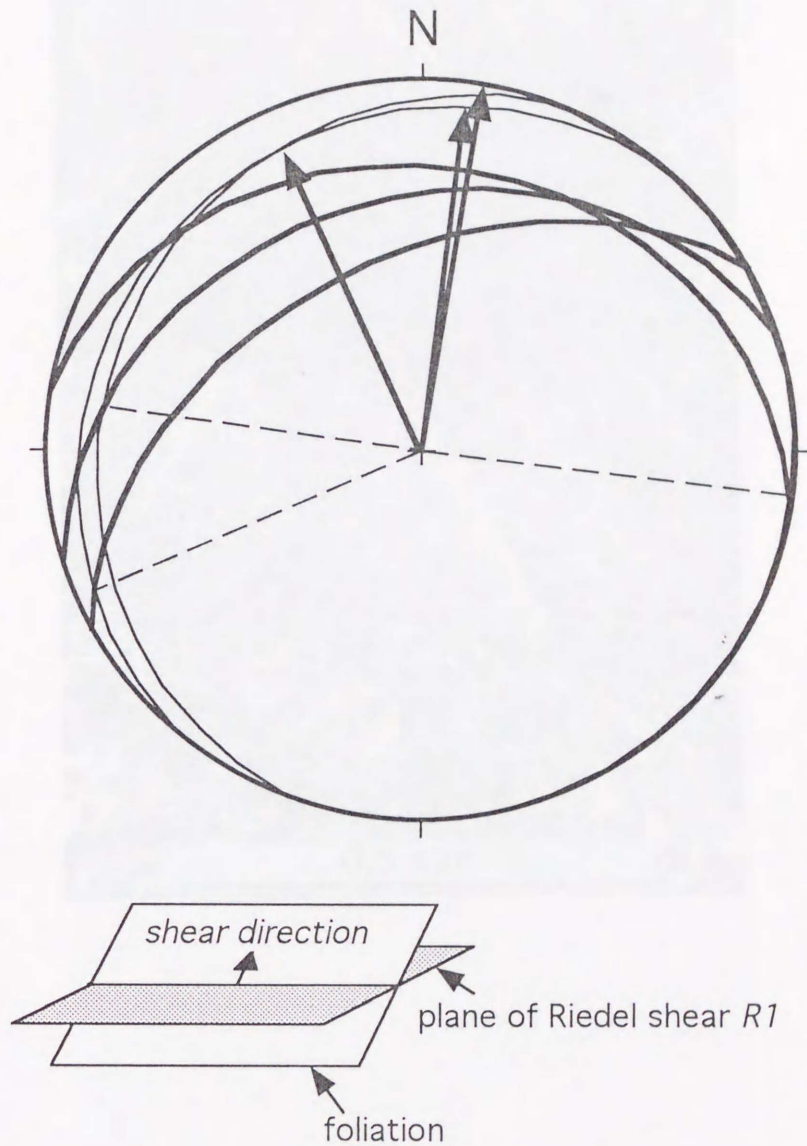
Fig. 3.6.   Diagram showing the shear direction (arrows) of the melt-filled fractures in the metapelites around the Iwakuni Century Golf Course.   Thin solid girdles, thick solid girdles, and dashed lines represent foliation, plane of Riedel shear R_1, and intersection between the former two, respectively.   Lower hemisphere equal area projection.

0.5 mm
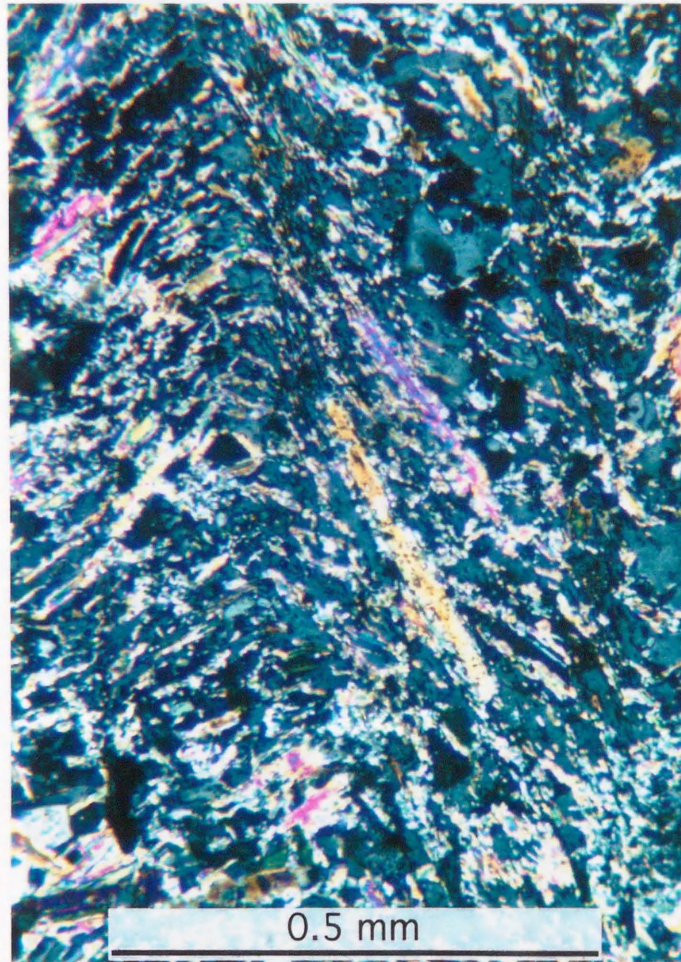
Fig. 3.7. Microphotograph showing the axial plane cleavage of crenulation type of D_1 fold is masked by the K-feldspar porphyroblast.
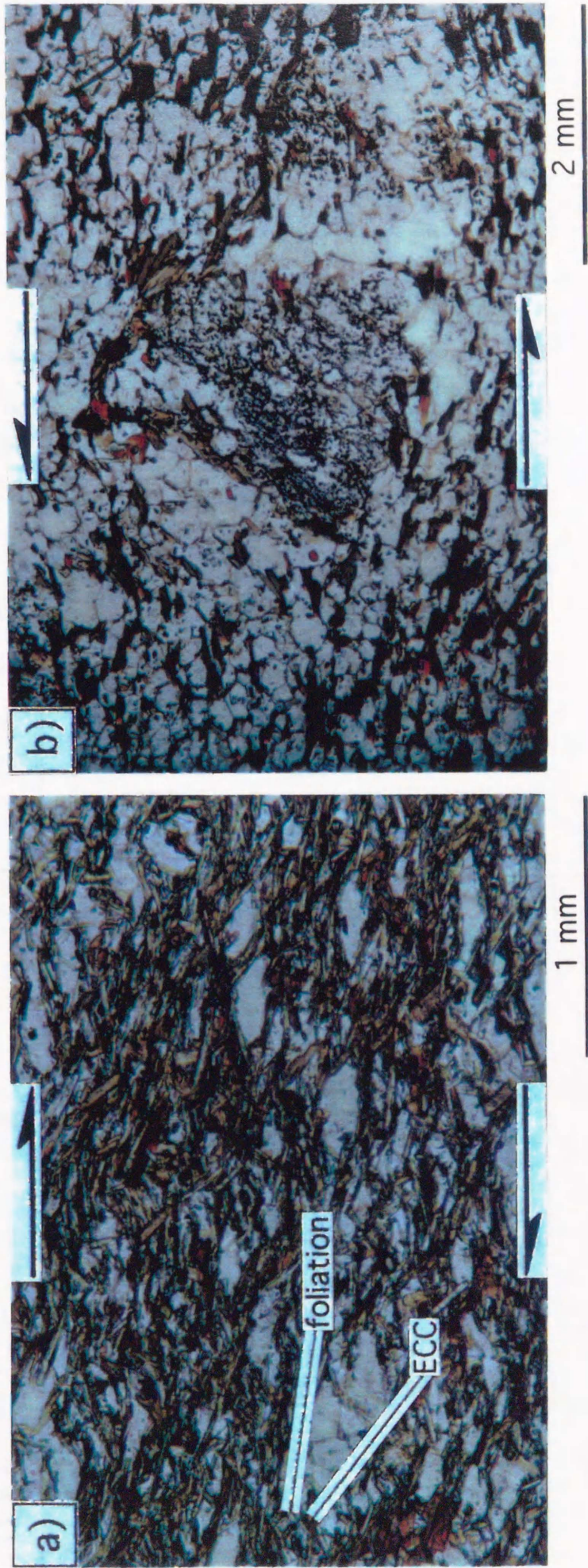
Fig. 3.8. Microphotographs showing asymmetric textures in metapelites of the biotite and cordierite zones. Plane-polarized light. a) extensional crenulation cleavage. b) rotation of cordierite porphyroblast. See text for details.
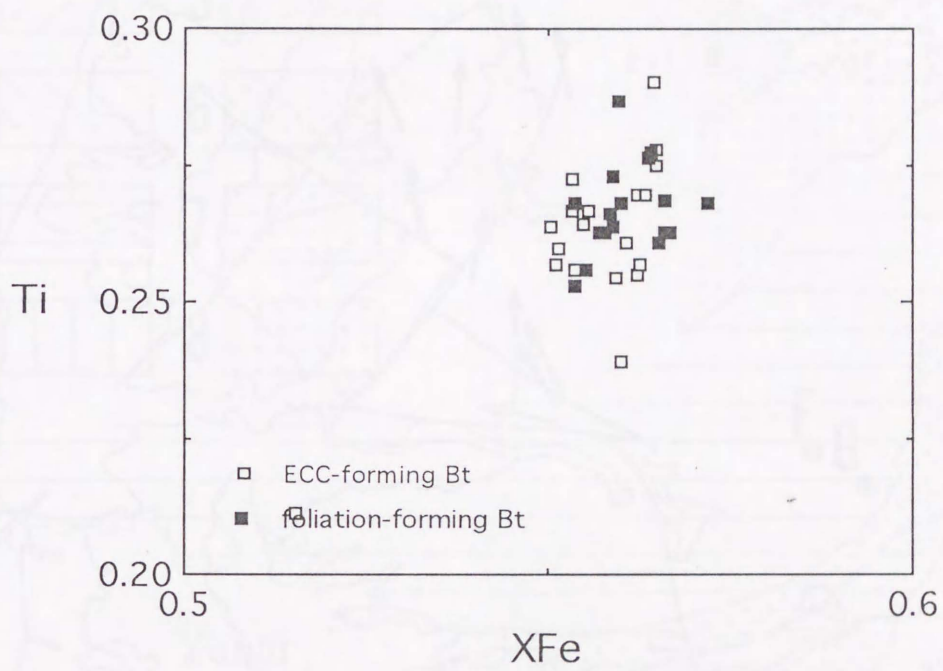
Fig. 3.9. Ti versus XFe [Fe/(Fe+Mg)] for biotite in metapelites from the biotite zone. Numbers of ions on the basis of 22 oxygens.

Fig. 3.10. Diagram showing the shear sense of the asymmetric texture in metapelites (closed arrows).
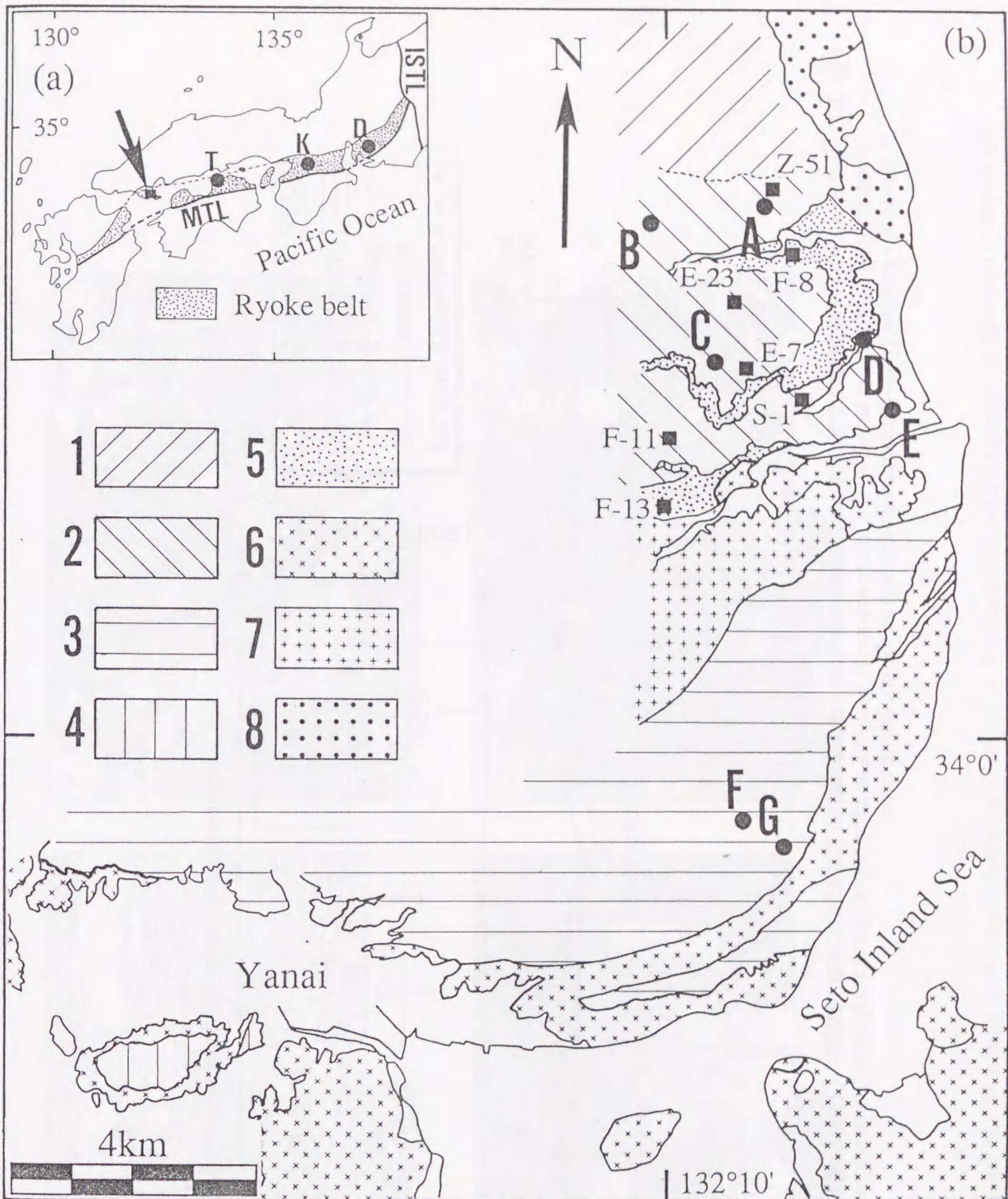
Fig. 3.11. Geological map of the Ryoke metamorphic belt in the Yanai district (simplified from Okudaira *et al.*, 1993). a) Index map of the investigated area. MTL : Median Tectonic Line. ISTL : Itoigawa-Shizuoka Tectonic Line. D : Dando district. K : Kasagi district. T : Teshima district. b) Geological and metamorphic zonation map. 1 - 4 : Ryoke metamorphic rocks (1 biotite zone, 2 cordierite zone, 3 garnet zone, 4 sillimanite zone). 5 : migmatite zone. 6 and 7 : Ryoke granites (6 : Older granites, 7 : Younger granites). 8 : Hiroshima granites. The locations of samples for both petrological and microstructural analyses are shown by squares and dots respectively. Closed circles denoted by A, B, C, D, E, F, and G indicate localities of samples A, B, C, D, E, F, and G. Closed squares indicate localities of samples for petrological analyses of metamorphic temperatures.
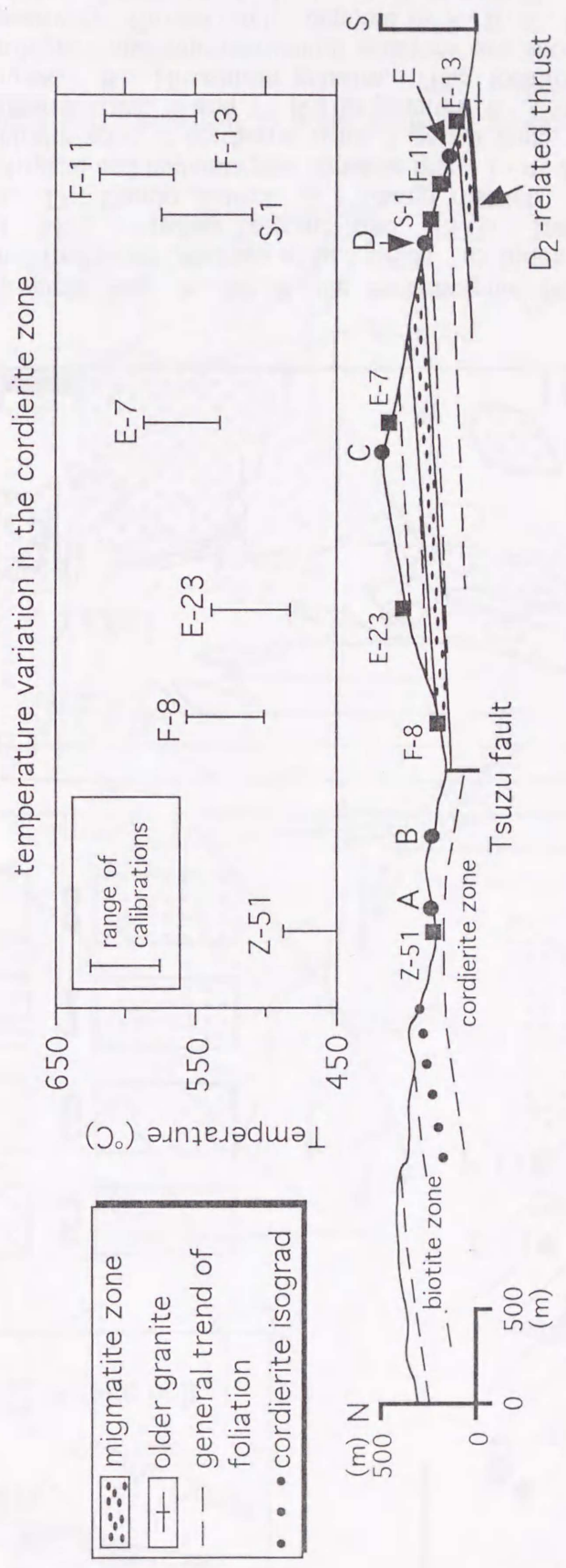
Fig. 3.12. Schematic cross section across the cordierite zone from north to south (Okudaira et al., 1993). Closed circles and closed squares indicate the structural positions of samples (metacherts) for microstructural analyses and for petrological analyses of metamorphic temperature respectively. An inset diagram shows the metamorphic temperature variation in the cordierite zone.
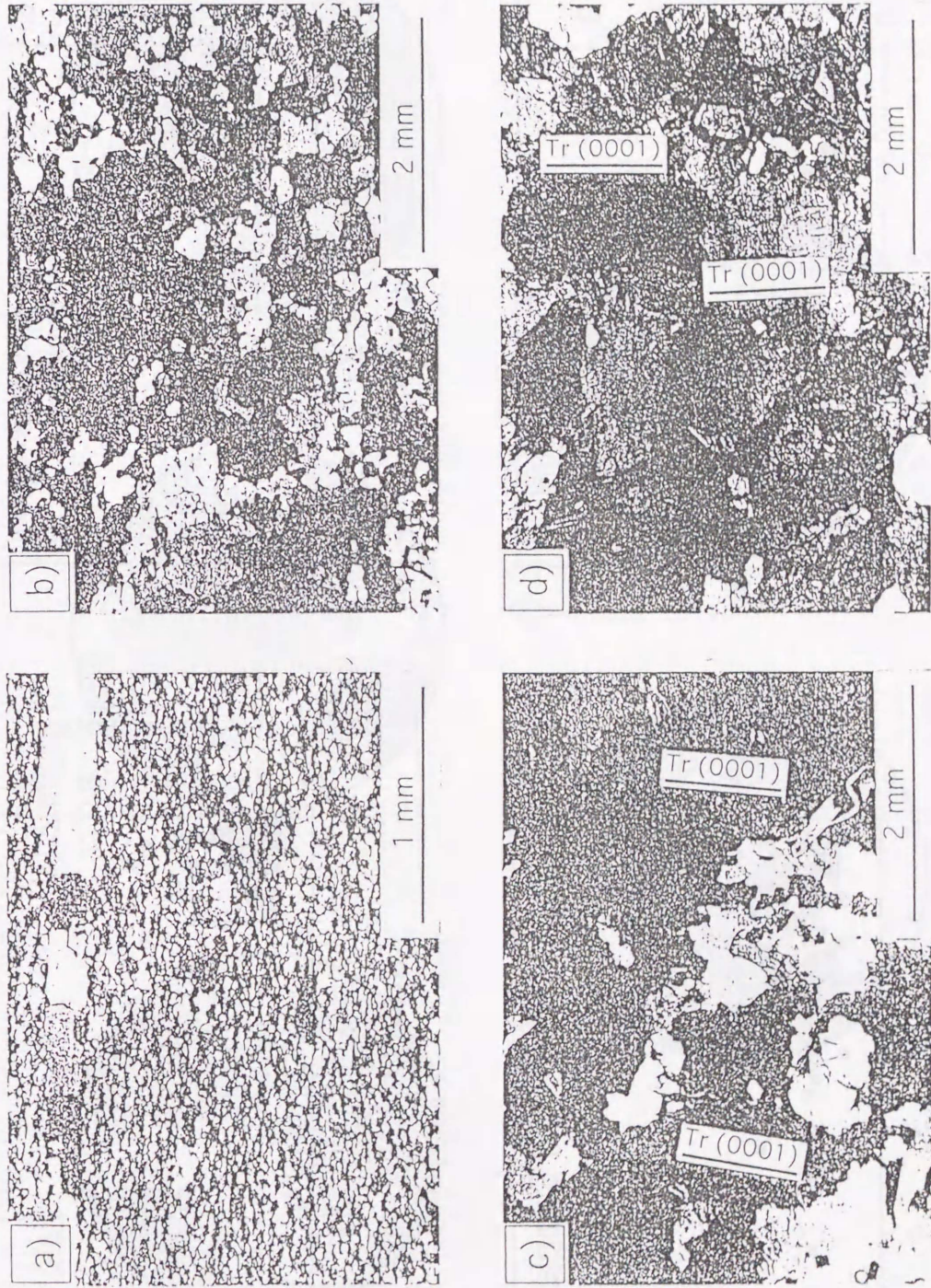
Fig. 3.13. Optical microstructures of quartz grains in the metacharts. a) Sample A. b) Sample C. c) Sample D. d) Sample G. Tr (0001) denotes the trace of the basal plane in the quartz.
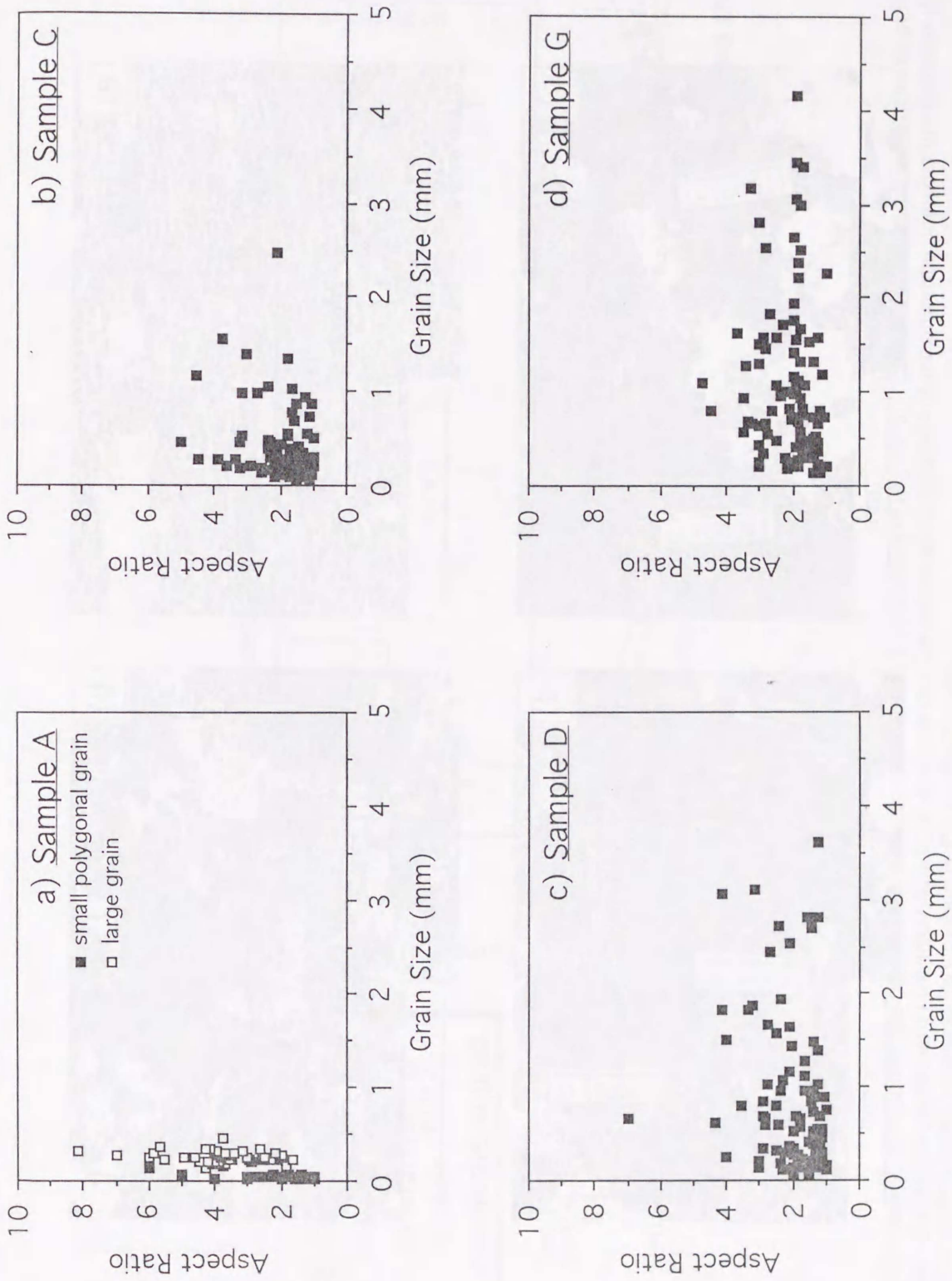
Fig. 3.14. Grain size (geometric mean of the length of long-axis and that of short-axis of quartz) versus aspect ratio (ratio of the length of long-axis to that of short-axis of quartz). a) Sample A. Open square: small grain. Closed square: large grain. b) Sample C. c) Sample D. d) Sample G.
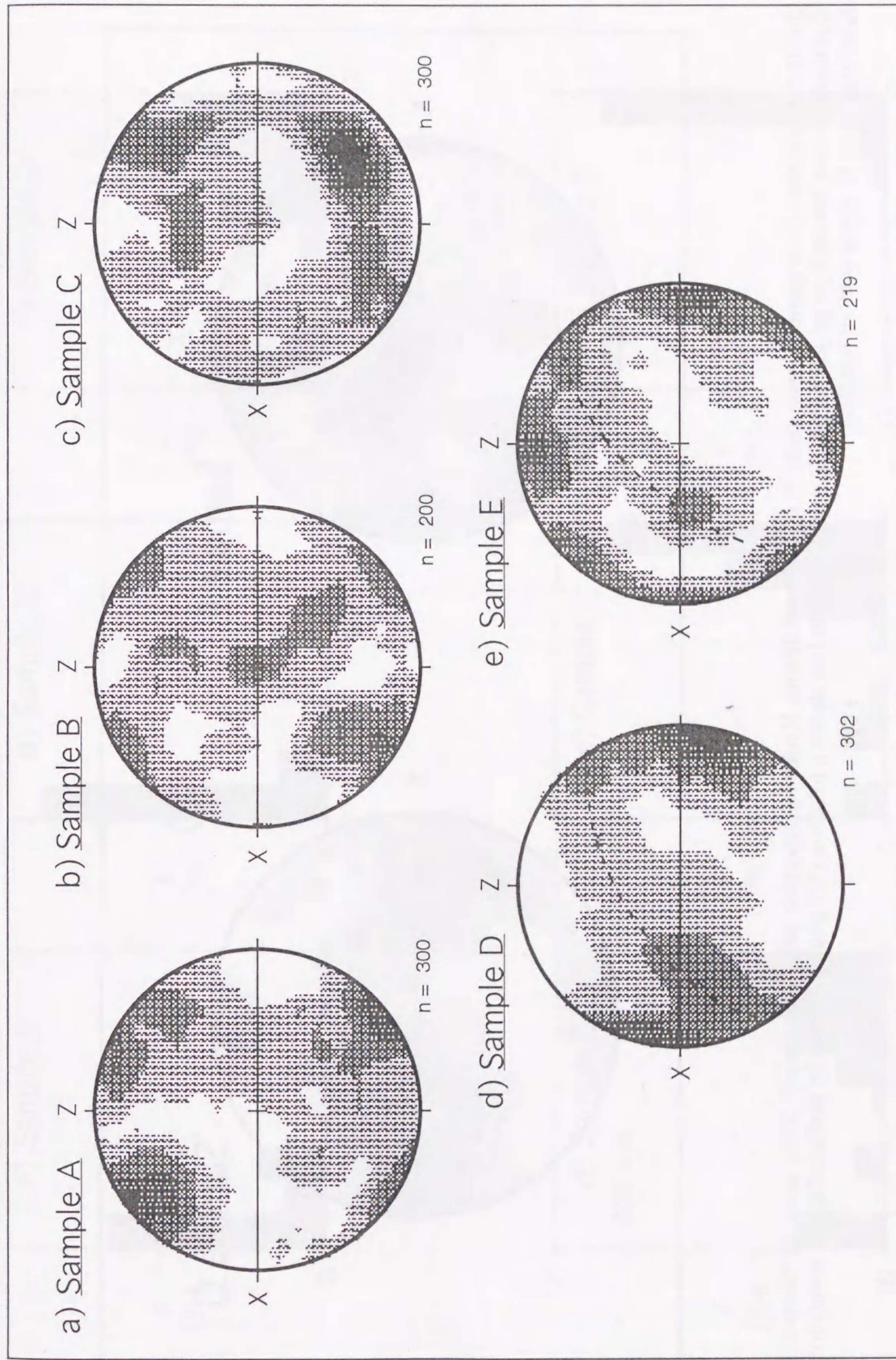
Fig. 3.15. Quartz c-axis fabrics from cordierite zone metacherts in the Yanai district, Ryoke metamorphic belt. a) Sample A, 300 c-axes. b) Sample B, 200 c-axes. c) Sample C, 300 c-axes. d) Sample D, 302 c-axes. e) Sample E, 219 c-axes. Straight line shows a foliation (XY plane) defined by preferred shape orientation of mica grains. Kamb contours (2 sigma contour interval).
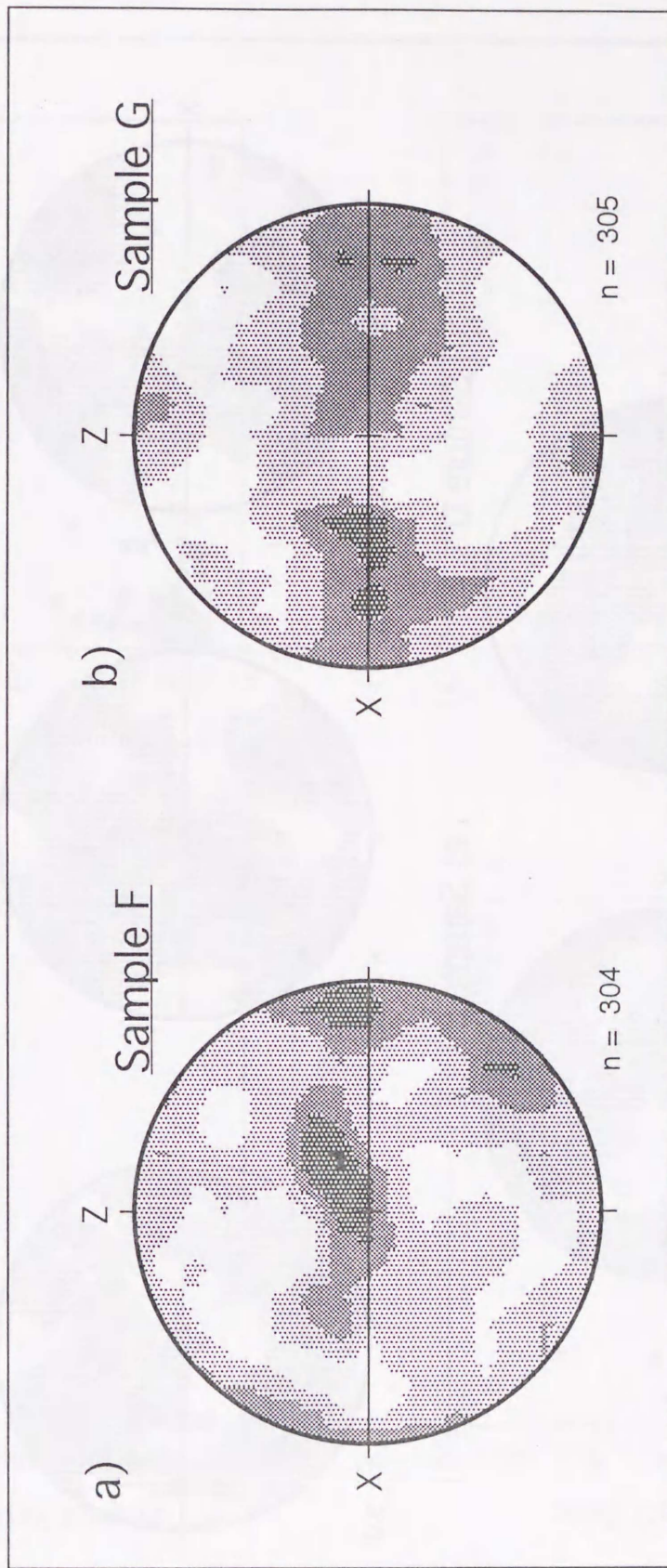
Fig. 3.16. Quartz c-axis fabrics from garnet zone metacherts in the Yanai district, Ryoke metamorphic belt. a) Sample F, 304 c-axes. b) Sample G, 305 c-axes. Equal area, lower hemisphere projection on XZ plane. Straight line shows a foliation (XY plane) defined by preferred shape orientation of mica grains. Kamb contours (2 sigma contour interval).
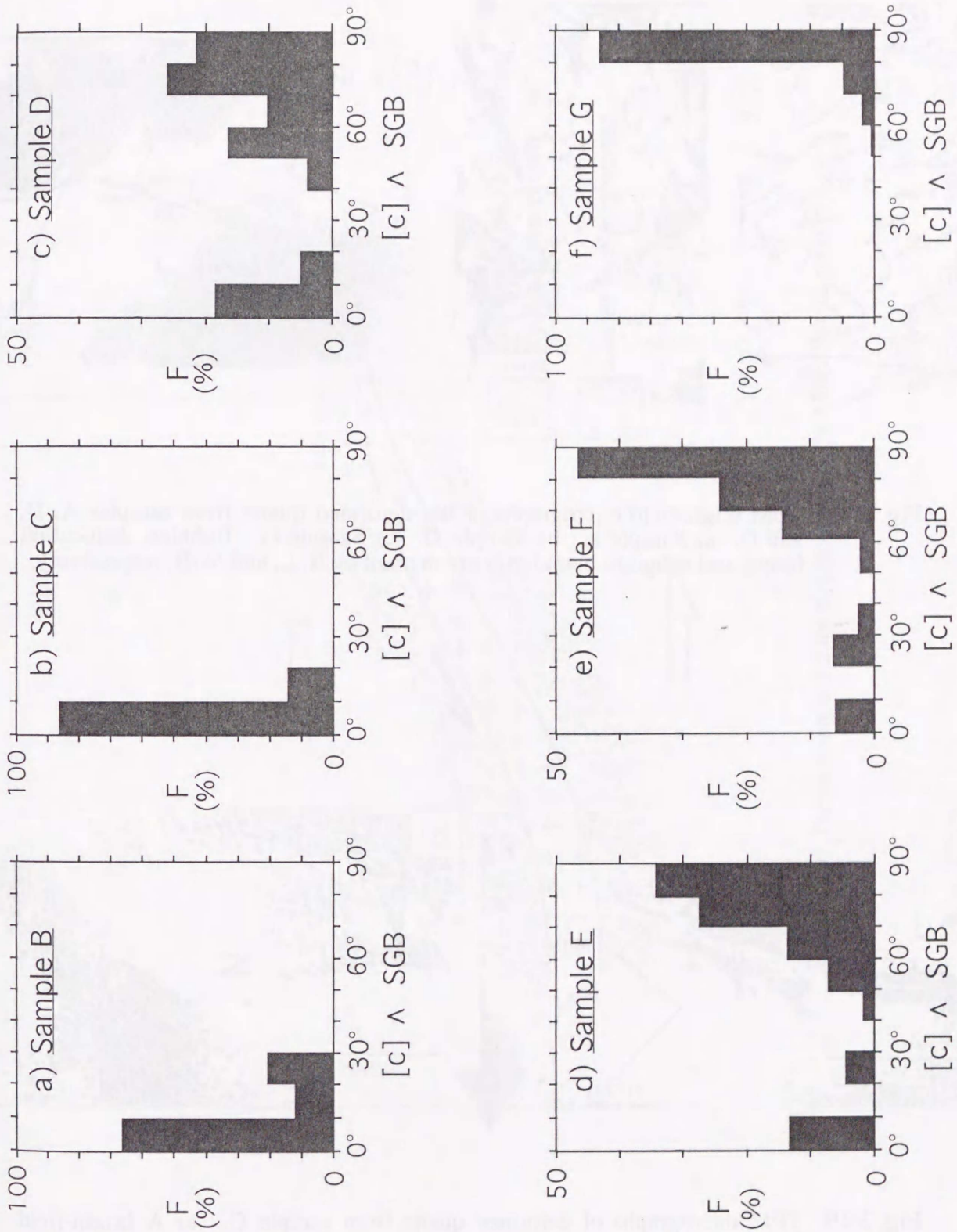
Fig. 3.17. Histogram of the angles between subgrain boundaries and c-axes in subgrains. a) Sample B. b) Sample C. c) Sample D. d) Sample E. e) Sample F. f) Sample G.
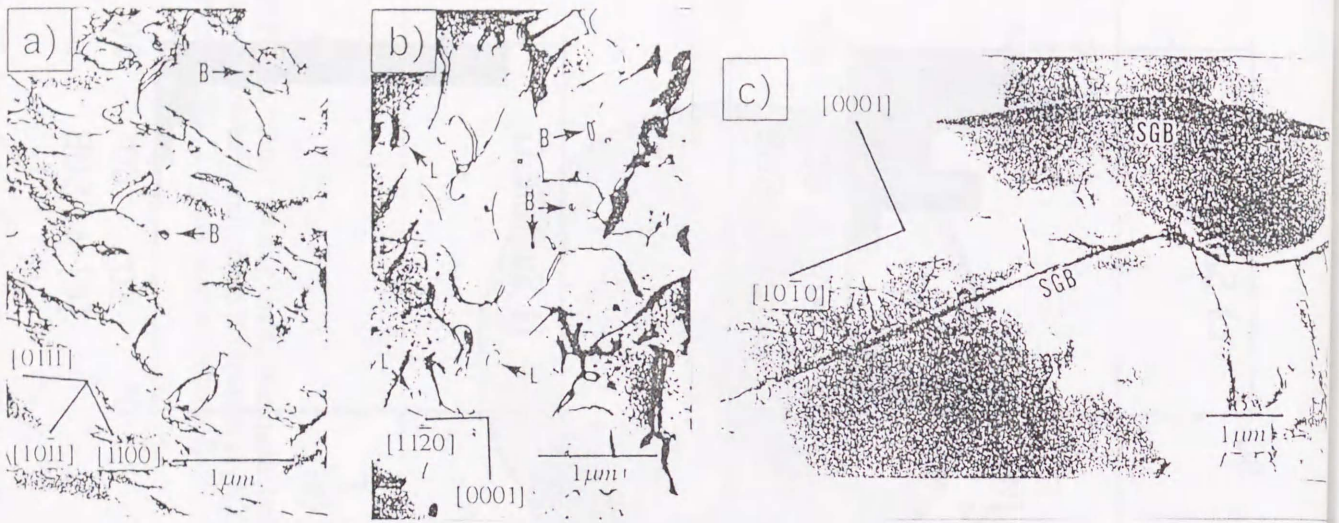
Fig. 3.18. TEM bright-field micrographs of the deformed quartz from samples A, D, and G. a) Sample A. b) Sample D. c) Sample G. Bubbles, dislocation loops, and subgrain boundaries are marked by B, L, and SGB, respectively.
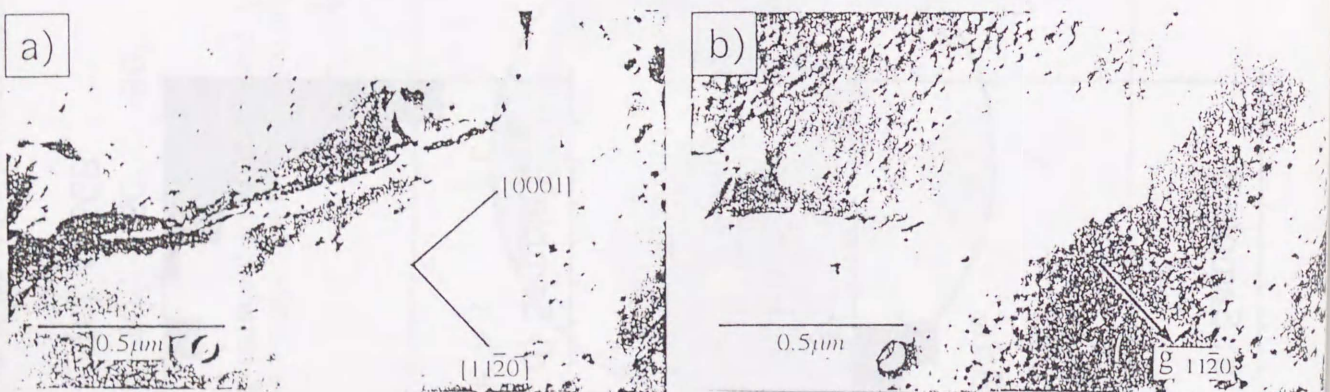
Fig. 3.19. TEM micrographs of deformed quartz from sample G. a) A bright-field image of free dislocation. b) A dark-field image of the same area. Diffracting vector $g = [11\bar{2}0]$.
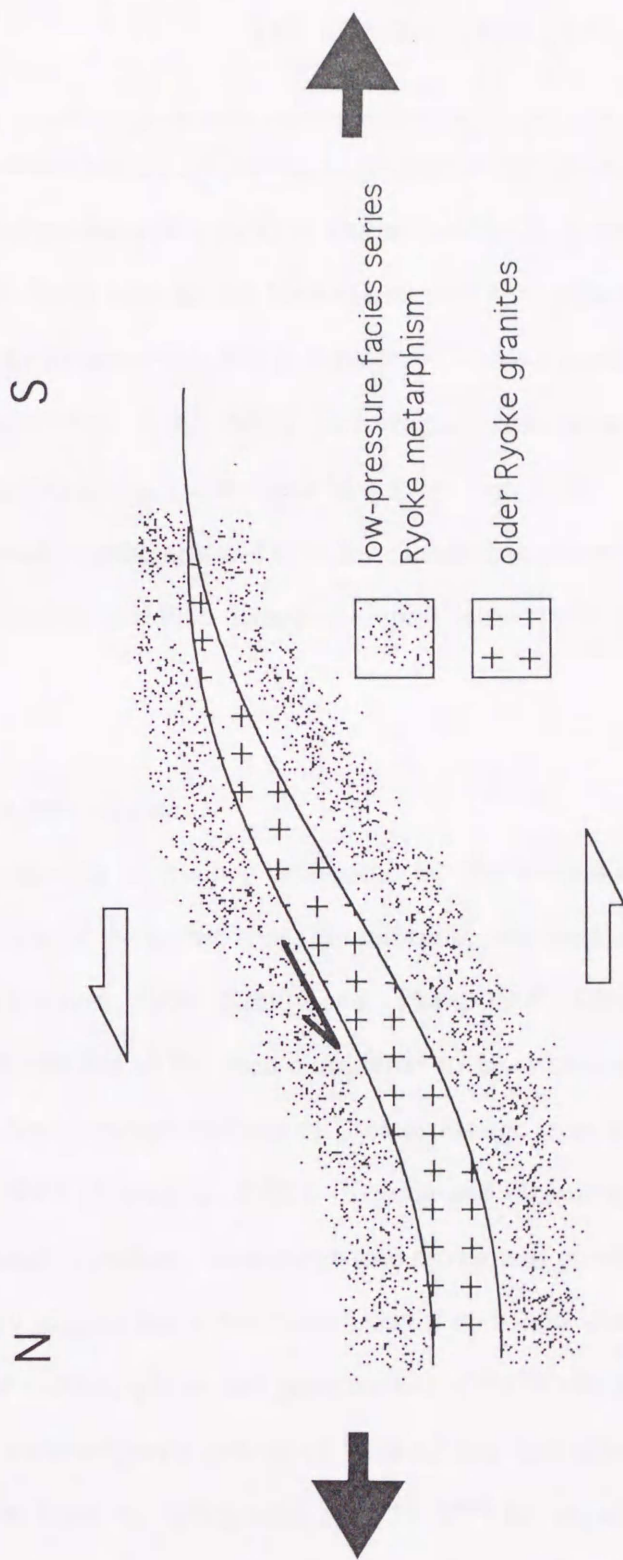
Fig. 3.20. Tectonic model for the emplacement of the Older Ryoke granites.

D2 deformation is characterized by the rearrangement of the geological structure of the Older Ryoke granitoids and metamorphic rocks produced during D1, giving rise to their displacement along the low-angle faults such as the Kitaoshima and Yuu thrusts (Okudaira et al., 1993). During D2, the Ryoke metamorphic belt is considered to have significantly been uplifted (Hara et al., 1991; Okudaira et al., 1992, 1993). Deformation structures of D2 is well recognized at the Hirarehana peninsula of the Yashirojima island (see Fig. 1.2b). In this Chapter, the author will describe deformation structures of D2 in the Hirarehana peninsula to clarify the movement picture of D2 deformation, and then discuss the uplift tectonics of the Ryoke metamorphic belt in the district.

4.1: The Kitaoshima granodiorite

The Hirarehana peninsula is mainly composed of the Gamano granodiorite, Kitaoshima granodiorite, metapelite of the garnet zone, amphibolite, and metabasic rocks as shown in Fig. 4.1 (Kojima and Okamura, 1968; Sakurai and Hara, 1990; Okudaira et al., 1993). The Kitaoshima granodiorite has so far been considered to be a fragment of the continental crust which predates the Ryoke metamorphism of Cretaceous age (e.g., Kojima and Okamura, 1968; Sakurai and Hara, 1990; Hara et al., 1991). Kojima and Okamura (1968) considered that the features such as agmatic structure, metamorphosed dykes, and granitizated fault observed in the granodiorite strongly suggest that it had been brought up to the shallow tectonic level of brittle fracturing before the metamorphism and granitization of the Ryoke age began and therefore that the granodiorite is an orthogneiss (so-called "Kitaoshima orthogneiss"). However, the U-Pb ages of zircon grains from the orthogneiss are 92 ~ 97 Ma (unpublished data; Herzig et al., 1995). These ages are consistent with those (95 ~ 101 Ma) of the Gamano granodiorite (Shigeno and Yamaguchi, 1976; Higashimoto et al., 1983; Nakajima et al., 1993; unpublished data; Herzig et al., 1995), though the Kitaoshima granodiorite is intruded by the Gamano granodiorite (Okudaira et al., 1993). Honma (1974), Honma and Sakai (1975), and Shigeno

and Yamaguchi (1976) assumed on the basis of the petrological features such as mineral assemblages and major and minor elements of the Kitaoshima orthogneiss and Gamano granodiorite that they are crystallized from the same original magma. The Kitaoshima and Gamano granodiorites can be assumed to belong to the Older Ryoke granitoids.

4.2: Geological and deformation structures in the Hirarehana peninsula

As mentioned above, the Hirarehana peninsula is mainly composed of the Gamano granodiorite, Kitaoshima granodiorite, metapelite of the garnet zone, amphibolites, and metabasic rocks. The Gamano granodiorite and Kitaoshima granodiorite have a distinct foliation on mesoscopic scale, and are parallel to each other. The metapelites of the garnet zone and amphibolites are observed as xenoliths of the granodiorites, although these are also metabasic rocks as dyke. The foliations of the metapelites and granodiorites are parallel to each other and the lithologic boundaries between them are parallel to the their foliations. The foliations of the metabasic rocks and also parallel to those of the granodiorites and the lithologic boundaries between them are parallel to the their foliations. However, the amphibolites do not show any their foliation, and are fractured and intruded in network fashion by granitic materials.

The Kitaoshima granodiorite is divided in to three layers: coarse-grained layer, porphyroblastic layer, and fine-grained layer (Sakurai and Hara, 1990) as shown in Fig. 4.2. The former two layers are main constituent of the orthogneiss. The fine-grained layer has been considered to be shear zone formed by dynamic recrystallization of the coarse-grained and porphyroblastic layers (Sakurai and Hara, 1990; Okudaira et al. 1993). All the layers show distinct foliation which is characterized by preferred shape orientation of plagioclase, K-feldspar, and biotite grains. Following Kojima and Okamura (1968), poles of the foliation of the Kitaoshima granodiorite are shown in Fig. 4.1. The foliation is nearly flat-lying as a whole, though wavy folds on mesoscopic scale is reflected on the diagram. From the distribution of π-poles, π-circle (dashed circle) and π-axis (cross) can be estimated, as shown in the diagram, and then the π-axis points to N65°E, plunging at 12°. The layers of the Kitaoshima granodiorite are parallel to each other, although the fine-grained layer often truncates the coarse-

59

grained and porphyroblastic layers. Microfabric diagram of plagioclase (010) planes of the coarse-grained and porphyroblastic layers is characterized by orthorhombic symmetry with respect to the foliation surface and incomplete girdle around the axis normal to the foliation surface (Fig. 4.3). This observation indicates that the plagioclase (010) planes were oriented under coaxial deformation. In the coarse-grained and porphyroblastic layers, the biotite forms thin layers or trains of clots, arranged parallel to each other (Fig. 4.2a). On the foliation surface, the biotite clots are not elongate but show a circle shape (Fig. 4.4). These observations suggest that the biotite clots, as well as the fabrics of plagioclase (010) planes, were formed under pure shear deformation and therefore that the foliation of the coarse-grained and porphyroblastic layers was formed near coaxial (pure shear) condition. The fine-grained layer often truncates the coarse-grained and porphyroblastic layers at low-angles, and shows a distinct foliation (S2) which is parallel to the layer cutting across the foliation of coarse-grained and porphyroblastic layers (Fig. 4.5). The fine-grained layer is a mylonitic shear zone (Sakurai and Hara, 1990). S1-foliation is sometimes dragged along the shear plane, and such the structural relationship indicates top to the SW sense of shear (Fig. 4.5). The deformation related to the formation of the fine-grained layer postdates the deformation related to the formation of the foliation of the coarse-grained and porphyroblastic layers, and then the former is probably compared with D2 deformation in the other area.

4.3: Movement picture of D2 deformation and uplift tectonics of the Ryoke metamorphic belt
In contrast to the coarse-grained and porphyroblastic layers, many asymmetric structures are observed in the fine-grained layer (Fig. 4.6). Figure 4.6a, b shows that isolated metabasic xenolith have wedge-shaped tails and stair-stepping symmetry. Figure 4.6b shows the rotated boudinage of metabasic dyke. These asymmetric structures indicate top to the west sense of shear. Since the structures are only found in the fine-grained layer, the deformation forming the fine-grained layer is dominant in simple shear component. In summary, D1 deformation which formed the foliation of the Kitaoshima granodiorite (coarse-grained and porphyroblastic layers), metapelites, and metabasic rocks is dominant in pure shear component, and D2 deformation which formed the fine-grained layer is dominant in simple shear component and

60

has top to the W ~ SW sense of shear. D2 deformation is related to the uplift of the Ryoke metamorphic belt in the Yanai district, giving rise to the folding and displacement of the thermal structure of M1 metamorphism (Okudaira *et al.*, 1993). The deformation structures of D2 observed in the Hirarehana peninsula indicate the movement picture of the uplift tectonics of the Ryoke metamorphic belt in the Yanai district. In summary, inferred from the observations in Chapters 2, 3, and 4, a possible tectonic model of the Ryoke metamorphic belt in the Yanai district during Cretaceous age is shown in Fig. 4.7.
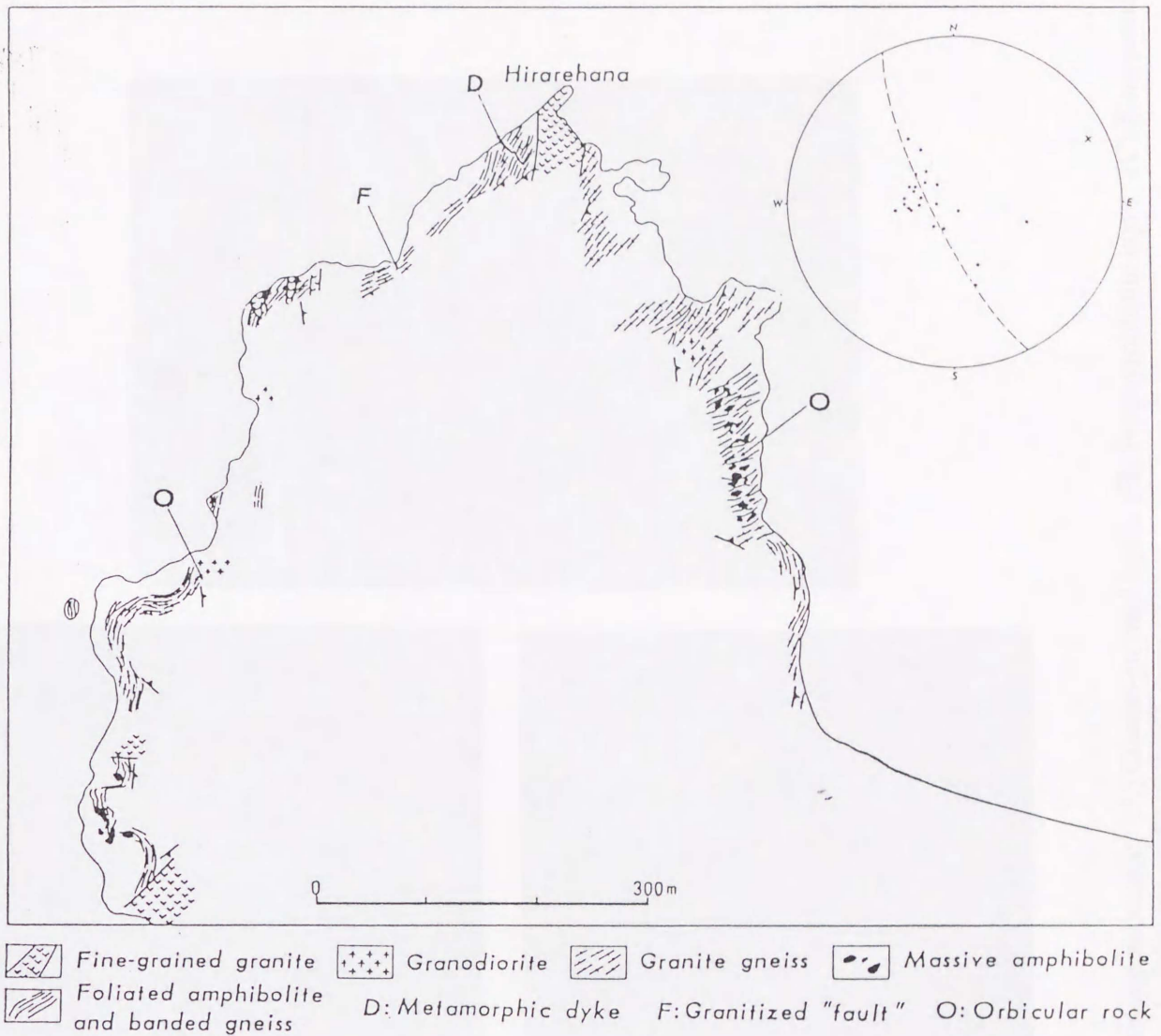
Fig. 4.1. Route map of the Hirarehana peninsula in the Yashirojima island and an inset diagram shows the π-poles of foliation of the Kitaoshima granodiorite (after Kojima and Okamura, 1968).
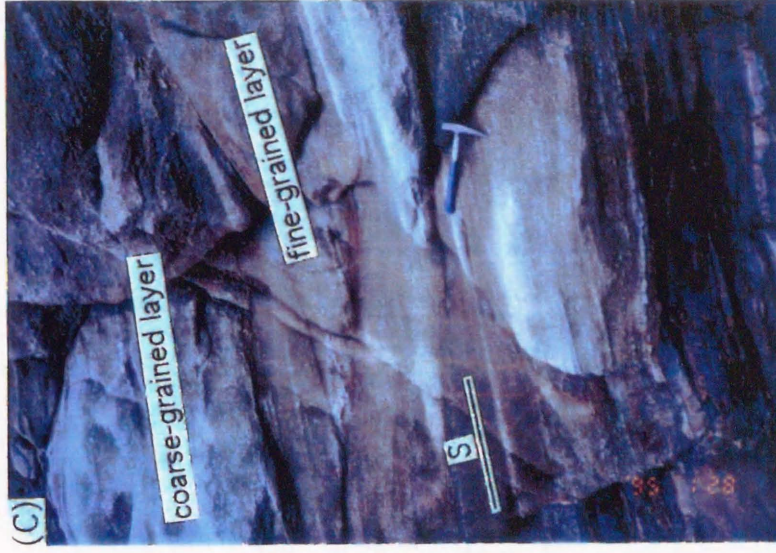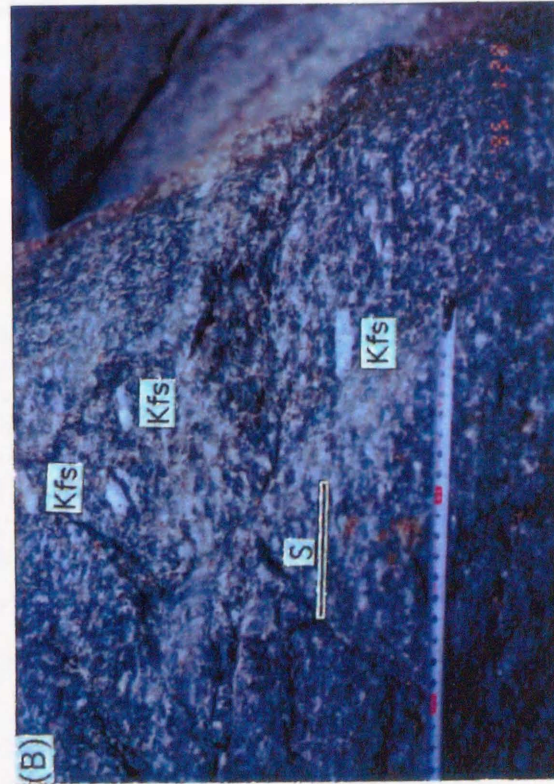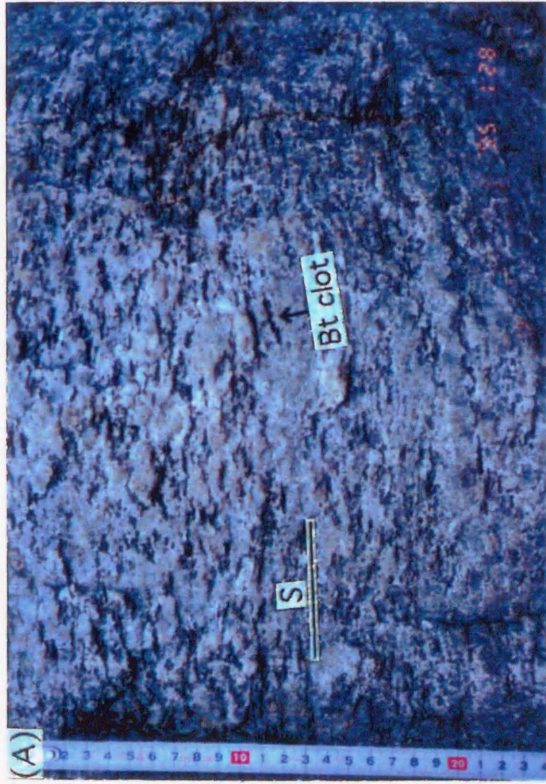
Fig. 4.2. Photographs showing the Kitaoshima granodiorite (A) Coarse-grained layer. (B) Porphyroblastic layer. (C) Fine-grained layer. S1 and Kfs denote S1-foliation and K-feldspar porphyroblast, respectively.
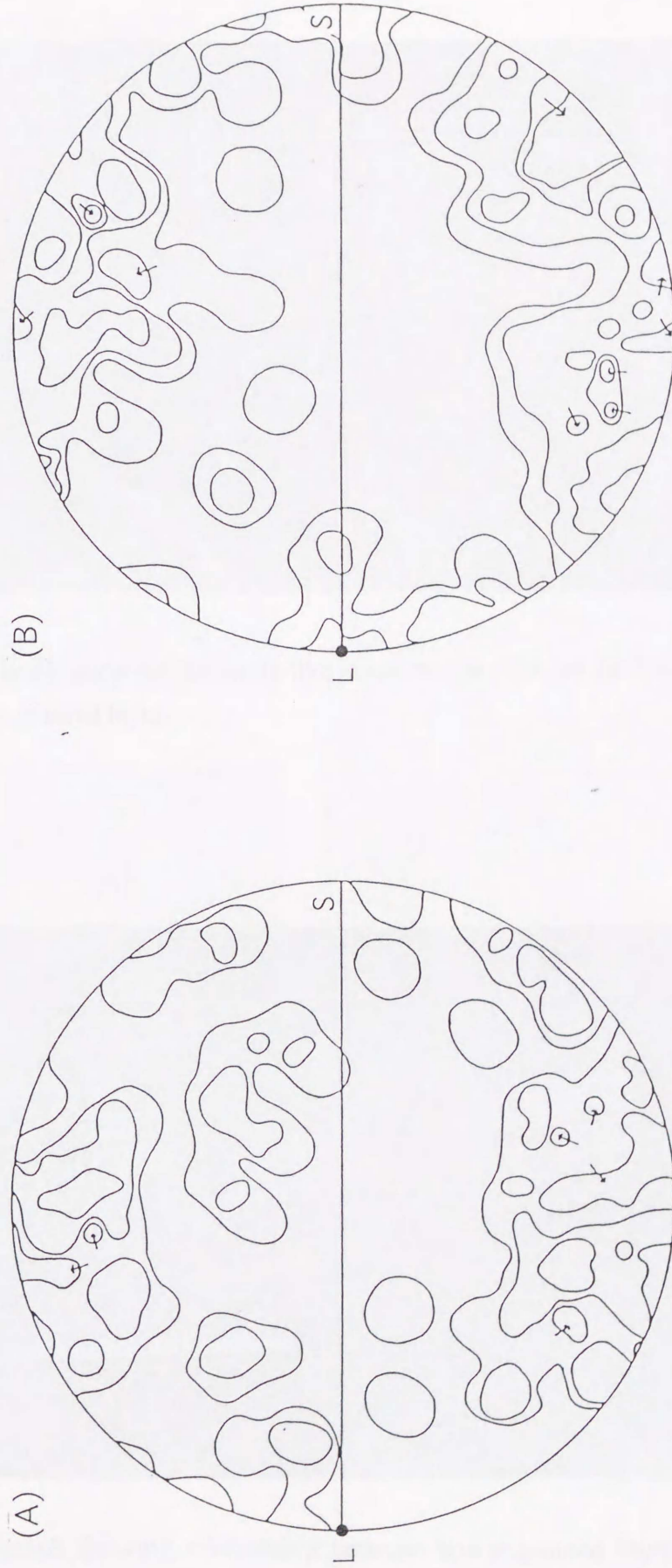
Fig. 4.3.   π-diagram of the plagioclase (010) plane of the coarse-grained layer (A) and the porphyroblastic layer (B).   Lower hemisphere equal-area projection. S and L indicate the foliation and lineation, respectively.
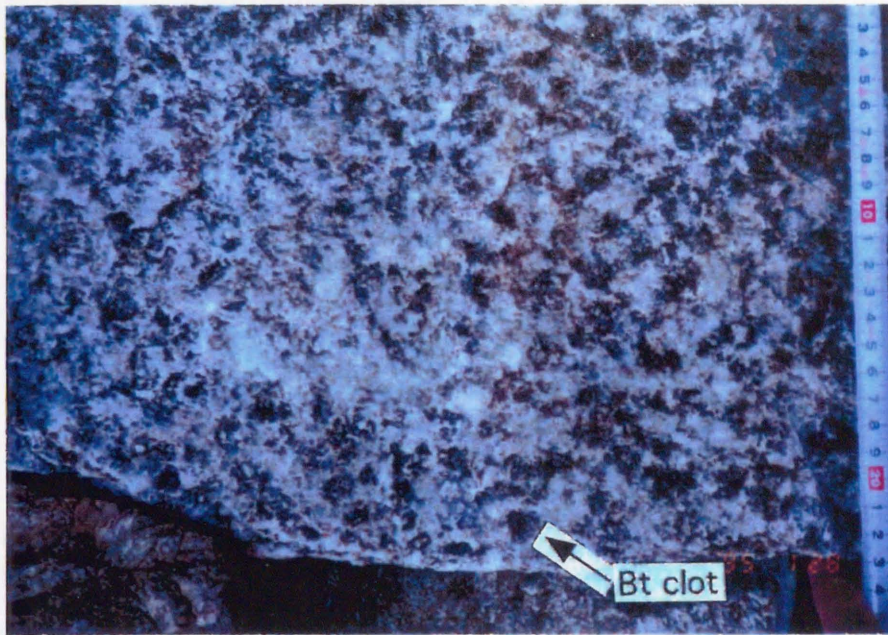
Fig. 4.4. Photograph showing the circle-like shape biotite clots on the foliation plane of the coarse-grained layer.
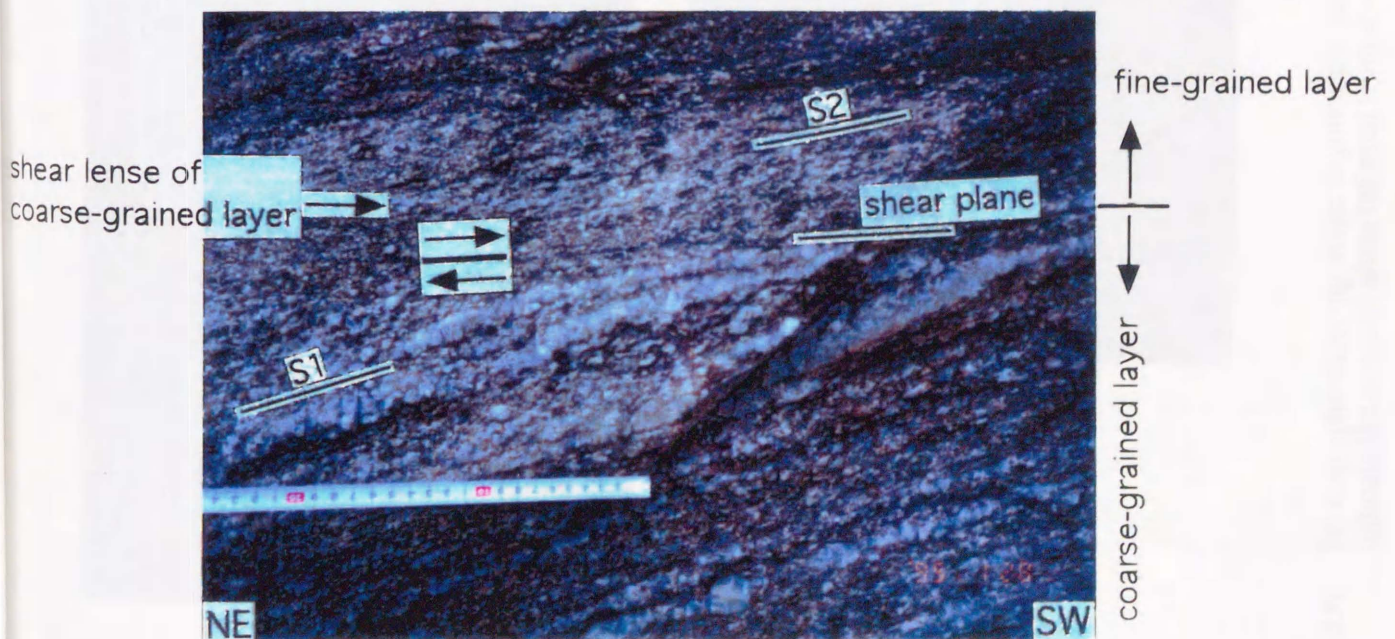
Fig. 4.5. Photograph showing relationship between coarse-grained layer and fine-grained layer. S1: S1-foliation. S2: S2-foliation. Arrows of photograph indicate the sense of shear inferred from the asymmetric structures See text for details.
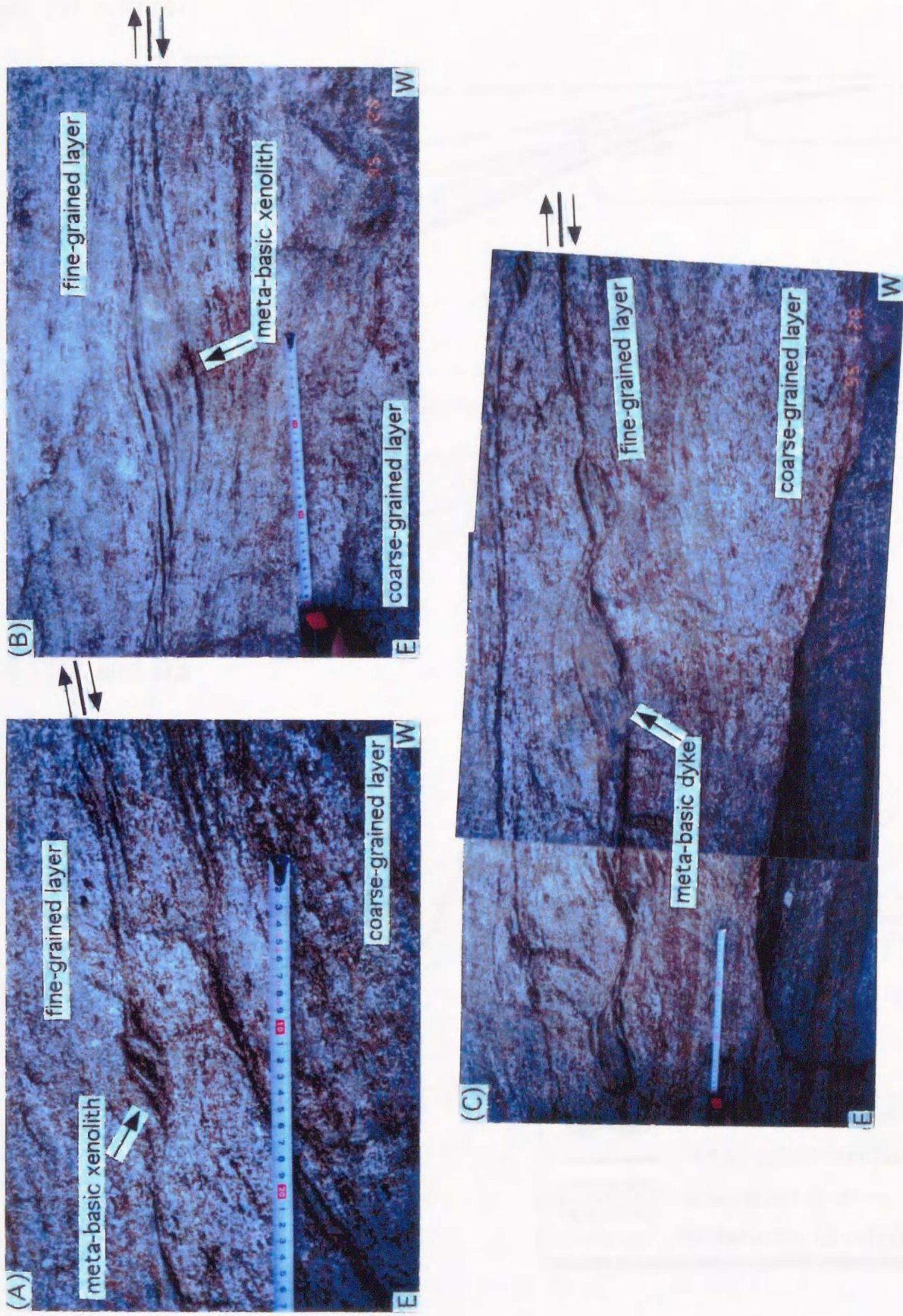
Fig. 4.6.   Photographs showing some asymmetric structures in the fine-grained layer.   Arrows on upper right-hand of each photograph indicate the sense of shear inferred from the asymmetric structures.   See text for details.

a) D1 and M1

bt zone

crd zone

sil zone

grt zone

b) initiation of D2

bt zone

crd zone

sil zone

grt zone

c) D2 and D3

bt zone

crd zone

sil zone

grt zone

present surface

Direction of regional stress
Active detachment fault
Older Ryoke Granites
Metamorphic zone boundary
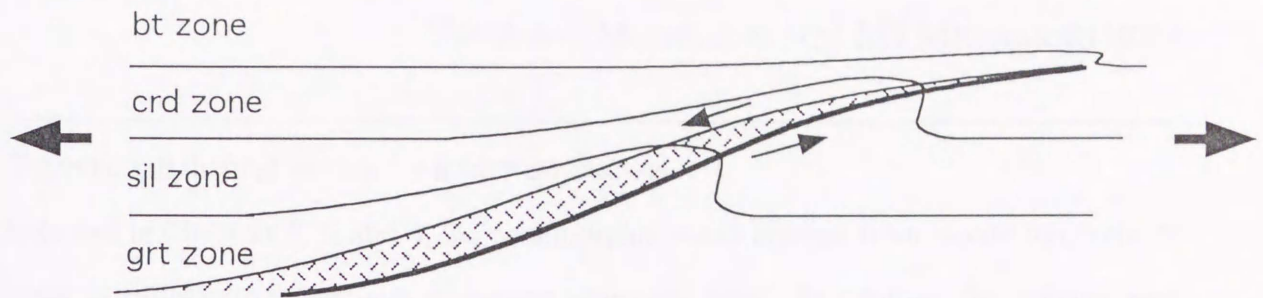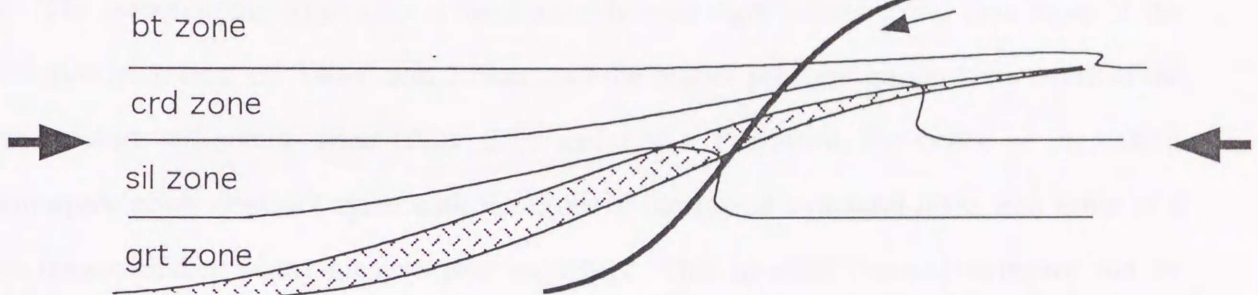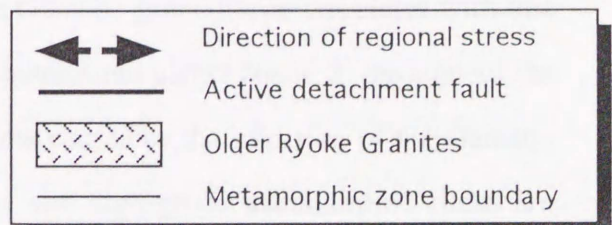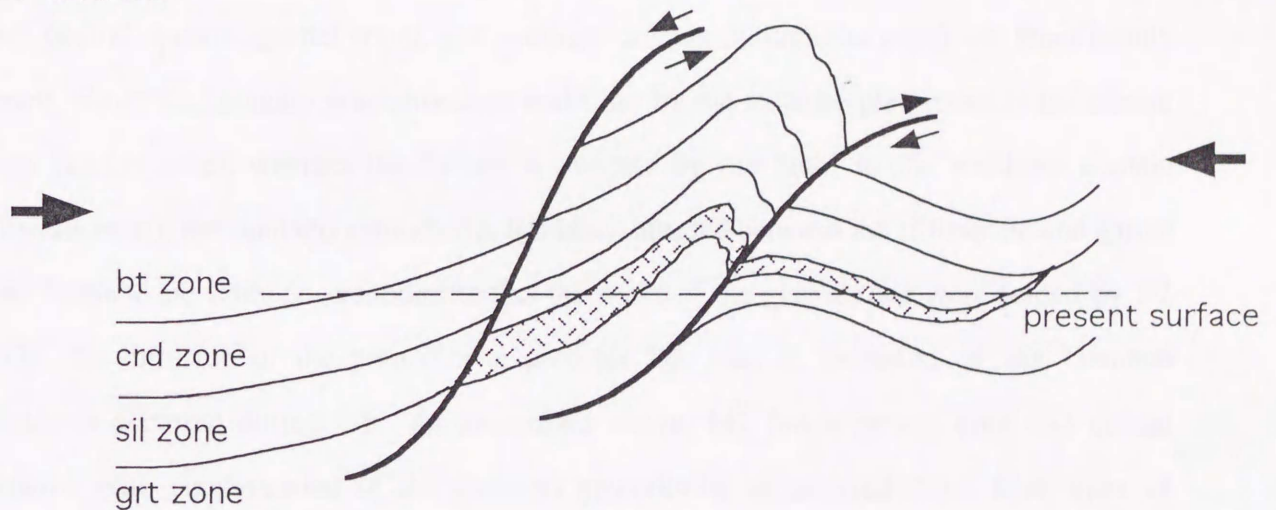
Fig. 4.7. A possible tectonic model for the Ryoke metamorphic belt in the Yanai district during Cretaceous.

5.1: Tectonic and thermal models for numerical analysis

As described in Chapters 2, 3, and 4, the metamorphic zones arrange from biotite to cordierite to garnet to sillimanite zones with increasing structural level. In contrast, the metamorphic grade increases from the biotite zone, through the cordierite and sillimanite zones, to the garnet zone. The metamorphic conditions of the cordierite zone significantly lower than those of the garnet zone by at least *ca.* 140°C and 2 kbar, and the higher pressure garnet zone overlies the lower pressure sillimanite zone (Figs. 2.1b and 2.9). Therefore, the order of increasing metamorphic grade does not agree with the order of increasing structural level, and there is a major discontinuities in the metamorphic sequence. This inverted thermal structure can be explained as the result of large-scale post-metamorphic faulting after D1 (Okudaira *et al.*, 1993). In fact, the geological structures among the northern domain (biotite and cordierite zones), central domain (garnet zone), and southern domain (sillimanite zone) are significantly different. Since the Gamano granodiorite is underlain by the metamorphic rocks in the central domain (garnet zone), whereas the former is overlaid by the latter in the southern domain (sillimanite zone), the Gamano granodiorite has been intruded between the sillimanite and garnet zones. Because the Gamano granodiorite and the rocks of the garnet zone were folded by D2 and D3, the intrusion of the granodiorite predates D2, that is, intrusion of the Gamano granodiorite occurred during D1. As mentioned above, M1 has a strong time and spatial association with emplacement of the Gamano granodiorite as inferred from four lines of geological evidence as follows; 1) distribution of the Gamano granodiorite correlates with that of the high-grade metamorphic zones such as the sillimanite and garnet zones, 2) throughout the high-grade metamorphic zones, distinct contact aureoles caused by the intrusion of the Gamano granodiorite are lacking, 3) geological structures of the high-grade metamorphic rocks are nearly compatible with those of the Gamano granodiorite, and 4) radiometric ages of the metamorphic rocks are roughly compatible with those of the Gamano granodiorite. These geological evidences suggest that M1 resulted from the intrusion of the Gamano granodiorite

during D1. From these circumstances, a possible tectonic model for the Ryoke metamorphic belt in the district has been proposed by Okudaira *et al.* (1993, 1994, 1995) as shown in Fig. 5.1. The tectonic model is 1) the low- to flat-angle intrusion of the Gamano granodiorite during D1 resulted in M1, and 2) after D1 the metamorphic sequence of M1 was modified by the deformation during D2 and D3. According to the tectonic model, to clarify of the thermal effects of the emplacement of the Gamano granodiorite, I conduct simple thermal model for M1 by using 1-D numerical simulation as bellow.

5.2: Numerical analysis

5.2.1: Methods

An one-dimensional heat transfer equation with fluid advection term is written as

$$\rho_m C_m \frac{\partial T}{\partial t} = K \frac{\partial^2 T}{\partial z^2} - C_f \frac{\partial (Tu)}{\partial z} + A \tag{5.1}$$

where ρ_m, density of rock; C_m, specific heat of rock; T, temperature; t, time; K, thermal conductivity; z, vertical coordinate measured from the earth's surface; C_f, specific heat of fluid; u, mass fluid flux; and A is heat production of radioactive. Density and specific heat of magma are assumed to be similar with those of rock, according to De Yoreo *et al.* (1989), Hanson & Barton (1989), Rothstein & Hoisch (1994), and others. Equation (5.1) was solved numerically using an explicit finite-difference method with a 1,000 m array spacing (Δz) and a 3.15×10^9 sec time step (Δt). The parameters used in the numerical models are shown in Table 5.1.

Production of heat by the magmatic crystallization (latent heat) and consumption of heat during the endothermic reactions have been calculated assuming reactions to be a continuous linear function of temperature between liquidus and solidus temperature ($T_{liq} \sim T_{sol}$) and between endothermic reaction interval ($T_{start} \sim T_{end}$), respectively. According to Hanson and Barton (1989), I have used the crystallization intervals ($T_{liq} \sim T_{sol}$) of ($950 \sim 750°C$) and ($1050 \sim 850°C$) for the initial intrusion temperature (T_{int}) of 900 and 1000°C, respectively. Here after, the former is called as Model 1 and the latter is called as Model 2 (Fig. 5.2). For ΔH of crystallizing magma, I have taken the value of 3.35×10^5 J kg^{-1}, using data for plagioclase,

quartz, and K-feldspar (Wells, 1980). In the crystallizing magma, recharge and convection of the magma are not modeled here. In the wall rocks, most dehydration reactions are endothermic and thus consume heat (Peacock, 1989; Spear, 1993). For typical dehydration reactions, the ΔH of reaction is in the range of 60 ~ 100 kJ per mole of volatile evolved (Walther and Orville, 1982). During metamorphism, a typical pelite loses approximately 5 wt% H_2O (Walther and Orville, 1982), which is equivalent to approximately 7.6×10^3 moles m^{-3} of rock. Assuming 60 kJ mole^{-1} for dehydration reactions results in a heat sink of 1.6×10^5 J kg^{-1} (Peacock, 1989). Since the actual metamorphic reactions are too complex to thermal calculations, the dehydration reaction interval between 350 and 800°C is modeled here. It is assumed that rocks initially at temperature below 350°C contain 5 wt% volatiles, and rocks initially at temperature above 800°C contain no volatiles, respectively. For rocks initially at the temperatures within the reaction interval, the volatile content is calculated from the following equation:

$$X_{fw} = X_w (T_{end} - T)/(T_{end} - T_{start}) \quad T_{start} < T < T_{end} \tag{5.2}$$

where X_{fw} is the weight fraction of fluid evolved from the rock at T, and X_w is that of fluid contained in the rock at T_{start}. The production and consumption of heat were incorporated into the numerical models using an effective heat capacity, C^*, and an effective thermal diffusivity, κ^*, for rocks undergoing reactions (Jaeger, 1964; Peacock, 1989; Hanson and Barton, 1989). The effective thermal diffusivity is then calculated from

$$\kappa^* = \frac{K}{\rho_m C^*}, \tag{5.3}$$

where the effective heat capacity (C^*) is defined by

$$C^* = C_m + \left[\Delta H / (T_{liq} - T_{sol}) \right] \text{ for the magmatic crystallization,} \tag{5.4a}$$

$$C^* = C_m + \left[\Delta H / (T_{end} - T_{start}) \right] \text{ for the metamorphic endothermic reactions,} \tag{5.4b}$$

70

where ΔH in Eqs. (5.4a) and (5.4b) is enthalpy of the magmatic crystallization and the metamorphic endothermic reaction intervals, respectively.

The second term on the right hand side of Eq. (5.1) reflects the heat transport by advection. The fluid and solid matrix are assumed to have the same temperature T. The ρ_m must be a volumetric average over the fluid-filled pores and the solid matrix. However, because a substantial fraction of the medium is made up of the solid matrix, which is usually a better conductor of heat than the fluid, it is generally a good approximation to assume the ρ_m as the density of the solid matrix (Hanson, 1992). For the case of thermally driven devolatilization reactions, the fluid mass production rate per unit volume, J_w, resulting from a temperature increase can be expressed as (Peacock, 1989; Hanson, 1992):

$$J_w = \frac{X_{fw}\,\rho_m}{\Delta T_{rxn}}\left(\frac{\partial T}{\partial t}\right)_z \qquad T_{start} < T < T_{end}. \tag{5.5}$$

On the other hand, the fluid production contributed by the crystallization of the magma has been calculated assuming crystallization to be a continuous linear function of temperature between liquidus and solidus temperature. The volatile content of the magma X_{fg} (wt%) at temperature T is

$$X_{fg} = \frac{X_g\left(T - T_{sol}\right)}{T_{liq} - T_{sol}} \qquad T_{sol} < T < T_{liq} \tag{5.6}$$

where X_g is the weight fraction of fluid of the magma at T_{int}.

The fluid production rate J_g (kg m^{-3} s^{-1}) at the depth z is written by

$$J_g = -\frac{X_{fg}\,\rho_m}{T_{liq} - T_{sol}}\left(\frac{\partial T}{\partial t}\right)_z \qquad z'' < z < z'''. \tag{5.7}$$

where z''' and z'' are the bottom and top of the magma, respectively.

The flux produced from fluid production can be calculated from an one-dimensional model of the advance of isotherms through a crustal section (Walther and Orville, 1982; Hanson, 1992). The integrated vertical fluid flux u_z (kg m^{-2} s^{-1}) at the depth z is given by

$$u_z = \int_z^{z'} \frac{X_{fw}\rho_m}{T_-T}\left(\frac{\partial T}{\partial t}\right)_z dz - \int_{z''}^{z'''} \frac{X_{fg}\rho_m}{T_-T}\left(\frac{\partial T}{\partial t}\right)_z dz \qquad (5.8)$$

where z' is the depth at the bottom of the region of devolatilization.

Radiogenic heat production, the third term on the right hand side of Eq. (5.1), of elements to decay decreases exponentially with depth according to the relation (Turcotte and Schubert, 1982):

$$A = A_0 e^{-z/} \qquad (5.9)$$

where A_0 and hr are the surface radiogenic heat production and the characteristic length scale, respectively. On the other hand, for the magma, the heat production resulted from the decay of radioactive elements A is represented by that of the magma A_g, that is, $A = A_g$.

The initial continental geotherm immediately before the intrusion of magma is calculated from (Turcotte and Schubert, 1982):

$$T_i = T_s + \frac{q_m z}{K} + \frac{A_0 hr^2}{K}\left(1 - e^{-z/}\right) \qquad (5.10)$$

where T_i, T_s, and q_m are the initial temperature of the rock, the surface temperature, and the mantle heat flux, respectively. In this study, the boundary conditions are constant temperature at $z = 0$ and constant mantle heat flux, q_m, at the bottom of the lithosphere. The thickness of the lithosphere before the intrusion of the Gamano granodiorite is assumed to be 30 km. Due to the P-T conditions of M0 metamorphism, the initial geotherm in the lithosphere is roughly compatible with $ca.$ 30°C km^{-1}, and therefore q_m can be assumed to be 0.08 W m^{-2}. The initial geothermal gradient ($ca.$ 30°C km^{-1}) is comparable with the mean geothermal gradient of an

active continental margin or an island-arc (Sugimura and Uyeda, 1973). Based on the estimated pressures of the sillimanite and garnet zones, the Gamano granodioritw was placed between *ca.* 16 and 19 km in depth and therefore the granodiorite layer was *ca.* 3-km-thick. Therefore, I assumed a 3-km-thick sheet-like intrusion with the granodioritic composition which was instantaneously placed between 16 and 19 km in depth. After the intrusion, the thickness of the lithosphere instantaneously increases 35 km. Figure 5.2 shows initial and boundary conditions for the thermal models for M1.

5.2.2: Results

Figure 5.3 shows the temperature-depth curves with increasing time. Thermal relaxation of the situation shown in Fig. 5.2a is fast; namely after *ca.* 4 Ma temperatures are almost restored to original steady-state ones (Figs. 5.3 and 5.4). Figure 5.4 gives the thermal relaxation at three depth levels (12-, 15-, and 20-km depth) associated with the situation in Fig. 5.2a, and the petrologically estimated peak metamorphic temperatures are also drawn as stippled parts. The 12 km depth point, which is correlated to the cordierite zone, reaches the peak temperature of $\approx$ 485°C at 0.40 Ma for Model 1, and *ca.* 500°C at 0.36 Ma for Model 2 in the system's evolution (Fig. 5.4a). The average rates of temperature increase of the two models are *ca.* 1.9×10^{-4} and 2.6×10^{-4}°C year^{-1}, and the periods of a high-temperature condition (> 450°C) are shorter than 1.0 and 1.6 Ma, respectively. The simulated peak temperatures of the two models are well within the petrologically estimated peak metamorphic temperatures between *ca.* 460 and 590°C. At the 15 km depth point, which is correlated to the sillimanite zone, the peak temperatures reach 669°C at 0.10 Ma for Model 1 and 718°C at 0.08 Ma for Model 2 (Fig. 5.4b). The average rates of temperature increase are *ca.* 1.7×10^{-3} and 2.7×10^{-3}°C year^{-1}, and the periods of a high-temperature condition (> 600°C) are shorter than 0.5 and 0.6 Ma, respectively. The simulated peak temperatures of the two models are well within the petrologically estimated peak metamorphic temperatures between *ca.* 630 and 690°C. At the 20 km depth point, which is correlated to the garnet zone, the peak temperatures reach 716°C at 0.20 Ma for Model 1 and 752°C at 0.16 Ma for Model 2 (Fig. 5.4c). The average rates of temperature increase are *ca.* 1.1×10^{-3} and 1.6×10^{-3}°C year^{-1}, and the periods of a high-

temperature condition (> 700°C) is shorter than 0.3 and 0.6 Ma, respectively. Although the simulated peak temperature of Model 1 is slightly lower than the petrologically estimated peak metamorphic temperatures between *ca.* 730 and 770°C, that of Model 2 is well within the petrologically estimated one. Furthermore, the simulated metamorphic field gradients of both the models are shown in Fig. 5.5 with the petrologically estimated one. The simulated and petrologically estimated metamorphic field gradients are nearly consistent.

5.3: Discussion for the analysis

5.3.1: Evaluation of an instantaneous and single intrusion

I modeled the emplacement of the Gamano granodiorite to be an instantaneous and a single episode. The instantaneous pluton emplacement can be assumed to simplify the models, because theoretical studies suggest that magmas rise quickly relative to their rate of cooling (cf. Spera, 1980; Spence and Turcotte, 1985; Mahon *et al.*, 1988; Rothstein and Hoisch, 1994). Spence and Turcotte (1985) calculated a speed of 10 mm s^{-1} to 100 m s^{-1} (3×10^2 to 3×10^6 km Ma^{-1}) for the propagation of magma along cracks. For example, a magmatic body takes 1.5×10^{-1} Ma for rising 15 km at the speed of 10^2 km Ma^{-1}. Therefore, when magma ascends, negligible change occurs in the thermal profile of the crust. However, this approximation is made for ease of calculation and will only be valid so long as the ascent velocity is greater than 10 km Ma^{-1}, and if ascent velocities are less than this value, more complicated models are required (De Yoreo *et al.*, 1989).

The crustal heating can be prolonged by emplacing the plutons many times (Wells, 1980; Chapman and Furlong, 1992; Rothstein and Hoisch, 1994). However, if the total volume of the magma is a constant, the magnitude of crustal heating is lessened at any position compared to the case of a single intrusion, because the early pulses of temperature increase by magma intrusions have been cooled significantly before the later magma are emplaced (Wells, 1980; Chapman and Furlong, 1992). The results of the models (see Figs. 5.3 and 5.4) demonstrate that the attainment of the petrologically estimated peak temperatures requires the emplacement of the Gamano granodiorite by a single episode or by multiple episodes of a rapid succession (Figs. 5.3 and 5.4).

74

5.3.2: Thermal effects of fluid flow

Metamorphic fluid is approximately three times less dense than rocks, thus released fluid tends to migrate upward into overlying rocks. This fluid flow probably takes place along discrete fractures because the permeabilities of unfractured rocks are insufficient to accommodate the fluid flux (Walther and Orville, 1982). The possibility of multi-pass circulation (convection) of fluid at crustal depths greater than 5 ~ 10 km has been a subject of considerable debate (e.g. Ferry, 1986; Wood and Walther, 1986). However, the thermal effects of fluid convection are beyond the scope of this study, and thus a only one-pass upward fluid flow is considered. Fluids can advect substantial amount of heat, and therefore the infiltrating fluid may significantly affect the thermal structure of the overlying rocks (e.g. Peacock, 1989).

Considering the thermal effects of fluid flow on the basis of the calculated fluid production-rate, I implicitly assume that all the fluid, produced by dehydration reactions and from crystallizing intrusion, migrates upward through the overlying rock pile. Fluid flux out of the 35-km-thick lithosphere is plotted as time in Fig. 5.6. The fluid flux curves represent fluid-production of each depth integrated from 0- to 35-km depth. The fluid flux of the two models gradually decreases with the system's evolution, because the flux will decrease with time as the heating rate (dT / dt) of the lithosphere wanes (Fig. 5.6). The results indicate that the advective heat transfer directly affects the T-t paths in an early stage of the system's evolution. The fluid flux of Model 2 is higher than that of Model 1, because the heating rate of the lithosphere of Model 2 is higher than that of Model 1 (see Figs. 5.3 and 5.4).

For clarifying the effects of the fluid flow on the T-t paths, Fig. 5.7 represents the T-t paths calculated from Model 1 at the 12-km depth for three different cases: 1) conduction is the only mode of heat transfer (Case 1); 2) conduction is the only mode of heat transfer and heat consumption resulted from the endothermic reactions is considered (Case 2); and 3) conduction and fluid advection are the mode of heat transfer (Case 3). The peak temperatures resulted from Cases 2 and 3 show *ca.* 30°C lower than that resulted from Case 1, because the endothermic reactions between 400 and 800 °C consumes heat corresponding to ΔH (see also Peacock, 1989; Okudaira *et al.*, 1994a). This indicates that the consumption of heat by endothermic

reactions significantly affects the thermal evolution. The T-t path of Case 3 is characterized by a more rapid increase and decrease in temperature than that of Case 2. The rapid heating is contributed by the fluid advection. However, the rapid cooling does not directly result from fluid advection but from rapid cooling of the Gamano granodiorite, because the employed metamorphic reaction model is only considered during prograde stage ($+ dT / dt$). In the parts beneath the Gamano granodiorite, the inverted thermal gradients persist for several million years (see Fig. 5.3). During this time period, fluid will migrate from the cooler parts beneath the Gamano granodiorite to the warmer the Gamano granodiorite, thus, upward the fluid flow will result in a more rapid cooling of the Gamano granodiorite. However, when the inverted thermal gradients has been erased, upward-flowing fluids will travel down thermal gradients, thereby warming up the overlying rocks. Consequently, the fluid flow, produced by continuous dehydration reactions and from crystallizing magma, contributes toward a shorter duration of high-temperature condition and a more rapid increase and decrease of metamorphic temperature. However, the thermal effects of fluid flow in the one-dimensional models considered here is oversimplified in comparison with two- or three-dimensional models, because the fluids produced by dehydration reactions and crystallizing intrusion migrate upward only and thus lateral fluid flow is neglected in the one-dimensional models (e.g. Furlong *et al.*, 1991; Hanson, 1992).

5.4: Concluding remarks for the analysis

In this Chapter, I proposed the thermal model for M1 metamorphism, and conducted one-dimensional numerical heat-transfer simulations. The simulated peak temperature of each depth can be nearly correlated with the petrologically estimated ones. Moreover, the simulated metamorphic field gradients are also nearly consistent with the petrologically estimated one. These results suggested that the thermal models are reasonable for M1, and therefore it is suggested that M1 metamorphism is caused by the intrusion of the Gamano granodiorite.

Table 5.1. Parameters used in the numerical models

Parameter	Definition	Units and typical values
A	Heat production rate of radioactive elements	W m^{-3}
A_0	Surface radiogenic heat production rate	2.60×10^{-6} W m^{-3}
A_g	Radiogenic heat production rate of magma	2.64×10^{-6} W m^{-3}
C_f	Specific heat of fluid	3750 J kg^{-1} K^{-1}
C_m	Specific heat of rock	880 J kg^{-1} K^{-1}
C^*	Specific heat during reaction	J kg^{-1} K^{-1}
hr	Characteristic length scale	10 km
ΔH	Enthalpy of reaction	J kg^{-1}
J_g	Fluid production rate of reaction	kg m^{-3} s^{-1}
J_w	Fluid production rate of crystallizing magma	kg m^{-3} s^{-1}
K	Thermal conductivity	2.8 W m^{-1} K^{-1}
κ^*	Thermal diffusivity during reaction	m^2 s^{-1}
q_m	Mantle heat flux	0.08 W m^{-2}
ρ_m	Density of rock	2750 kg m^{-3}
T	Temperature	K
T_i	Initial temperature of rock	K
T_s	Surface temperature	273 K ($\cong 0°$C)
T_{start}	Lower temperature of reaction interval	673 K ($\cong 400°$C)
T_{end}	Upper temperature of reaction interval	1073 K ($\cong 800°$C)
T_{liq}	Liquidus temperature of magma	K
T_{sol}	Solidus temperature of magma	K
T_{int}	Initial intrusion temperature of magma	K
t	Time	s
u_z	Fluid flux	kg m^{-2} s^{-1}
X_g	Weight fraction of fluid of initial magma	0.04
X_w	Weight fraction of fluid of rock at surface	0.05
X_{fg}	Weight fraction of fluid of magma at depth z	
X_{fw}	Weight fraction of fluid of rock at depth z	
z	Depth	m
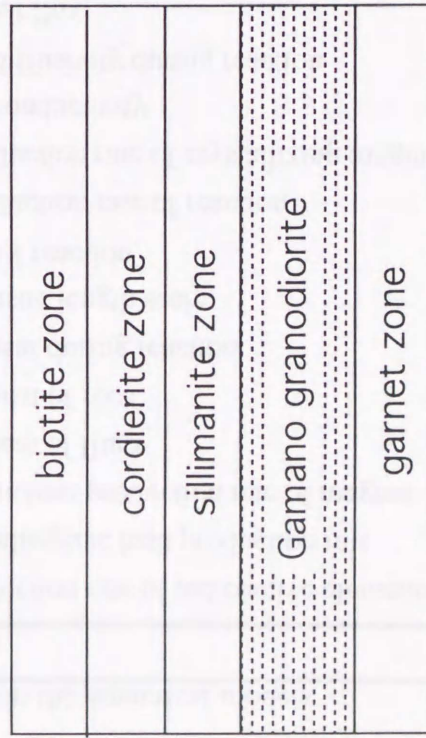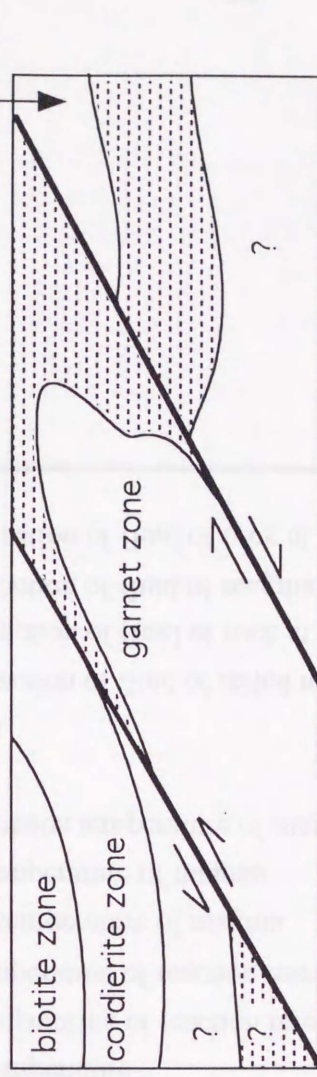
Fig. 5.1. Schematic geological configurations at D1 deformation (a) and D2 deformation (b) after Okudaira et al. (1993, 1994b). See text for further details.
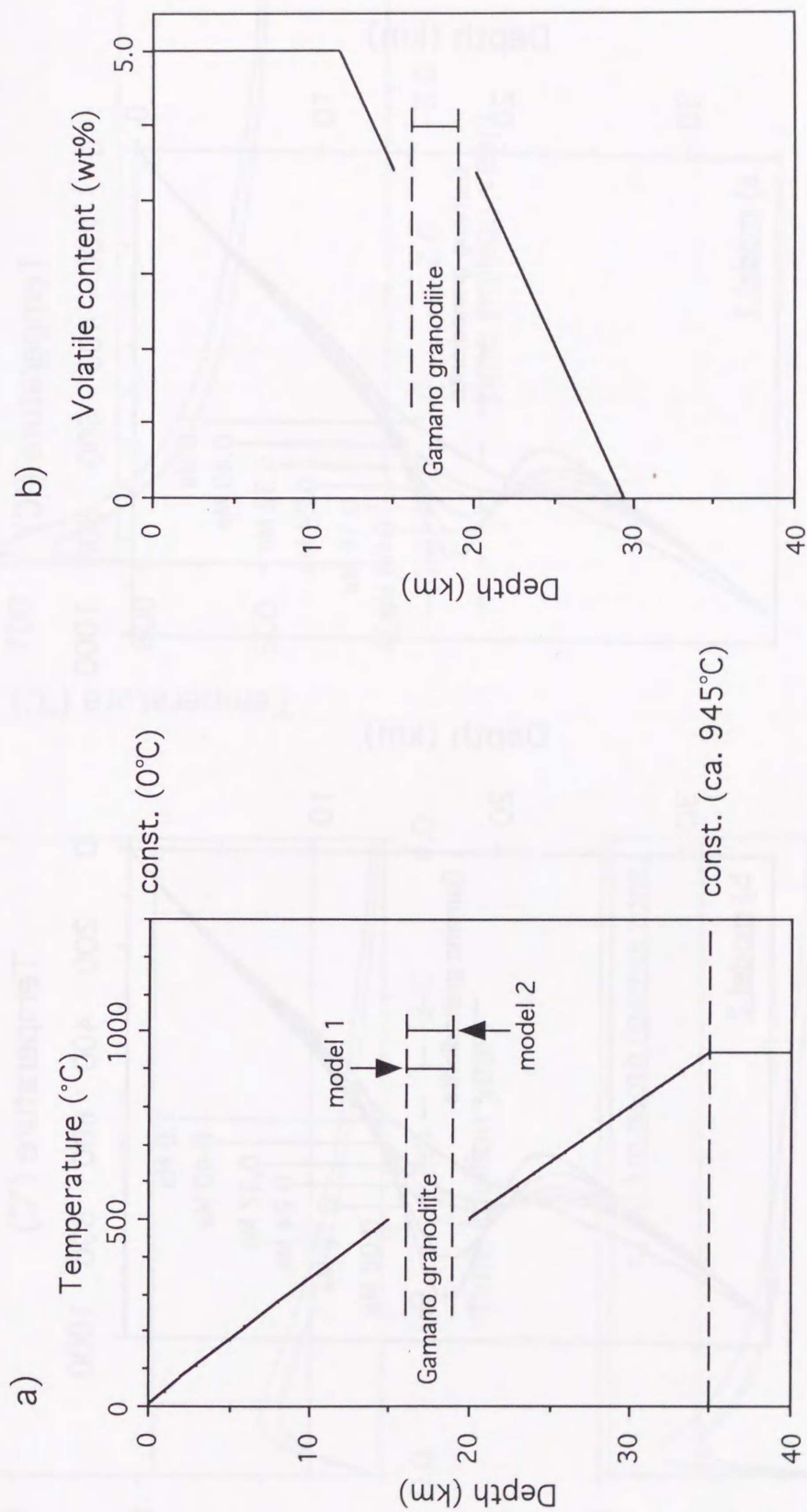
Fig. 5.2. (a) Initial and boundary conditions for both the one-dimensional thermal models for M1. (b) Initial volatile contents as a function of depth. See text for details of tectonic and thermal models.
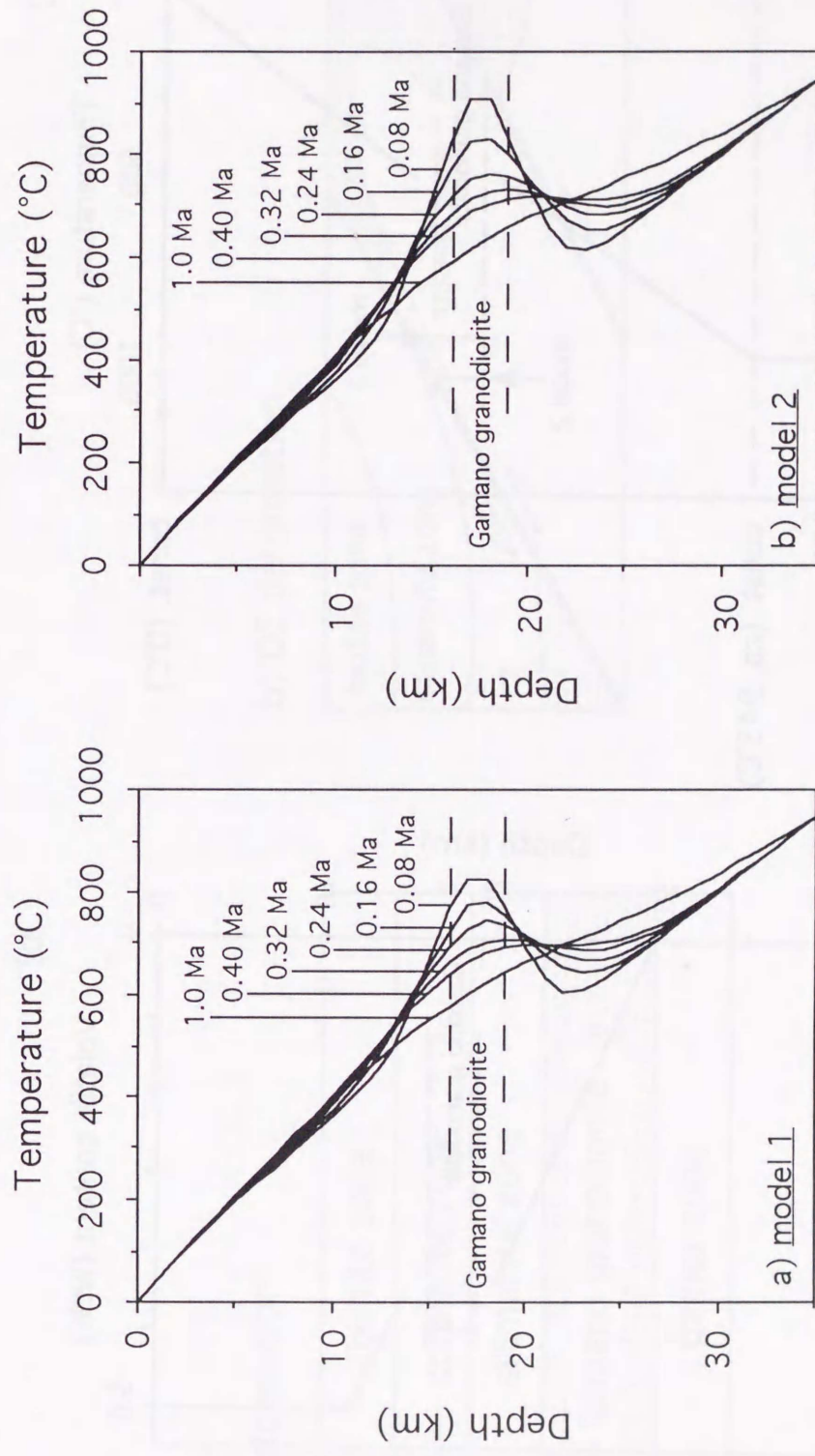
Fig. 5.3. Temperature-depth plots showing thermal evolution of the 35-km-thick lithosphere immediately after instantaneous intrusion of the Gamano granodiorite. Curves labeled with time, in million of years after the intrusion.
(a) Tliq, Tsol, and Tint are 950, 750, and 900°C, respectively (Model 1).
(b) Tliq, Tsol, and Tint are 1050, 850, and 1000°C, respectively (Model 2).
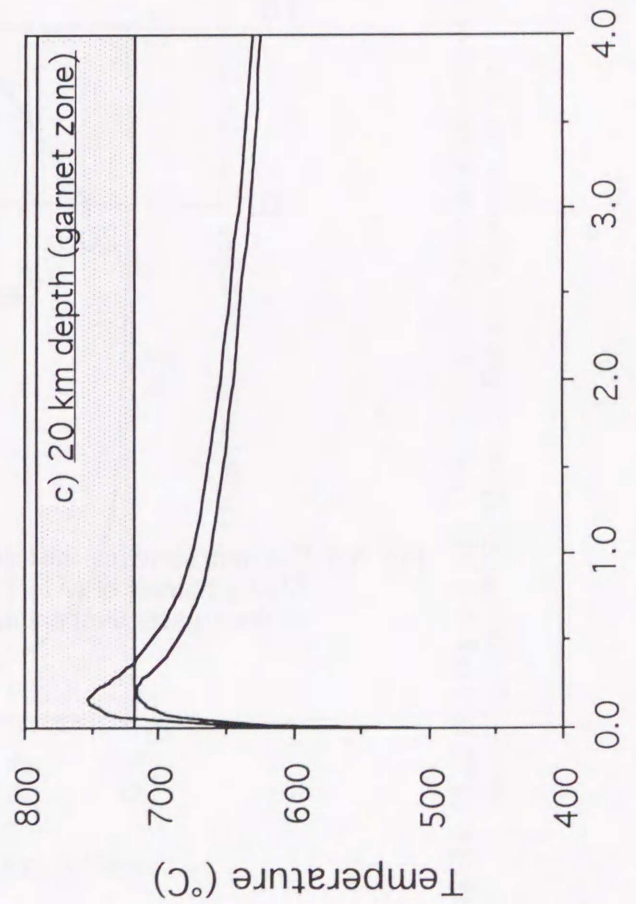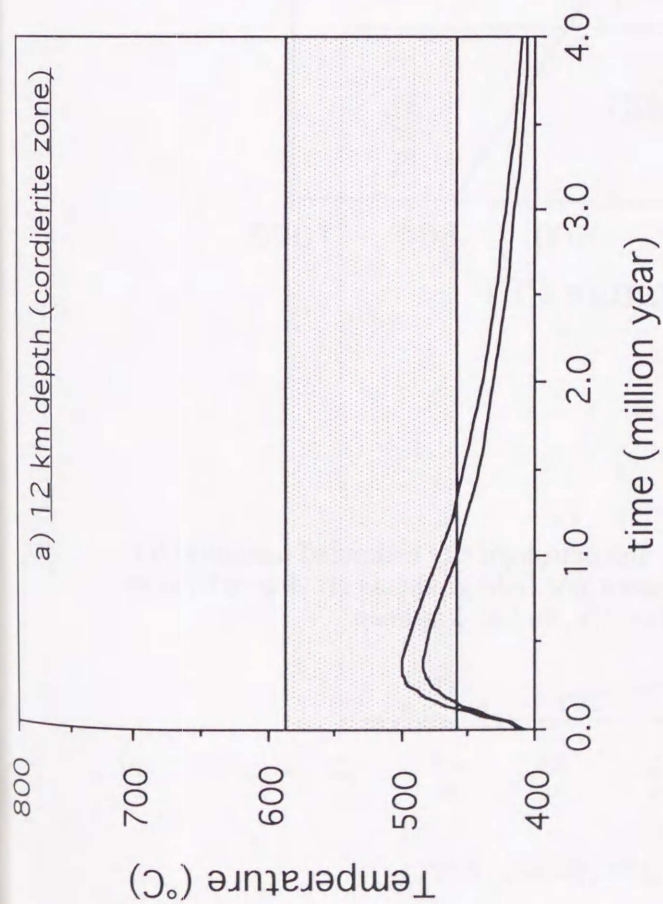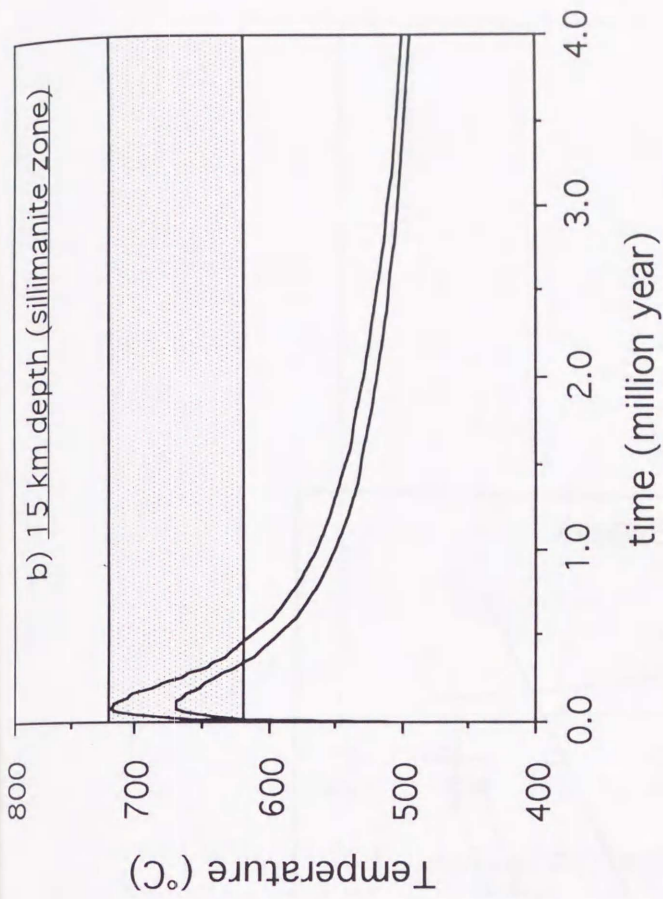
Fig. 5.4. Temperature-time plots of the 12-km-deep (a), 15-km -deep (b), and 20-km-deep (c). Curves shown for different models: Model 1 (upper); Model 2 (lower). Each crustal level corresponds to the depths of the cordierite, sillimanite, and garnet zones, respectively.
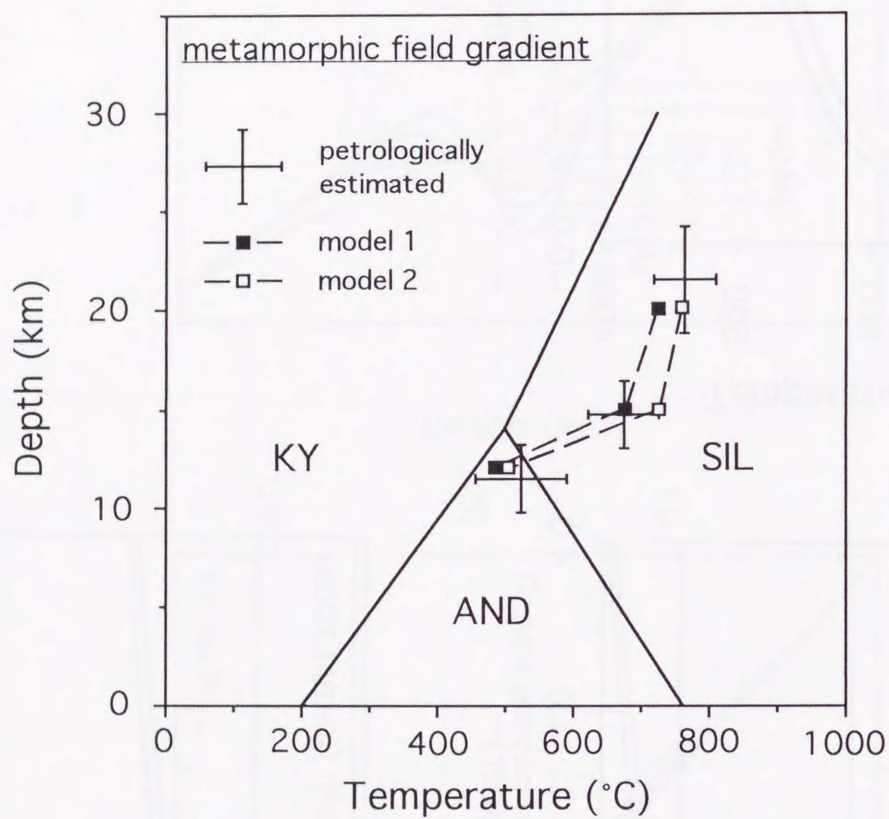
Fig. 5.5. Diagram showing the simulated and petrologically estimated metamorphic filed gradients of M1. The metamorphic field gradients are drawn by trace of the highest temperatures of 12-, 15-, and 20-km-deep.
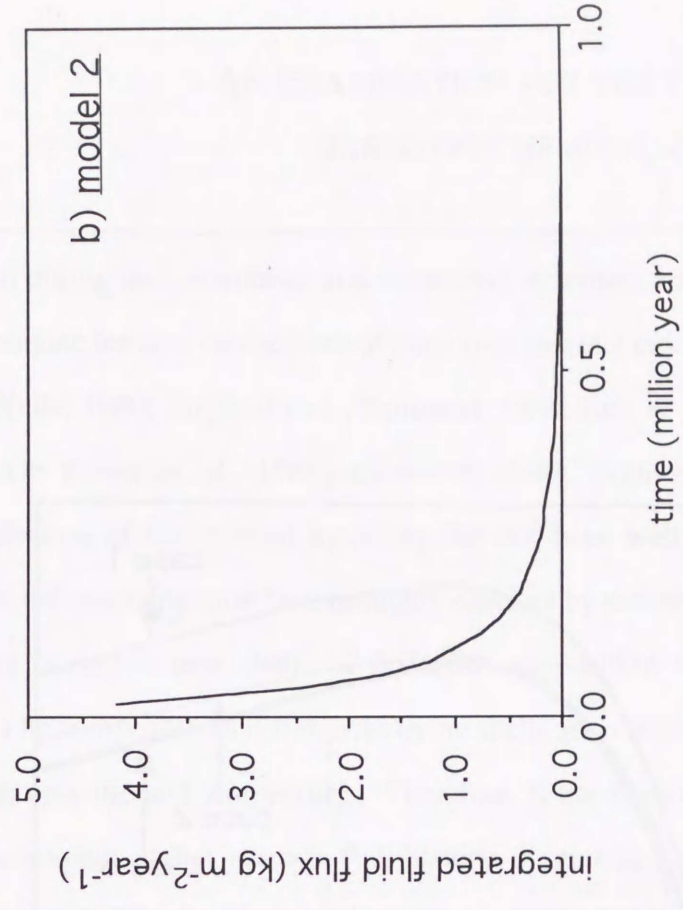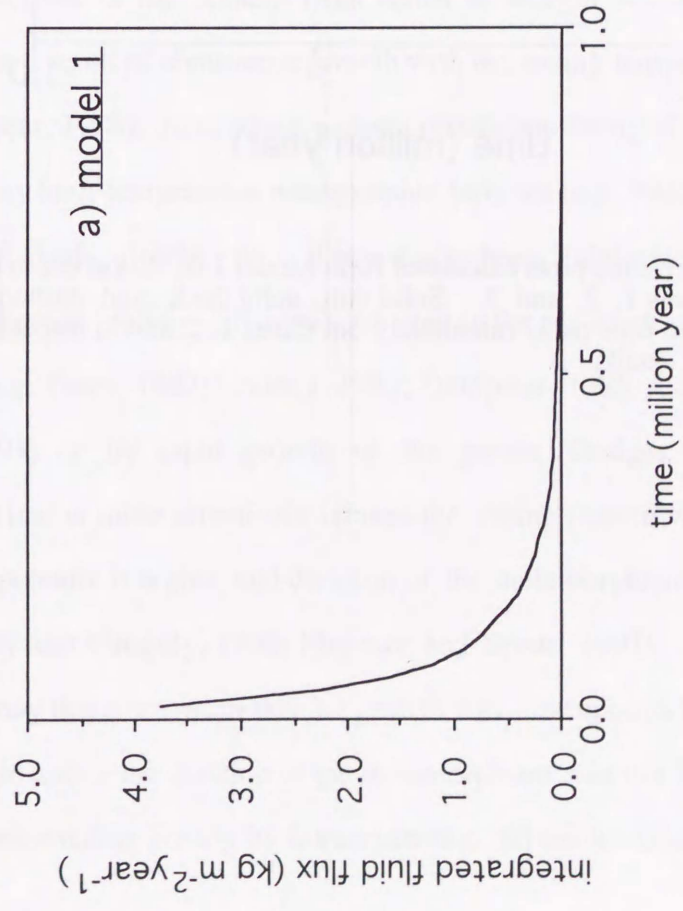
Fig. 5.6. Fluid flux (kg m-2 year-1) through 35 km depth as a function of time. The fluid-flux curves represent fluid production curves integrated from 0- to 35-km depth. (a) Model 1. (b) Model 2. See text for further details.
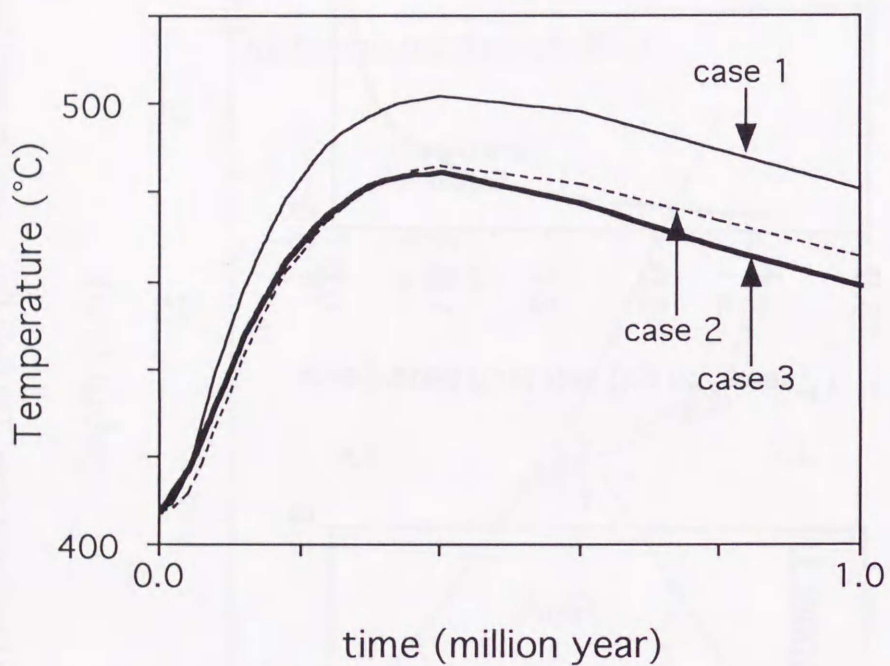
Fig. 5.7. Temperature-time plots calculated form Model 1 of 12-km depth for comparison among Cases 1, 2, and 3. Solid thin, solid thick, and dashed lines are the temperature-time paths calculated from Cases 1, 2, and 3, respectively. See text for further details.

Thermal evolution during metamorphism and associated tectonism have been interpreted in a number of metamorphic terranes on the basis of numerical thermal modeling (e.g. Oxburgh and Turcotte, 1971; Wells, 1980; England and Thompson, 1984; Lux *et al.*, 1986; Wickham and Oxburgh, 1987; De Yoreo *et al.*, 1989; Loosveld, 1989; Rothstein and Hoisch, 1994). However, an evaluation of the thermal modeling has not been well documented, while the validity of the thermal modeling must be thoroughly checked by petrological studies.

Growth zoning occurs as new shells of different composition which are added onto a growing crystal. The compositional differences in the shells arise because of changing external conditions such as pressure and temperature. Therefore, it has been considered that chemical zoning in a metamorphic garnet records P-T history of metamorphism (e.g. Loomis and Nimick, 1982; Spear, 1989a, b; Florence and Spear, 1991, 1993). The zoning in garnet, consisting of a decrease of Mn content from center to margin, so-called normal zoning, has been interpreted as a result of continuous growth with increasing temperature (e.g. Loomis and Nimick, 1982; Spear, 1988). In contrast, garnet crystals consisting of unzoned core have been reported from many high-temperature metamorphic terranes (e.g. Yardley, 1977; Tracy, 1982; Dempster, 1985; Ikeda, 1993a, b). They have been interpreted to have formed by intracrystalline diffusion (volume diffusion) obliterating the pre-existing chemical zoning during metamorphism (e.g. Tracy, 1982; Loomis, 1983; Dempster, 1985; Chakraborty and Ganguly, 1990; Spear, 1991) or by rapid growth of the garnet (Hodges and Silverberg, 1988). Intracrystalline diffusion more effectively relaxes the zoning pattern when a crystal is smaller, metamorphic temperature is higher, and duration of the metamorphism is longer (e.g. Loomis, 1983; Chakraborty and Ganguly, 1990; Florence and Spear, 1991). Preservation of normal zoning in garnet may therefore mean that the growth was slow enough for the zoning to appear, and the temperature and/or the duration of the metamorphism was not high and/or long enough to obliterate the pre-existing zoning by intracrystalline diffusion. Thus, when nucleation and

85

growth mechanisms of garnet crystals are identified, the chemical zoning in garnet can be used to examine the pressure-temperature-time path (*P-T-t* path) of metamorphism (Spear, 1989a, b; Chakraborty and Ganguly, 1990; Florence and Spear, 1991, 1993).

In this Chapter, I present chemical zoning profile in garnets from the Ryoke metamorphic rocks in the Yanai district, southwest Japan, and compare them with numerically simulated zoning pattern of garnets. Then, the temperature-time path (*T-t* path) of the low-pressure facies series Ryoke metamorphism proposed by Chapter V will be examined.

6.1: Experimental procedure

Garnet crystals were separated following the methods of Kretz (1973) and Banno *et al.* (1986) from a small volume (about 4 cm^3) of the metapelite from the sillimanite zone (Fig. 2.1b). The rock was heated in air to 700°C for 60 min. and quenched in water, and pressed by use of a vise. Garnet crystals were separated from other minerals using tweezers. Approximately 80 ~ 90 % of the garnet crystals could be extracted without breaking them. Euhedral crystals were mounted in resin, and the mount was ground down and polished until the crystal diameter under the polarization microscope was equal to that under the reflecting microscope.

Separated garnets were analyzed using an electron-probe microanalyzer (JEOL, JCMA-733II) at Hiroshima University, operating at an accelerating voltage of 15 kV, a current of 19 nA, and a beam width of 5 μm.

6.2: Chemical zoning in garnet

The studied metapelite of the sillimanite zone (Fig. 2.1b) is composed of alternating thin (a few millimeters thick) layers of mica-rich and mica-poor layers. Quartz, plagioclase, K-feldspar, biotite, sillimanite, garnet, and cordierite are stable in the zone, while cordierite rarely occurs and does not coexist with garnet. Graphite, ilmenite, apatite, zircon, and tourmaline occur as accessory minerals. A typical mineral assemblage in the zone is shown on Thompson's (1957) A'FM diagram in Fig. 6.1.

Garnets in the metapelite show euhedral (or subhedral) shape (Fig. 6.2a,d), although some large crystals show anhedral shape where they grew together (Fig. 6.2b,c). The garnets

smaller than *ca.* 0.5 mm in radius are distributed within the mica-poor layers, while the garnets larger than *ca.* 0.5 mm in radius concentrate within the mica-rich layers. The number of the garnets distributed within the mica-rich layers is quite small. Almost all the garnets of various sizes show the textural zoning which consists of inclusion-rich core and inclusion-poor rim (Fig. 6.2). The inclusions, which are mostly anhedral quartz and a very small amount of graphite, ilmenite, and biotite, show no distinct alignment and do not seem to have been subjected to any rotation, which indicates static crystallization of the garnets (e.g. Spry, 1969; Barker, 1990). The shape of the boundary between the inclusion-rich core and inclusion-poor rim is often parallel to the shape of the garnet crystal (Fig. 6.2c). There is no relationship between the boundary of textural zoning and the boundary of chemical zoning.

Some chemical compositions of garnets are presented in Table 6.1. The chemical zoning profiles of molar fractions of almandine (X_{Fe}), spessartine (X_{Mn}), pyrope (X_{Mg}), and grossular (X_{Ca}) in garnets with different radii between 0.1 and 0.8 mm at *ca.* 0.1 mm interval are shown in Fig. 6.3. These profiles were measured from the geometrical center to the outermost margin in the garnets separated from the metapelite unit. In this study, it is regarded that garnet lacks chemical zoning when variation in spessartine content is less than 1 mol% within a single grain except for reversely zoned part.

Giving full attention to the profiles of spessartine (X_{Mn}), important features in Fig. 6.3 are as follows.

1) Three kinds of garnets with normally zoned, unzoned, and reversely zoned patterns in their core occur together in the metapelitic unit.

2) Sample A (radius: $r = 0.10$ mm) is reversely zoned from the center to outermost margin (Fig. 6.3a).

3) Samples B ($r = 0.20$ mm) and C ($r = 0.32$ mm) consist of unzoned core and reversely zoned rim (Fig. 6.3b,c).

4) Samples D ($r = 0.44$ mm), E ($r = 0.50$ mm), F ($r = 0.56$ mm), and G ($r = 0.70$ mm) consist of normally zoned core and reversely zoned rim (Fig. 6.3d ~ g).

5) Sample H ($r = 0.80$ mm) does not show any maximum X_{Mn} at its center (Fig. 6.3h), and rather the grain shows multiple peaks of X_{Mn}, as was reported by Ikeda (1993a, b).

6) The width of the reversely zoned part in garnets with radii smaller than 0.70 mm is approximately 0.1 mm, whereas that of reversely zoned parts in grains of 0.70 and 0.80 mm in radius is *ca.* 0.2 mm.

The molar fraction of spessartine (X_{Mn}) at the center of garnets (solid squares in Fig. 6.4) continuously increases with an increase in radius, except for the larger ($r >$ *ca.* 0.5 mm) garnets in which the X_{Mn} varies greatly. Since the X_{Mn} in the larger ($r > 0.5$ mm) garnets is not so uniform among the garnets, the zoning profiles for the larger garnets as shown in Fig. 6.3f,g,h are not representative ones for their grain sizes. In contrast to the center of the garnets, X_{Mn} at the outermost margin of garnets (open squares in Fig. 6.4) does not depend on its grain size, which is uniform ranging between *ca.* 0.18 and 0.22 (mean value is *ca.* 0.2).

6.3: Nucleation and growth mechanisms of garnet

Nucleation and growth mechanisms of crystals are reflected in textural features, such as spatial and size distributions, of the crystals, which are recorded in the rock at the end of the crystallization episode (e.g. Kerrick *et al.*, 1991).

The crystal size distribution (CSD) plot (Cashman and Ferry, 1988) for garnets in the metapelite is shown in Fig. 6.5. This plot was made by the following procedures. By using an optical microscope with a micrometer, I measured the size of all the garnets ($n = 504$) in two thin sections (total measured area is 14 cm^2) from the same metapelite for which the chemical zoning in garnets is also studied. Following Cashman and Ferry (1988) and Morishita (1992), the number of garnets per size class and per unit area (N_a) is expressed by $N_a = c / (a\,\Delta L)$, where c, a, and ΔL are the number of garnet within the size class, measured area, and size class (0.06 mm in this study), respectively. Furthermore, the number of garnets per size class and per unit volume (N_v) is represented by $N_v = (c / a)^{1.5} / \Delta L$ (Cashman and Ferry, 1988; Morishita, 1992). In Fig. 6.5, the CSD plot shows that crystals of the intermediate size classes, from 0.12 to 0.48 mm (solid circles), fit a line with a slope of 5.68×10^{-3} cm (solid line). The linear crystal size distribution suggests that the crystals belonging to the size classes continuously nucleated and grew (Cashman and Ferry, 1988; Carlson, 1989; Kerrick *et al.*, 1991). In addition, the continuous increase of X_{Mn} at the center of the garnet with radius

between *ca.* 0.1 and 0.5 mm in Fig. 6.4 also indicates that garnets continuously nucleated and grew during prograde metamorphism, because X_{Mn} at the center of garnets reflects the P-T conditions at the time of nucleation (e.g. Loomis and Nimick, 1982; Spear, 1989a, b; Carlson, 1989, 1991). In other words, it is unlikely that the garnets of the intermediate size classes discontinuously grew during multiple crystallization events.

The fact that population densities of the larger and smallest size classes deviate from the slope in Fig. 6.5 could indicate that growth of the garnet for these size classes is not governed by the same nucleation and growth mechanisms (or rates) for the crystals of the intermediate size classes (Cashman and Ferry, 1988; Kerrick *et al.*, 1991). The population densities of the larger size classes deviated from the slope in Fig. 6.5 may have resulted from different nucleation densities and growth rates from those for the garnets of the intermediate size classes. This could be inferred from the fact that the nucleation density of the garnets ($r \leq ca.$ 0.5 mm) distributed within the mica-poor layers is much higher than that of the garnets ($r > ca.$ 0.5 mm) distributed within the mica-rich layers. The difference in nucleation density could lead the difference in growth rate (e.g. Carlson, 1989, 1991). A presence of multiple peak of X_{Mn} (Fig. 6.3h) and of plural inclusion-rich cores (Fig. 6.2b,c) in some larger grains ($r > ca.$ 0.5 mm) suggests that some larger grains may have resulted from impingement of more than two crystals followed by overgrowth (Toriumi, 1986; Ikeda, 1993a). In contrast, a decrease in the number of the garnets of the smallest size class may be interpreted as a result of suppression of nucleation in diffusion domains during diffusion-influenced nucleation and diffusion-controlled growth (Carlson, 1989, 1991), or a consumption of them due to Ostwald ripening after crystal growth with constant rate (Cashman and Ferry, 1988). However, even if the decrease in the number of the garnet of the smallest size class resulted from the Ostwald ripening, the effects of later modification may have been minor considering a small departure of the population density of the smallest size class from the slope in Fig. 6.5.

In the analyzed metapelite, most of garnet crystals are preferentially distributed within the mica-poor layers and show diffusion haloes (Fig. 6.2). Since the garnets were probably produced by consumption of reactants such as biotite, the garnets are preferentially distributed within the mica-poor layers. Furthermore, the diffusion haloes (depletion haloes) formed there,

because later nucleation was probably suppressed in the vicinity of earlier-formed nuclei, which support the diffusion-controlled growth of the garnets (Fisher, 1978; Ridley and Thompson, 1986; Carlson, 1989, 1991). Therefore, such the spatial distribution of the garnets suggests that the crystal growth mechanism is a diffusion-controlled.

In summary, the observations suggest that the garnets of intermediate sizes (*ca.* $0.1 \leq r \leq ca.$ 0.5 mm) have been formed by continuous nucleation and diffusion-controlled growth; whereas, the smaller (< *ca.* 0.1 mm) and larger (> *ca.* 0.5 mm) crystals whose population densities deviated from the slope in Fig. 6.5 would have crystallized by different mechanisms (or rates) as mentioned above. For simplicity, the following analyses are concerned only with the crystals of the intermediate size classes ($0.1 \leq r \leq ca.$ 0.5 mm).

6.4: Numerical analysis

Through numerical analysis, chemical zonings in garnets with different radii during the evolution of M1 metamorphism will be simulated along the *T-t* path proposed by Okudaira *et al.* (1994) (Fig. 5.4b). The simulated and observed zoning patterns in garnets with different radii from the sillimanite zone will be compared in order to evaluate the proposed *T-t* path for M1.

6.4.1: Analytical model

Growth zoning in regionally metamorphosed garnets is produced by continuous net transfer and exchange reactions driven by changes in *P-T* conditions (e.g. Loomis and Nimick, 1982; Spear, 1988). If a rate of prograde reactions is assumed to be sufficiently rapid comparable with a rate of change in *P-T*, local equilibrium between surface of the garnet crystal and matrix of rocks is assumed to be maintained throughout metamorphism (Walther and Wood, 1984; Spear, 1988), i.e., components move freely across grain boundaries between garnet and matrix. As mentioned above, the textural observations suggest that the garnets of the intermediate sizes (*ca.* $0.1 \leq r \leq ca.$ 0.5 mm) have been formed by diffusion-controlled growth. Therefore, the rate of prograde reactions is much faster than that of intergranular diffusion, because growth rate of metamorphic minerals is controlled by the slowest rate-limiting process

(Fisher, 1978). Consequently, in the case of diffusion-controlled growth, it is considered that the rate of intergranular diffusion would be slower than that of prograde metamorphic reactions, although it is rapid enough to justify the boundary conditions on the surface of garnet.

Garnet crystals are grown by the net transfer reactions only during the prograde stage, but are never consumed by the retrograde net transfer reactions unless an exotic fluid infiltrates the rock. In contrast, the cation exchange reactions on the surface of garnets occur during the prograde and retrograde stages, and the exchange reactions occur until the metamorphic temperature decreases below the closure temperature for cation exchange (Spear, 1989b; Yardley, 1989). Retrograde resorption caused by hydration reactions has been interpreted to explain the reverse zoning in garnet (e.g. Tracy, 1982). However, because the garnet crystals separated from the metapelite unit show euhedral shape, and the decrease in the number of the garnets of the smallest size class is small (see Fig. 6.5), these observations suggest that the retrograde resorption of the garnet was minor.

Basic assumptions employed in the analysis are summarized as follows: 1) the garnets statically formed during M1 metamorphism only, 2) nucleation and growth occur only during prograde metamorphic stage, 3) maximum radius of grain crystallized by continuous nucleation and growth is 0.5 mm, 4) growth of the garnets is governed by diffusion-controlled growth law, 5) intracrystalline diffusion in the garnet occurs during and after the crystallization, 6) after the thermal peak, grain size of the garnets does not change, 7) the crystal is in equilibrium with other phases on its surface and composition of the surface is a function of temperature until the metamorphic temperature decreases below the closure temperature for cation exchange, 8) after the metamorphic temperature decreases below the closure temperature, intracrystalline diffusion in garnet occurs being constrained by mass balance within the garnet, and 9) the shape of garnet crystals is assumed to be as an isotropic sphere to simplify the following analysis. In this study, an explicit finite-difference method with a 1×10^{-5} m array spacing and a 3.15×10^7 sec time step was used for the numerical simulation.

6.4.2: Composition of garnet surface

If tschermak's exchange is ignored in the coexisting minerals, there are only four independent continuous reactions which may operate in the assemblage quartz + plagioclase + K-feldspar + biotite + sillimanite + garnet in the SiO_2-Al_2O_3-FeO-MgO-MnO-CaO-Na_2O-K_2O-H_2O (MnNCKFMASH) system (Spear, 1989a, b):

$FeMg_{-1}$ (garnet) = $FeMg_{-1}$ (biotite) $\hspace{2cm}$ (6.1)

$FeMn_{-1}$ (garnet) = $FeMn_{-1}$ (biotite) $\hspace{2cm}$ (6.2)

$Ca_3Al_2Si_3O_{12}$ + $2Al_2SiO_5$ + SiO_2 = $3CaAl_2Si_2O_8$ $\hspace{1cm}$ (6.3)
$\hspace{0.5cm}$ (grossular) $\hspace{0.4cm}$ (sillimanite) $\hspace{0.2cm}$ (quartz) $\hspace{0.5cm}$ (anorthite)

$KFe_3AlSi_3O_{12}(OH)_2$ + Al_2SiO_5 + $2SiO_2$ =
$\hspace{0.5cm}$ (annite) $\hspace{2.2cm}$ (sillimanite) $\hspace{0.2cm}$ (quartz)

$Fe_3Al_2Si_3O_{12}$ + $KAlSi_3O_8$ + H_2O. $\hspace{2.5cm}$ (6.4)
$\hspace{0.5cm}$ (almandine) $\hspace{0.8cm}$ (K-feldspar)
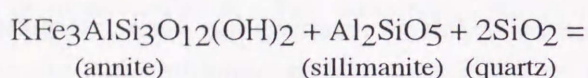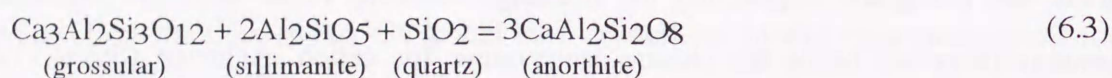
In general, manganese component is more concentrated in garnet than in most coexisting phases with the ratio Mn / (Mn + Fe) decreasing in the order garnet > ilmenite >> cordierite > biotite (e.g. Pownceby *et al.* 1987). Garnet may stably coexist with ilmenite ($FeTiO_3$) which commonly forms a solid solution with pyrophanite ($MnTiO_3$). This suggests the possibility of the Fe-Mn partitioning between garnet and ilmenite as the following exchange reaction;

$Fe_3Al_2Si_3O_{12}$ + $3MnTiO_3$ = $Mn_3Al_2Si_3O_{12}$ + $3FeTiO_3$, $\hspace{1cm}$ (6.5)
$\hspace{0.5cm}$ (almandine) $\hspace{0.7cm}$ (pyrophanite) $\hspace{0.7cm}$ (spessartine) $\hspace{0.7cm}$ (ilmenite)
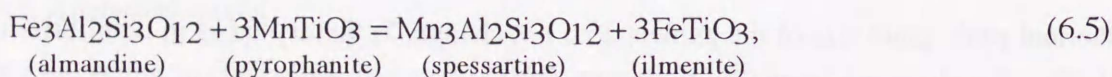
and this partitioning strongly depends on temperature (Pownceby *et al.*, 1987).

From Spear (1988), a difference in the composition (ΔX_{Mn}) of garnet grown by continuous reactions (Eqs 6.1 ~ 6.5) may be computed for a difference in temperature (ΔT) and pressure (ΔP) by relation as

$$\Delta X_{Mn} = \left(\partial X_{Mn} / \partial T \right)_P \Delta T + \left(\partial X_{Mn} / \partial P \right)_T \Delta P. \hspace{1.5cm} (6.6)$$

Because changes in spessartine component little reflect changes in pressure (Spear, 1989b) and the garnets analyzed here assumed to be crystallized in a static condition, the second term on the right-hand side of Eq (6.6) can be neglected. Therefore, the composition of the surface of the garnet is expected to be only a function of temperature, and the above equation can be rewritten for a certain finite temperature interval as

$$X_{Mn} = (dX_{Mn} / dT)T + C, \tag{6.7}$$

where T and C are temperature (K) and constant, respectively. (dX_{Mn} / dT) and C are assumed to be -1.0×10^{-3} and 1.095, respectively, to fit the highest and lowest values of X_{Mn} simulated for 0.5 mm garnet after 2 Ma system's evolution to those of the observed one. These values correspond with those calculated for the metamorphic temperatures where the assemblage garnet + biotite + sillimanite + K-feldspar + quartz + plagioclase is stable, which occurred in Fall Mountain, New Hampshire, based on the Gibbs method (Spear, 1989a).

6.4.3: Diffusion-controlled growth

A rate of growth controlled by intergranular diffusion exhibits an exponential dependence upon temperature (Ridley and Thompson, 1986; Carlson, 1989; Kerrick et al., 1991). When the ith crystal nucleates at time t_i, its radius r as a function of time t is given by the following general form of the diffusion-controlled growth law (Christian, 1975; Carlson, 1989):

$$r_i(t) = k_1 \sqrt{D_e(t - t_i)} \tag{6.8}$$

where D_e and k_1 are an effective diffusion coefficient for intergranular diffusion and a dimensionless constant, respectively. According to Carlson (1989), the effective diffusion coefficient D_e at T for intergranular diffusion is written as Arrhenius type equation:

$$D_e = D_\infty \exp\left(\frac{-E_a}{RT}\right) \tag{6.9}$$

where D_∞ is the value of the diffusion coefficient at infinite T, which is assumed to be constant, and E_a, R, and T are the activation energy for intergranular diffusion, gas constant, and temperature (K), respectively. Substituting (6.9) into (6.8) gives

$$r_i(t) = k_2 \sqrt{(t - t_i) \exp\left(\frac{-E_a}{RT}\right)} \qquad (6.10)$$

where growth constant k_2 is $k_1 \sqrt{D_\infty}$, and E_a is taken to be 8.37 x 10^4 J mol^{-1} (Fisher, 1978). The growth constant k_2 has not previously been estimated by experimental studies. Here, the value of k_2 is assumed by using the following method, which is similar to those adopted by Kretz (1974) and Carlson (1989). In the above mentioned mineral assemblage, garnet can be grown by the reaction biotite + sillimanite + quartz = garnet + K-feldspar + H_2O, from the temperature above the breakdown of muscovite + quartz (Spear, 1989a). Provided that the largest grain size attainable by diffusion-controlled growth is 0.5 mm in radius during the temperature increase from the temperature above the breakdown of muscovite + quartz (600°C) to the highest temperature (670°C), the growth constant k_2 is obtained as 6.29 x 10^{-8} m s$^{-0.5}$. The value of the growth constant is fixed for the other garnets with different radii. Figure 6.6b shows the radius versus time curves nucleated at different times during the prograde T-t path (Fig. 6.6a). The average growth rate ranges from 5.1 x 10^{-6} to 2.9 x 10^{-5} mm year^{-1}. The growth rate is comparable with the estimated one (1.3 x 10^{-6} ~ 1.9 x 10^{-5} mm year^{-1}) based on dating of a zoned garnet from Pigeon Island, Newfoundland, which probably crystallized by diffusion-controlled growth (Vance and O'Nions, 1990).

6.4.4: Intracrystalline diffusion

For intracrystalline diffusion in garnet, it is appropriate to apply the model for diffusion in a sphere (Crank, 1975). A fundamental equation to be solved is:

$$\frac{\partial X}{\partial t} = \frac{1}{x^2} \frac{\partial}{\partial x}\left(D x^2 \frac{\partial X}{\partial x}\right), \qquad (6.11)$$

with boundary conditions as

$$\frac{\partial X}{\partial x} = 0 \text{ at the center of a sphere,}$$

$X = f(T)$ at the outermost margin of a sphere,

where X, t, D, and x represent concentration of the component, time, diffusion coefficient of the component, and distance, respectively.

Garnets can be treated as almandine-spessartine solid solution in the following analyses, because the compositions of garnets show high (Fe + Mn) / (Fe + Mn + Mg + Ca) ratio, 0.86 ~ 0.90 (Table 6.1) and they indicate complementary zoning profiles of spessartine and almandine with relatively small change in pyrope and grossular (Fig. 6.3). Because the growth zoning pattern in garnet shows complementary changes of Fe and Mn, and because the concentration of the Mg and Ca components and their changes are negligibly small, the diffusional relaxation of the pattern can be considered to involve essentially Fe-Mn exchange (Elphick *et al.*, 1985; Loomis *et al.*, 1985; Chakraborty and Ganguly, 1992). Therefore, the diffusion coefficient of a multicomponent system can be treated as that of a binary (Fe-Mn) system in the following analyses.

According to Loomis *et al.* (1985) and Chakraborty and Ganguly (1992), the diffusion coefficient in all ideal binary ionic solution can be written as

$$D = \frac{D_1^* D_2^*}{X_1 D_1^* + X_2 D_2^*}, \tag{6.12}$$

where D_1^* and D_2^* represent tracer diffusion coefficients of the components 1 and 2, respectively, and X_1 and X_2 (= 1 - X_1) are concentration of the components 1 and 2, respectively. In this study, the tracer diffusion coefficients of Fe and Mn are expressed as follows (Chakraborty and Ganguly, 1990, 1992):

$$D^* = (6.4 \times 10^{-4}) \exp(- (65.82 \times 10^3 + 0.14P) / RT) \text{ cm}^2 \text{ s}^{-1}, \tag{6.13a}$$

$$D^*_{Mn} = (5.1 \times 10^{-4}) \exp(- (60.57 \times 10^3 + 0.15P) / RT) \text{ cm}^2 \text{ s}^{-1},$$ (6.13b)

where P is pressure in bar, which is taken to be 4 kbar in this study.

Schematic diagram of the changing chemical zoning during and after growth of the garnet is illustrated in Fig. 6.7. As mentioned above, the garnet is grown by using Eq (6.10) (see also Fig. 6.6b) and composition at the surface of the garnet is calculated by using Eq (6.7). Because the intracrystalline diffusion operates during and after garnet growth, molar fraction of the center of the garnet decreases with system's evolution. Growth of the garnet finishes at 0.1 Ma when the metamorphic temperature is the highest, and the grain size of the garnet after the thermal peak does not change. X_{Mn} of the outermost margin of the garnets calculated by using Eq (6.7) until the metamorphic temperature decreases to 600°C, which is assumed to be the closure temperature for the retrograde exchange reactions. Even after the temperature is decreased below the closure temperature, the intracrystalline diffusion in the garnet occurs until 2 Ma, being constrained by mass balance within the garnet. There is no significant change in X_{Mn} of any crystals after 2 Ma, because the intracrystalline diffusion coefficient is very small below the temperature established at 2 Ma (= 520°C).

6.4.5: Analytical results

Figure 6.8 shows simulated zoning profiles of X_{Mn} of different radii (0.1, 0.2, 0.3, 0.4, and 0.5 mm) at the time when growth is completed (thin solid lines) and those at the time when 2 Ma elapses after the intrusion (thick solid lines). Important results shown in Fig. 6.8 are: 1) the smallest grain (0.1 mm in radius) shows reverse zoning from the center to the outermost margin (Fig. 6.8a); 2) small grains (0.2 ≤ r ≤ 0.4 mm) consist of unzoned core and reversely zoned rim (Fig. 6.8b,c,d), and the variations of X_{Mn} in the unzoned part in the garnets with the radius of 0.2, 0.3, and 0.4 mm are $ca.$ 0.13, 0.36, and 0.69 mol%, respectively; 3) the largest grain (0.5 mm in radius) consists of normally zoned core and reversely zoned rim (Fig. 6.8e), and the difference in X_{Mn} between the highest and lowest across the grain is $ca.$ 5.96 mol%; 4) the width of reversely zoned part of all the crystals with different radii is 0.07 ~ 0.1 mm.

It is clear from the comparison between the zoning profiles at the end of growth and those at 2 Ma that the unzoned core of smaller garnets (Fig. 6.8b,c,d) does not really cause diffusional homogenization, but simply reflects very small reaction progress in the later formed garnets. The preservation of a distinct normal zoning of X_{Mn} in the garnet of 0.5 mm (Fig. 6.8e) results from a relatively large change in temperature during the growth period. The temperature interval (ΔT) during the growth of the 0.5 mm garnet is *ca.* 70°C, although the ΔT during the growth of the garnet smaller than 0.40 mm in radius is smaller than *ca.* 10°C (see Fig. 6.6). These results suggest that the zoning patterns at the core of all the garnets essentially reflect the prograde *T-t* history, although the zoning patterns at the rim of all the garnets and near the center of the largest garnet are significantly modified by the intracrystalline diffusional relaxation because of relatively large difference in X_{Mn} within relatively short distance.

6.5. Discussion for the analysis

Figure 6.9 shows comparison between the chemical zonings of the observed garnets (0.10, 0.20, 0.32, 0.44, and 0.50 mm in radius) in Fig. 6.3 and the patterns simulated at 2 Ma in the system's evolution. This figure indicates that the observed zoning profiles are well reproduced by the numerical model with a difference less than 1 mol%, except for the largest grain. In the middle part of the largest garnet, the values of the simulated X_{Mn} are significantly lower than those of the observed one, and a maximum difference in the values between them is *ca.* 1.7 mol% (Fig. 6.9e). The difference between the observed and simulated zoning patterns in the garnet may have resulted from difference between the actual and proposed *T-t* paths. According to Okudaira *et al.* (1993), there is an uncertainty for the highest metamorphic temperature for rocks in the sillimanite zone, which could have ranged between 630 and 690°C. It is therefore necessary to examine a possible variation of zoning pattern for a range of *T-t* path. To examine the variation of garnet zoning, temperatures of different *T-t* paths are taken to be proportional to those of the previously simulated one (Fig. 6.4b). Hence, temperatures of the different path to be examined here are given by the following equation:

$$T_1 = T_0 + (T_0 - 773)f \tag{6.14}$$

where T_0 and T_1 represent the temperature (K) of the previously estimated path (Fig. 6.4b) and that of modified one, respectively, and f is a scaling factor. Figure 6.10a shows the modified T-t path (thin solid line) between 0 and 2 Ma with f of -0.12, which corresponds to 20°C decrease in the thermal peak from the previously estimated one (thick solid line). Figure 6.10b represents the modified zoning profile of X_{Mn} in the simulated garnet of 0.50 mm in radius (thin solid line) calculated for the modified path. In this calculation, the same assumptions are employed as those of the previous ones, except for the values of k_2 and t_i. As shown in Fig. 6.10b, the observed zoning pattern for the 0.5 mm radius garnet (thin solid line with open squares) falls between the profiles calculated for the modified T-t path and for the previously estimated one. This result indicates that the difference in the peak temperature between the numerically simulated T-t path and the actual T-t path was probably less than 20°C. Furthermore, the maximum difference between the observed and simulated X_{Mn} occurs in the middle part of the garnet, which may suggest that the temperatures of the actual T-t path are lower than those of the proposed one at the early to middle stages (ca. 0.02 ~ 0.06 Ma) of the prograde metamorphism.

As mentioned above, the observed X_{Mn} at the center of garnets for the sizes ranging from ca. 0.1 to 0.4 mm (solid squares in Fig. 6.11) increases slightly with grain size, although the X_{Mn} value of the garnets with similar grain size varies by ca. 1 mol%. In contrast, for the grains with a radius greater than ca. 0.4 mm, the increase of the X_{Mn} values with grain size is abrupt. Such a sharp increase has been reported by Kretz (1973) from garnet-biotite-cordierite schist near Yellowknife, Canada. Molar fraction of spessartine at the center of the simulated garnets (solid line in Fig. 6.11) also slightly changes for the sizes between ca. 0.1 and 0.4 mm, and abruptly increases for the sizes greater than ca. 0.4 mm. Overall, the values of X_{Mn} at the center of the simulated garnets are comparable with those of the observed ones, and a difference in the values between them is less than about 1 mol%, which corresponds with a difference in temperature of ca. 10°C calculated by using Eq (6.7). In the garnets smaller than ca. 0.25 mm in radius, the values of X_{Mn} at the center of the simulated garnets are systematically higher than those of the observed ones by about 1 mol%. A possible reason of the difference between the

observed and simulated center X_{Mn} is 1) that the value of dX_{Mn} / dT in Eq (6.7) is underestimated, 2) or that the temperatures of the proposed T-t path are lower than those of the actual path at the late stage of the prograde metamorphism. If the latter is the case, the actual metamorphic temperatures may be higher than the proposed ones by *ca.* 10˚C at the late stage (*ca.* 0.08 ~ 0.1 Ma) of the prograde metamorphism.

6.6: Concluding remarks for the analysis

The garnets from the Ryoke metamorphic belt (low P / T type) in the Yanai district, southwest Japan, show various chemical zoning patterns. The zoning pattern at the core of the garnets systematically varies from reversely zoned to unzoned to normally zoned patterns with increasing grain size of the garnets. Quantitative and qualitative textural analyses for the garnets lead to the conclusion that the crystallization mechanism for the garnets ($0.1 \leq r \leq 0.5$ mm) is a continuous nucleation and diffusion-controlled growth. To examine the validity of the T-t path proposed by Okudaira *et al.* (1994), I study whether the chemical zoning pattern for various sizes of the garnets can be reproduced by a numerical simulation for the T-t path. The simulation employs a numerical model of continuous nucleation and diffusion-controlled growth, in combination with intracrystalline diffusion. The results of the simulation for the T-t path indicate that the observed zoning patterns of the various sizes of garnets are well reproduced by the numerical model, in spite of the fact that simulated zoning patterns strongly depend on T-t history, i.e. X_{Mn} changes responding to the subtle changes in temperature. Deduced from the comparison between the observed X_{Mn} and the simulated X_{Mn} for the proposed T-t path, the metamorphic temperatures of the actual T-t path could have been lower than those of the proposed one by *ca.* 20˚C at the early to middle stages, and are higher by *ca.* 10˚C at the late stage of the prograde metamorphism. Thus, if the employed analytical model and the assumed value of the parameters are appropriate, the results of this study suggest that the proposed T-t path gives a good explanation for the low-pressure facies series Ryoke metamorphism.

Table 6.1. Chemical compositions at the geometrical center (left column) and outermost margin (right) column) of garnets in cation per mineral formula (O = 24). Radius (mm) of each sample is in parentheses. R^{2+} : Fe + Mn + Mg + Ca.

sample no.	A (0.10 mm)		B (0.20 mm)		C (0.32 mm)		D (0.44 mm)	
Si	6.03	6.02	6.02	6.06	6.00	5.99	5.97	5.95
Al	4.04	4.04	4.05	4.13	4.04	4.07	4.05	4.05
Fe	4.18	4.19	4.20	3.93	4.17	4.07	4.17	4.20
Mn	0.84	1.11	0.88	1.11	0.95	1.21	1.03	1.15
Mg	0.59	0.46	0.57	0.46	0.56	0.42	0.54	0.47
Ca	0.25	0.22	0.24	0.19	0.26	0.19	0.24	0.21
cation sum	15.93	16.04	15.96	15.88	15.98	15.95	16.00	16.03
(Fe+Mn) / R^{2+}	0.86	0.89	0.86	0.89	0.86	0.90	0.87	0.89

Table 6.1. (*continued*)

sample no.	E (0.50 mm)		F (0.56 mm)		G (0.7 mm)		H (0.8 mm)	
Si	5.98	5.95	6.03	6.07	5.96	5.85	5.93	5.98
Al	4.03	4.09	4.01	4.07	4.07	4.06	4.07	4.16
Fe	3.95	4.12	3.91	3.9	63.83	4.20	4.21	3.95
Mn	1.25	1.16	1.25	1.20	1.35	1.25	1.03	1.24
Mg	0.47	0.47	0.45	0.41	0.42	0.43	0.52	0.40
Ca	0.32	0.21	0.31	0.19	0.38	0.24	0.29	0.22
cation sum	16.00	16.00	15,96	15.90	16.01	16.03	16.05	15.95
(Fe+Mn) / R^{2+}	0.87	0..89	0.87	0.90	0.87	0.89	0.87	0.89
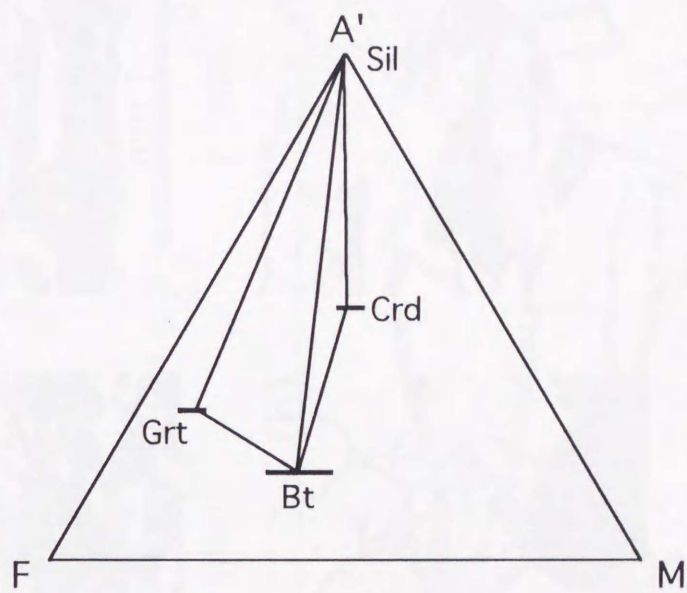
Fig. 6.1. A'FM diagram projected from K-feldspar in the Thompson's AKFM system for the sillimanite zone.
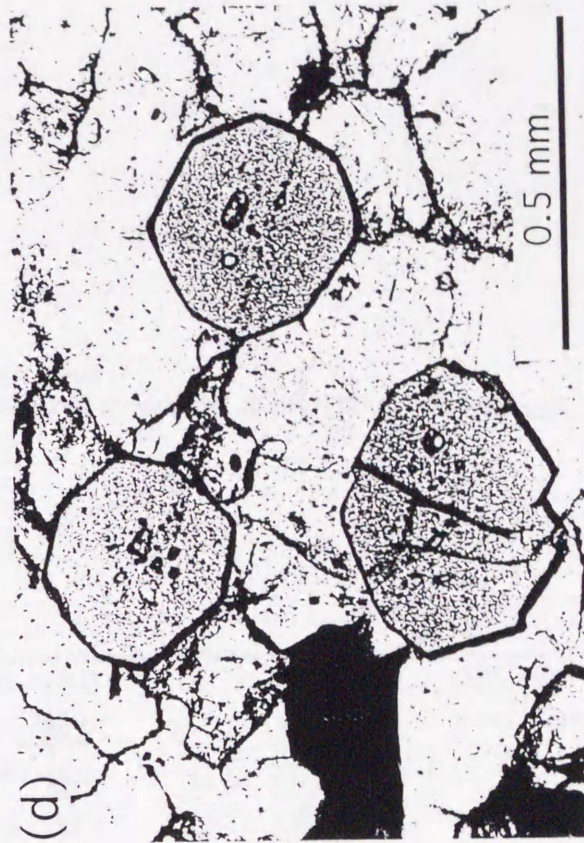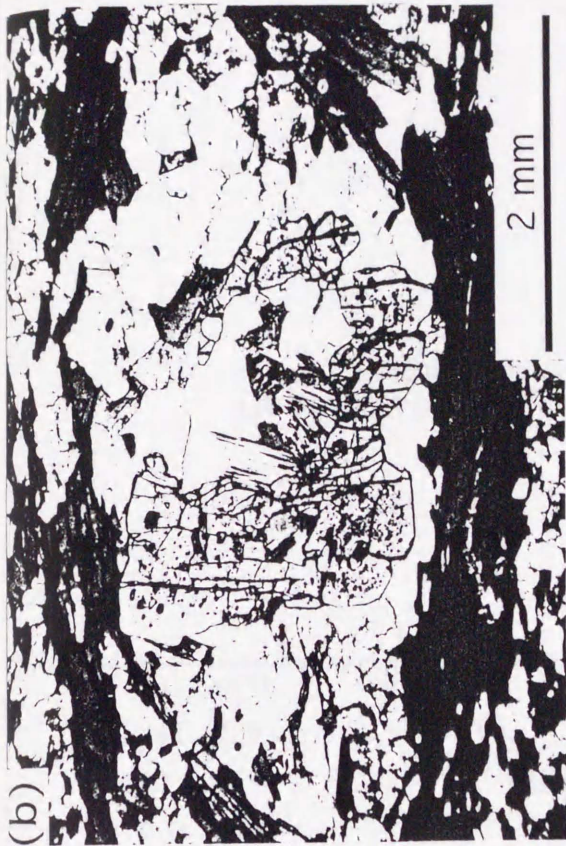
Fig. 6.2. Microphotograph showing textures of garnet crystals in the thin section of the studied metapelite. Minerals showing high refractive index are garnets. Dark-colored and light-colored minerals are biotite and felsic minerals (quartz, plagioclase, and K-feldspar), respectively. Plane-polarized light. (a) Garnet crystals showing euhedral or subhedral shape and preferential distribution within mica-poor layer. (b) and (c) Anhedral garnet crystals showing the texture indicating impingement of more than two crystals. (d) Garnet crystals showing euhedral shape and quartz grains as inclusions in core of garnets.
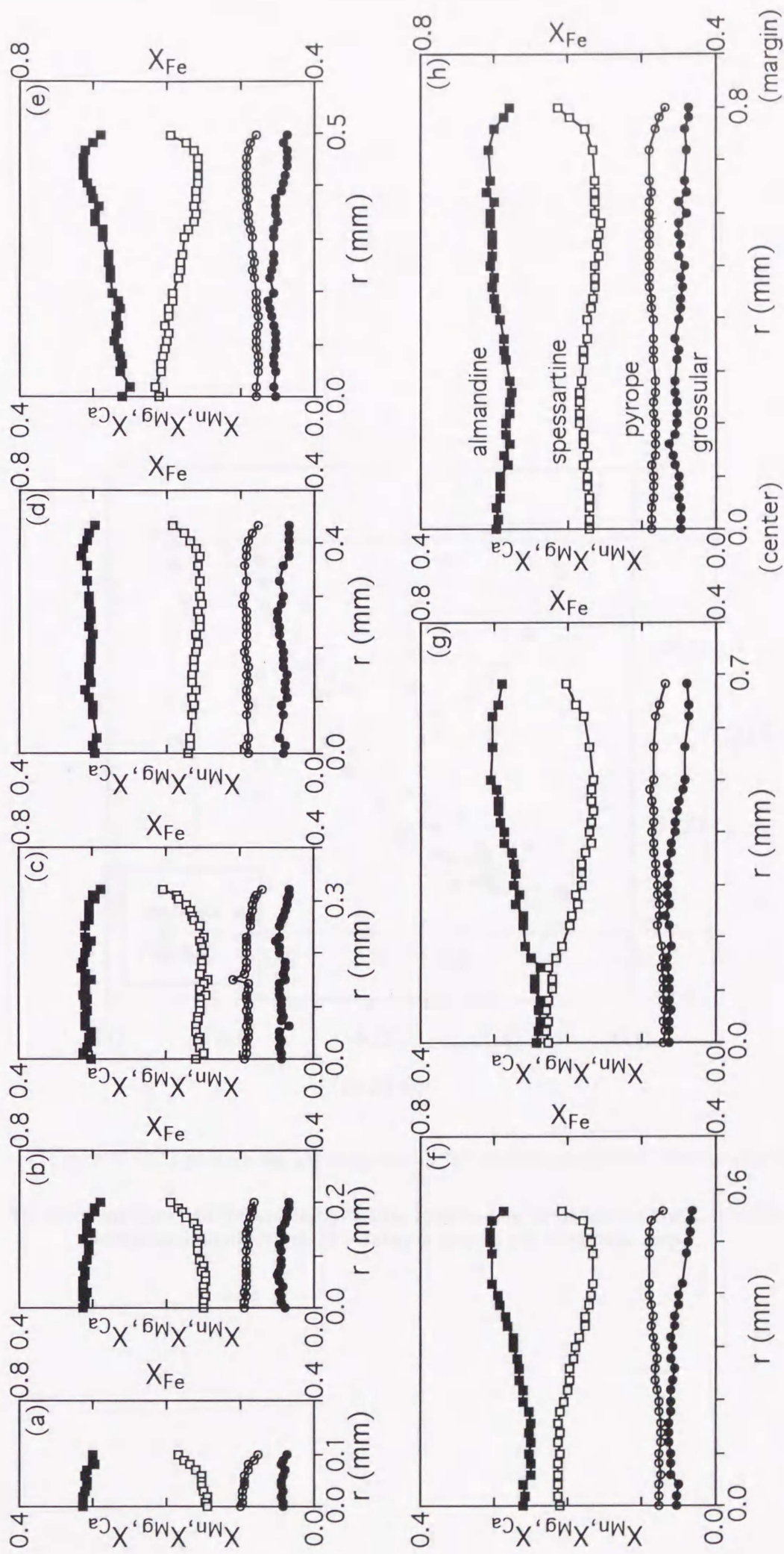
Fig. 6.3. Chemical zoning patterns for almandine (XFe), spessartine (XMn), pyrope (XMg), and grossular (XCa) of the separated garnet crystals of different radii between 0. and 0.8 mm at c. 0.1 mm interval from the studied sample. (a) sample A (r = 0.10 mm). (b) sample B (r = 0.20 mm). (c) sample C (r = 0.32 mm). (d) sample D (r = 0.44 mm). (e) sample E (r = 0.50 mm). (f) sample F (r = 0.56 mm). (g) sample G (r = 0.70 mm). (h) sample H (r = 0.80 mm).
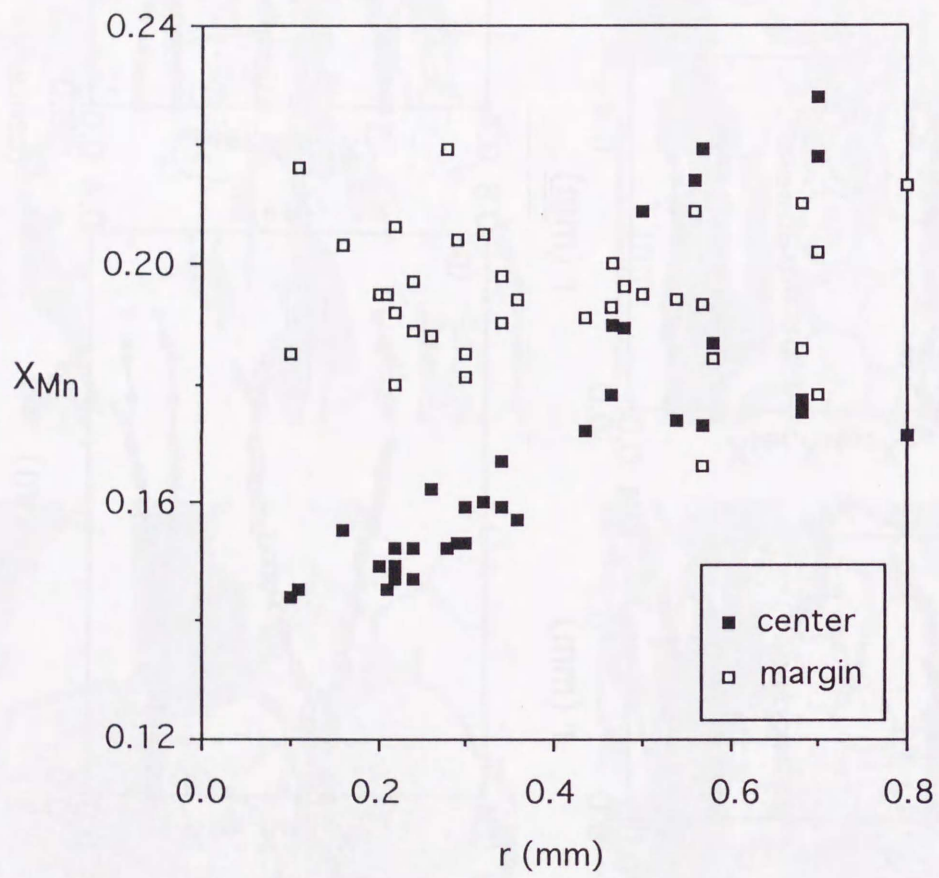
Fig. 6.4. XMn values at the geometrical center (solid square) and outermost margin (open square) of the garnets separated from the studied metapelite.
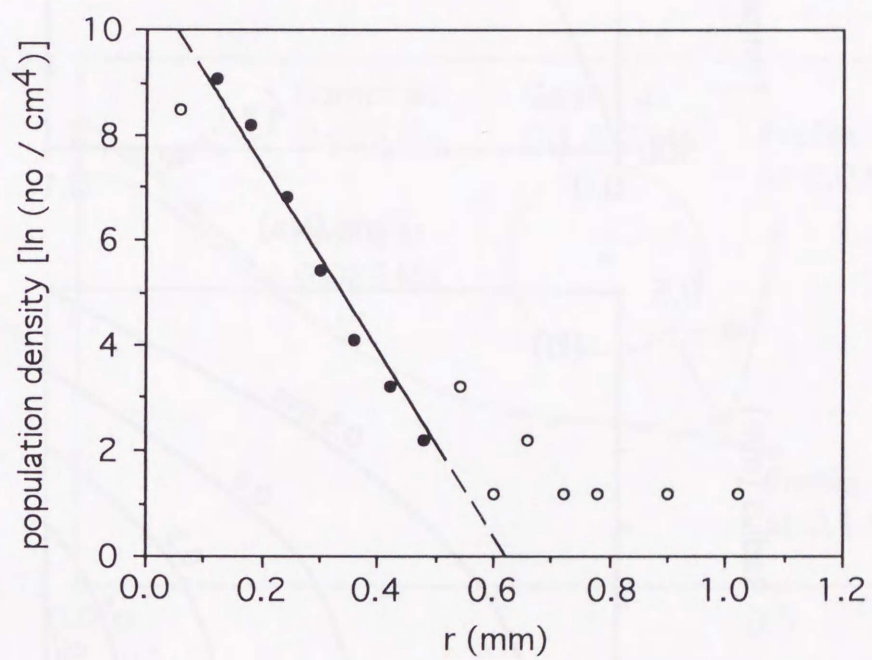
Fig. 6.5. CSD plot for the garnet grains of the studied metapelite. See text for details.
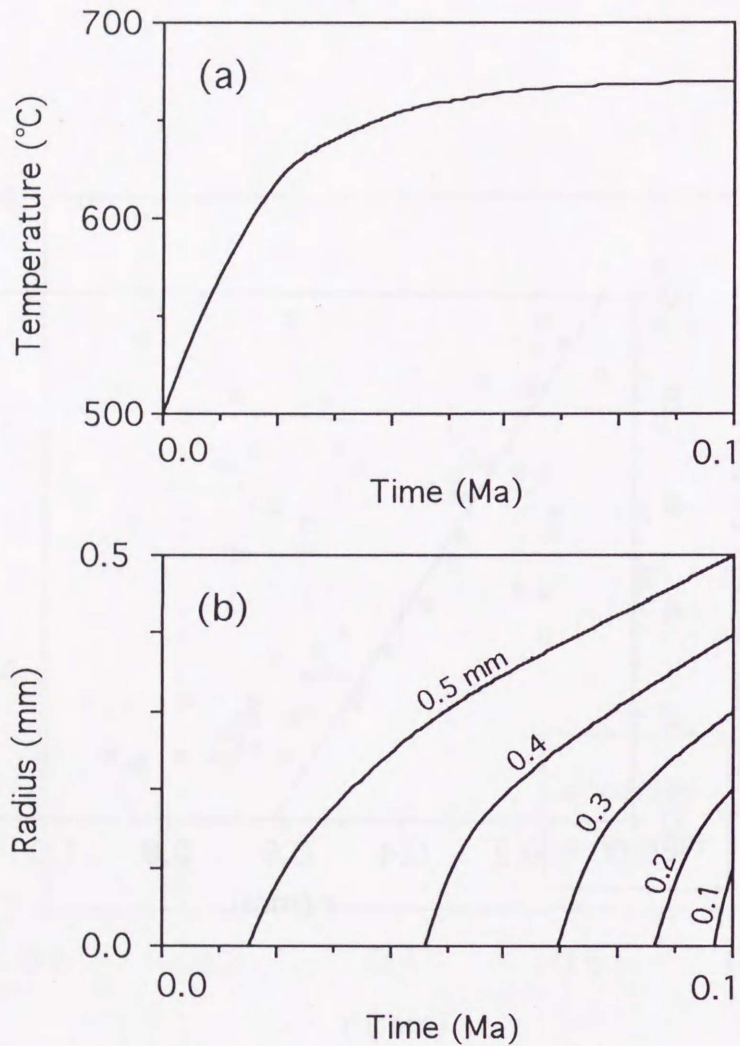
Fig. 6.6. (a) Temperature-time path during only the prograde stage of the path in Fig. 5.4b. (b) Radius - time curves of garnets with a radius of 0.5 mm (ti = 0.0150 Ma), 0.4 mm (ti = 0.0460 Ma), 0.3 mm (ti = 0.0695 Ma), 0.2 mm (ti = 0.0865 Ma), and 0.1 mm (ti = 0.0966 Ma) , respectively, corresponding to the temperature-time path of (a) using equation (10) (see text).   Nucleation of garnet crystals is continuous from the temperature above the breakdown of muscovite + quartz (600 °C) to the highest temperature (670°C), and growth of the garnets is governed by diffusion-controlled growth law during the above tempe-rature range.
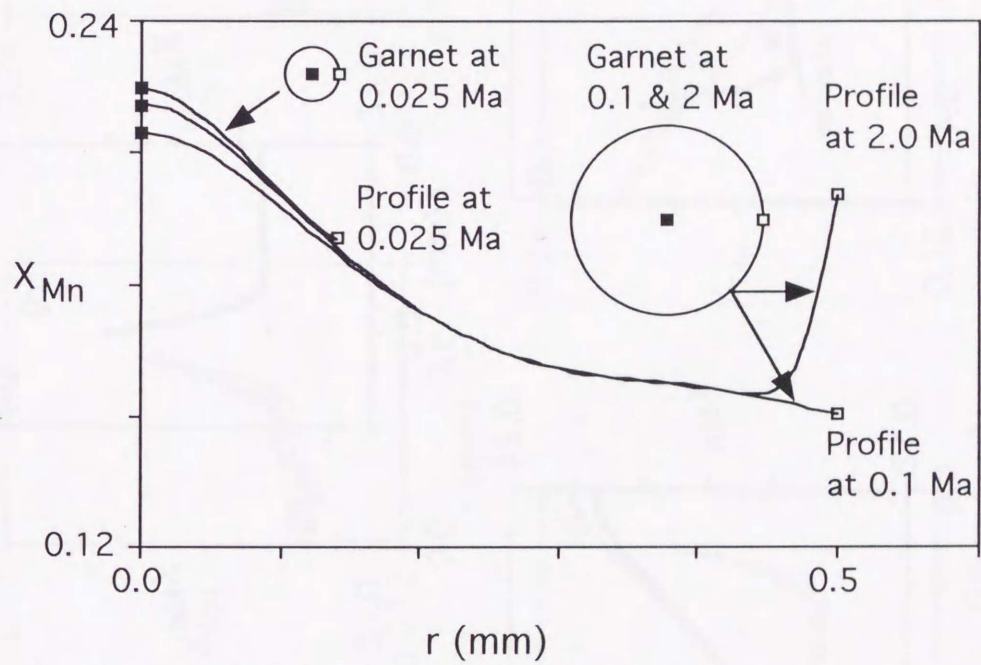
Fig. 6.7. Schematic diagram showing the changing chemical zoning (XMn) during and after growth of the garnet with a radius of 0.5 mm. See text for explanation.
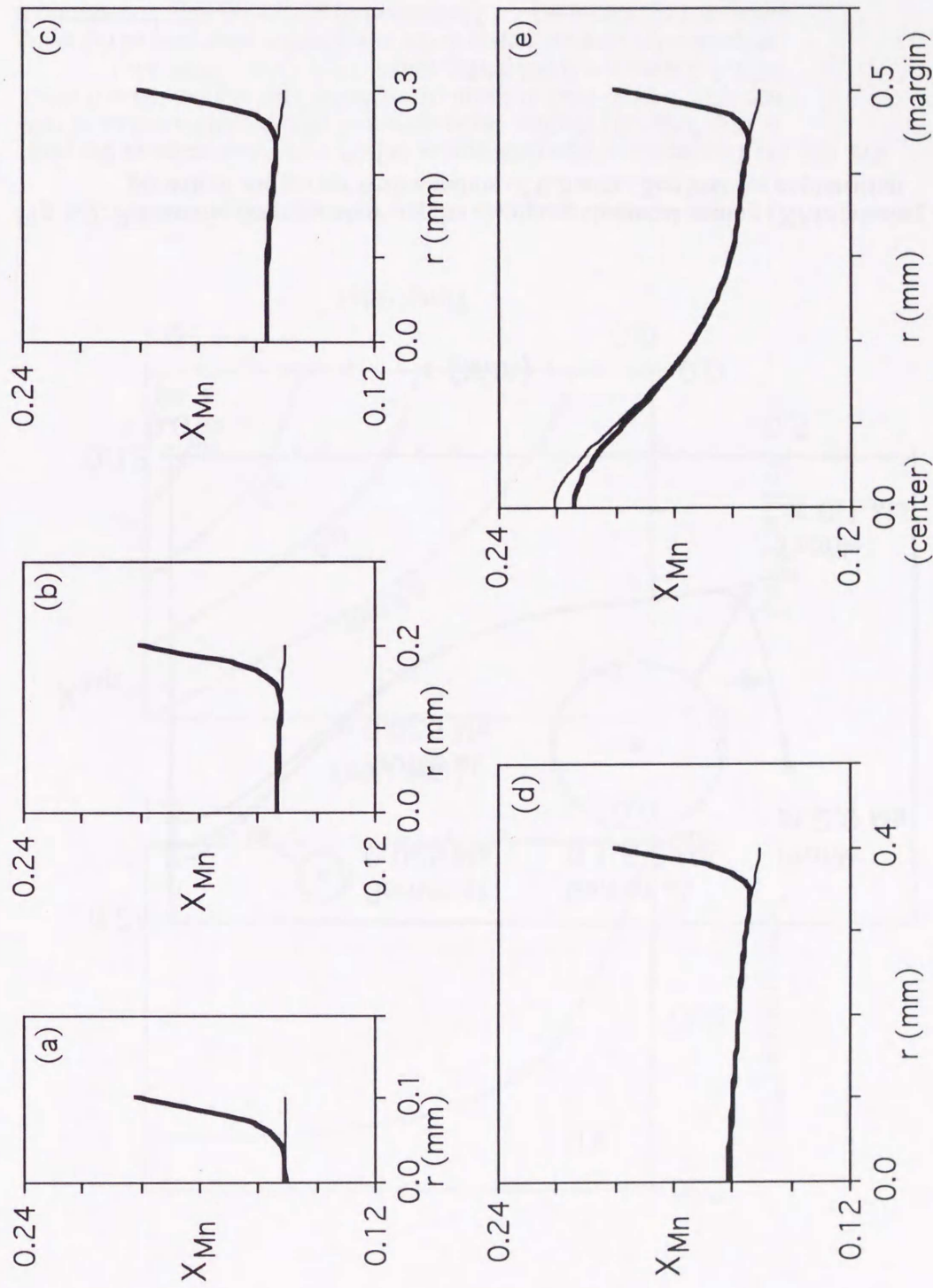
Fig. 6.8. Simulated chemical zoning patterns of different radii: (a) 0.1 mm; (b) 0.2 mm; (c) 0.3 mm; (d) 0.4 mm; and (e) 0.5 mm. Thin and thick solid lines indicate the zoning profiles at the end of growth and 2 Ma after the intrusion, respectively.
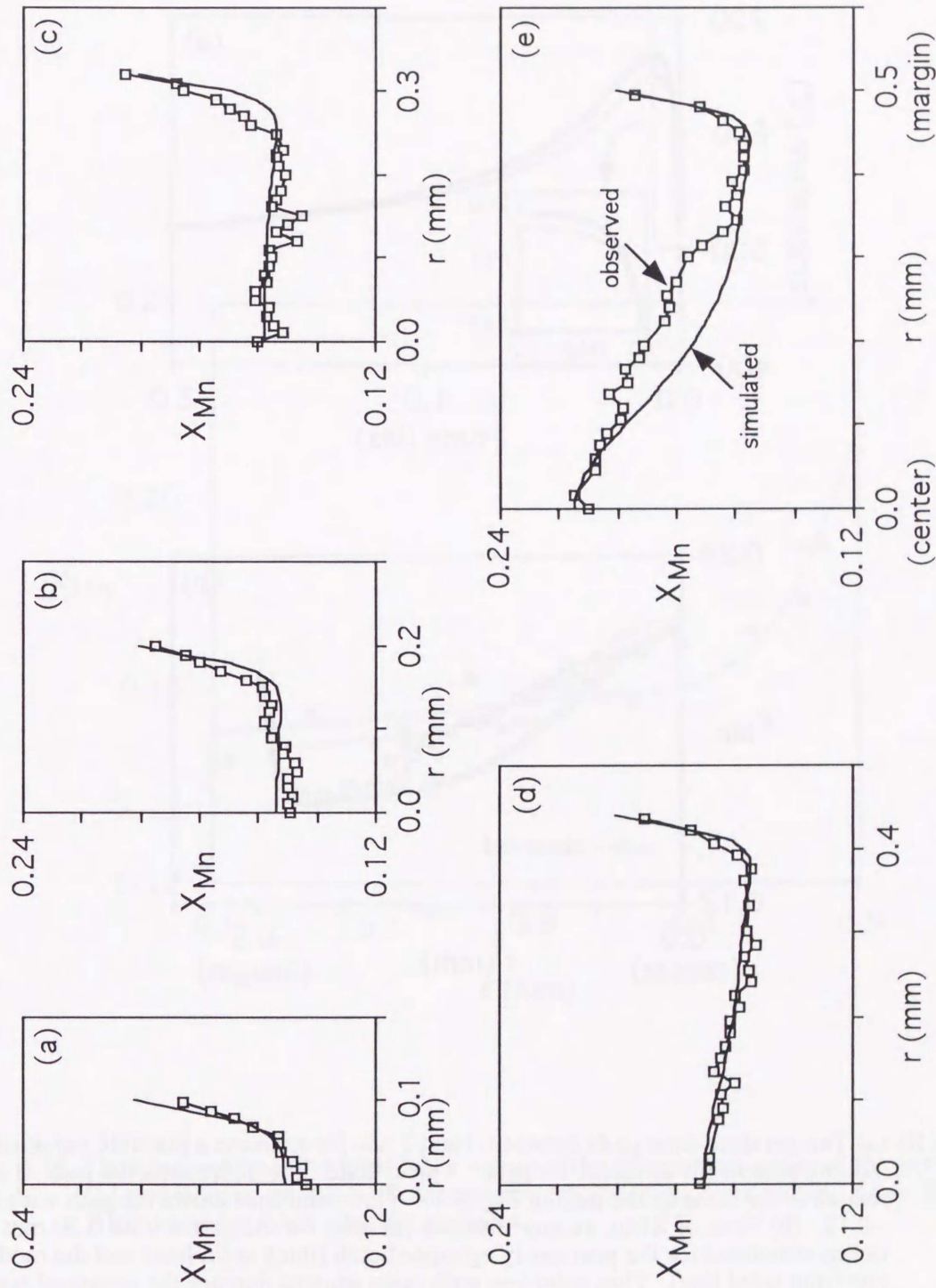
Fig. 6.9. The observed zoning profiles of garnets with different radii compared with the simulated ones after 2 Ma. (a) - (e) are the same as (a) - (e) in Fig. 6.3, respectively. Thin solid line with open squares and thin solid line denote the observed and simulated zoning profiles, respectively.
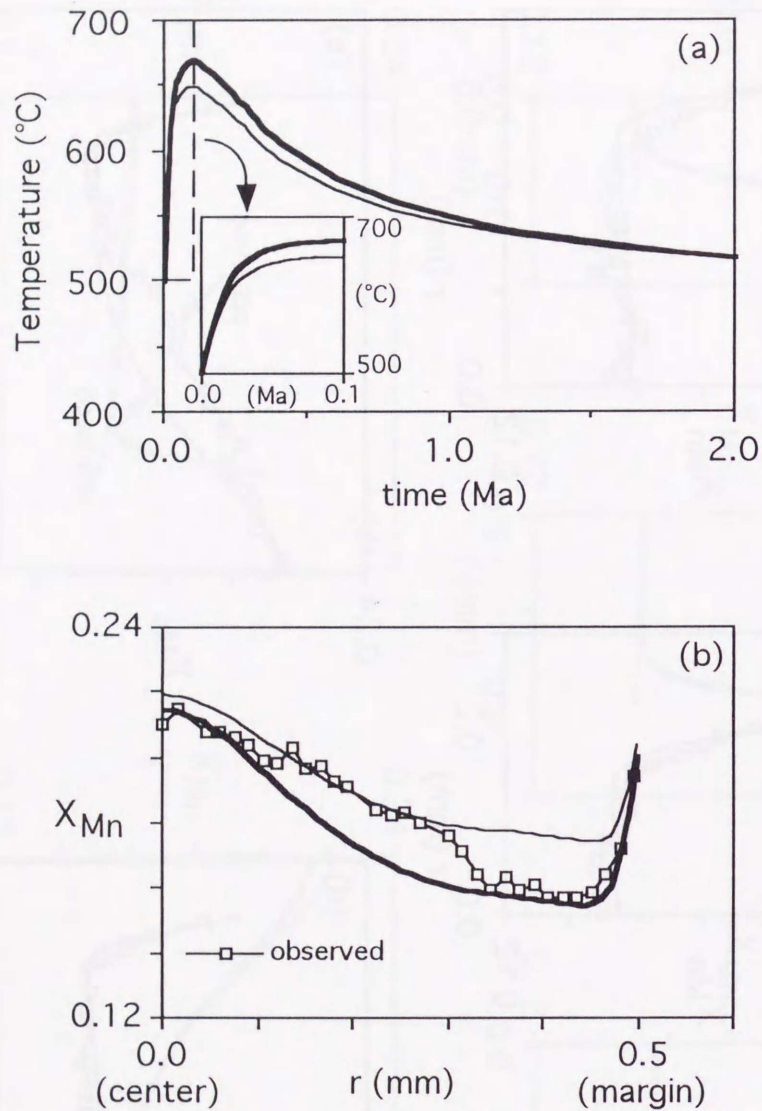
Fig. 6.10. (a) Temperature-time plots between 0 and 2 Ma for examine a possible variation of zoning pattern for different T-t path. Thick solid line represents the path (f = 0) which is the same as the path in Fig. 5.4b. Thin solid line shows the path with f = -0.12. (b) Plots of XMn versus distance (in mm) for the garnet with 0.50 mm in radius simulated for the previously estimated path (thick solid line) and the modified one (thin solid line). Thin solid line with open squares denotes the observed zoning profile for the garnet with 0.50 mm in radius (sample E). See text for details.
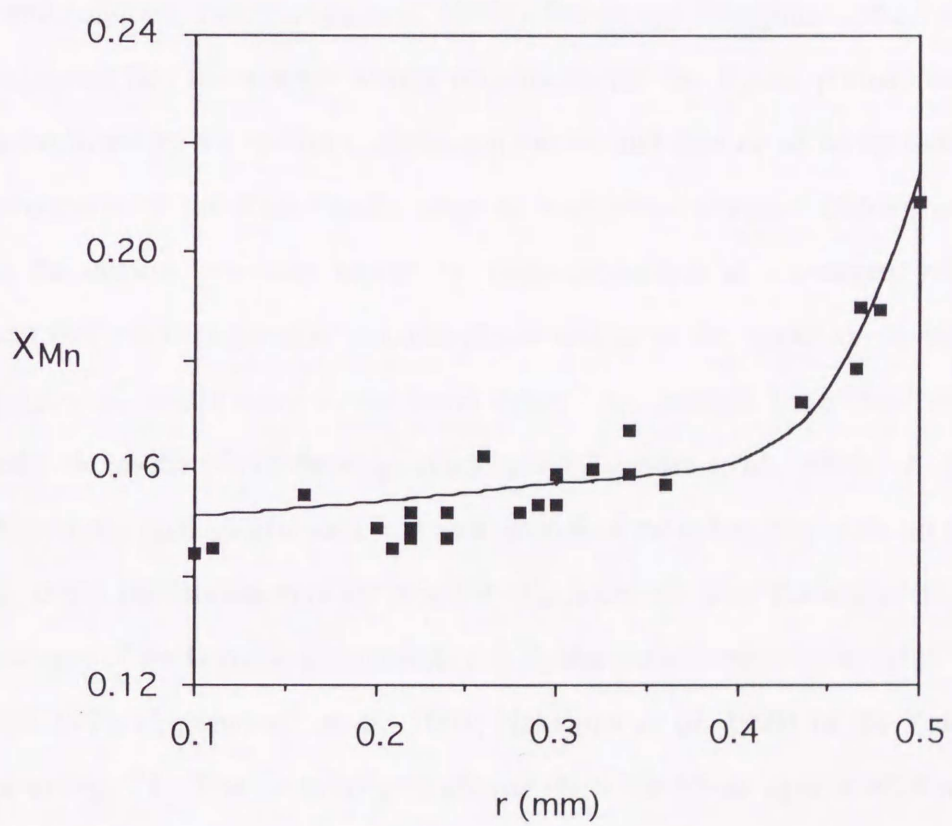
Fig. 6.11. The observed and simulated XMn values at the geometrical center of the garnets between 0.1 and 0.5 mm in radius. Solid squares: the observed XMn values. Line: the simulated XMn values at 2 Ma after the intrusion.

As mentioned in the preceding pages, the Ryoke metamorphism is mainly divided into two phases (M0 and M1). The former is nearly medium-pressure facies series metamorphism (*ca.* 30°C km^{-1}) and the latter is low-pressure facies series one (*ca.* 40 ~ 50°C km^{-1}). The geothermal gradient at M0 is comparable with that of surface heat flow of *ca.* 100 mW m^{-1}. This high heat flow is not adequate to the steady state heat flow at continental margin (cf. Turcotte and Schubert, 1982). Hara *et al.* (1991), Banno and Nakajima (1992), and Nakajima (1994) suggested that the tectonic setting responsible for the Ryoke plutono-metamorphism cannot be explained by the ordinary subduction model, and then needs an episodic event such as the subduction of the Kula-Pacific ridge at continental margin. Delong *et al.* (1979) simulated the thermal processes caused by ridge subduction at convergent margin. They pointed out that medium-pressure metamorphism occurs at the upper or middle crust, and magma generation would occur in the lower crust. As inferred from their results, M0 is considered to be resulted from the ridge subduction (Okudaira *et al.*, 1994). A chronological relationship among geological events such as transition of the subducting plate (after Maruyama and Sakai, 1986), sedimentation of the protolith (Kuga Group: after Takami *et al.*, 1990), and radiometric ages of the Gamano granodiorite and Ryoke metamorphic rocks (after Shigeno and Yamaguchi, 1976; Higashimoto *et al.*, 1983; Nakajima *et al.* 1993) in the Yanai district is illustrated in Fig. 7.1. The Gamano granodiorite show the Rb-Sr ages of 86.6 and 91.3 Ma (Shigeno and Yamaguchi, 1976), the K-Ar ages of 89.5 Ma (Higashimoto *et al.*, 1983), and the U-Pb age of 101.0 Ma (Nakajima *et al.*, 1993). The Ryoke metamorphic rocks show the Rb-Sr ages of 91.9 and 95.4 Ma (Shigeno and Yamaguchi, 1976). A minimum time interval between the ages of the Gamano granodiorite and metamorphic rocks and those of the sedimentation of protolith (Kuga Group) would be estimated to be *ca.* 30 Ma. The age of the subduction of the Kula-Pacific ridge is slightly younger than those of the Gamano granodiorite and metamorphic rocks. Therefore, the subduction of the Kula-Pacific ridge seems too late for

the heat source of the Ryoke plutono-metamorphism, and a possible heat source of the plutono-metamorphism is the subduction of the Izanagi-Farallon ridge.

The Shimonoseki Subgroup, which is upper part of the Lower Cretaceous Kanmon Group (Fig. 7.2: after Fig. 1 of Nakada and Takeda, 1995), consists of volcanic rocks and non-marine sediments, and formed during Aptian (123.5 ~ 112 Ma) to Albian (112 ~ 97 Ma), and deposited in the back- or central-arc extensional sedimentary basin (e.g. Sakai *et al.*, 1992; Itaya *et al.*, 1993; Nakada and Takeda, 1995). High-Mg andesites (HMA's) have also been found (e.g. Imaoka *et al.*, 1989). HMA's are characteristically found in crustal extension region (e.g. Tatsumi, 1995). The activity of the HMA's of the Shimonoseki Subgroup was *ca.* 105 ~ 108 Ma (Itaya *et al.*, 1993). Because these ages of HMA's are nearly comparable with those of the Gamano granodiorite and metamorphic rocks, the formation of the extensional sedimentary basin and the activity of the HMA's of the Shimonoseki Subgroup were closely related to the Ryoke plutono-metamorphism (e.g. Imaoka *et al.*, 1989; Itaya *et al.*, 1993; Nakada and Takeda, 1995).

The intrusion of the Older Ryoke granitoids could have resulted in M1. Based on the geological constraints, the *T-t* path for M1 calculated from simple 1-D numerical simulation was proposed in Chapter 4. In Chapter 5, to examine the *T-t* path, the chemical zonings of garnets were simulated for the *T-t* path using a numerical model of diffusion in combination with its growth mechanism, and they were compared with the natural ones. Because the simulated zoning profiles in different radii well fit the natural ones, it is suggested that the path is reasonable for M1. Therefore, M1 could have resulted from intrusion of the Older Ryoke granitoids at intermediate crustal levels. Consequently, it os concluded that the Ryoke metamorphic rocks were firstly heated under medium-pressure facies conditions (M0), and then they were further heated under low-pressure facies conditions (M1) by intrusion of the Older Ryoke granitoids.

The tectono-metamorphic processes of the Ryoke metamorphic belt in the Yanai district are summarized as follows.

1) The accretion of the sedimentary rocks of the Kuga Group at the eastern margin of the Asian continent, until *ca.* 140 Ma.

2) The ridge subduction at the continental margin (*ca.* 160 ~ 140 Ma), and associated generation of magma (Older Ryoke granitoids) at the lower crust, which caused the medium-pressure facies series Ryoke metamorphism (M0) at the upper and middle crust. At about the same time, the non-marine sediments of the Shimonoseki Subgroup filled the back- or central-arc basin which was created by extensional tectonics (*ca.* 120 ~ 100 Ma).

3) The northward dipping large-scale extensional fracture zones which appear to have top to the NNE ~ NE sense of shear occurred at intermediate to shallow crustal levels were generated. The Gamano granodiorite, which is one of the Older Ryoke granitoids, ascended along the northward dipping large-scale extensional fracture zones from the lower to middle crust (*ca.* 100 Ma). The emplacement of the Gamano granodiorite resulted in the low-pressure facies series Ryoke metamorphism (M1) in the upper and middle crust. At about the same time, the HMA's of the Shimonoseki Subgroup erupted (*ca.* 110 Ma). This tectonic event is called as D1.

4) Immediately after the emplacement of the Gamano granodiorite, the metamorphic sequence was modified by low-angle faults and large-scale recumbent folds (D2). The mylonite zones developed along the MTL also represent this tectonic event (e.g. Hara *et al.*, 1991; Okudaira *et al.*, 1992; Ohtomo, 1993; Sakakibara, 1995).

5) After D2, a large amount of granite (Younger Ryoke and Hiroshima granitoids) intruded as stocks. The intrusion of the granite stocks resulted in a narrow contact metamorphism of the wall rocks (M2).

6) The upright folds with E-W trending axes were formed after the intrusion of the Younger and Hiroshima granitoids (D3). The upright folds are comparable with the upright folds developed in left-hand fashion throughout the Paleozoic-Mesozoic accretionary complexes and the Ryoke metamorphic belt in the Inner Zone of southwest Japan.
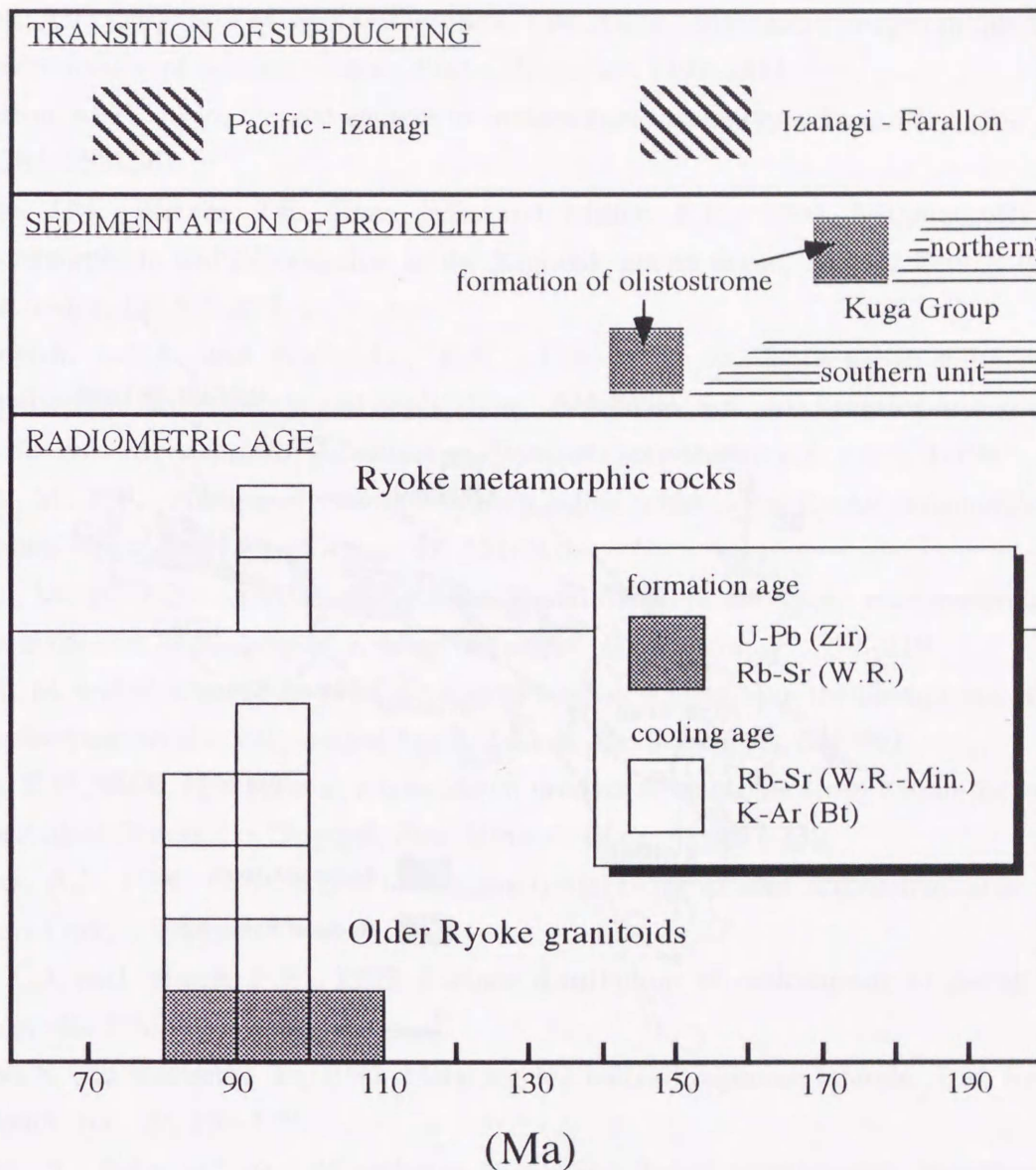
Fig. 7.1. Time relationship among geological events (transition of subducting plate, sedimentation of protolith (Kuga Group), and radiometric ages of the Older Ryoke granitoids and Ryoke metamorphic rocks) in the Yanai district. This figure is compiled from Shigeno and Yamaguchi (1976), Higashimoto *et al.* (1983), Maruyama and Sakai (1986), Takami *et al.* (1990), and Nakajima *et al.* (1993).
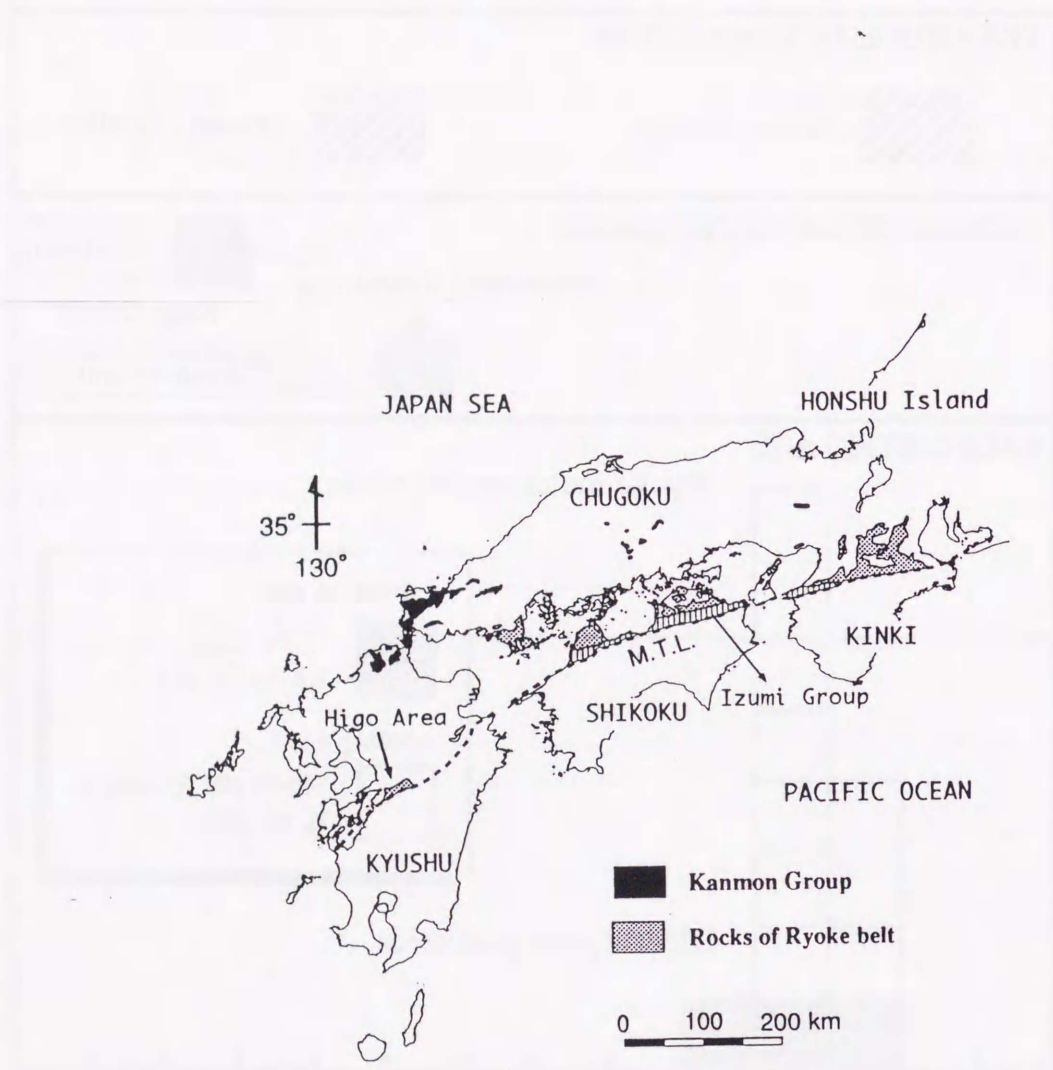
Fig. 7.2. Distribution of the Kanmon Group and rocks of the Ryoke metamorphic belt (after Fig. 1 of Nakada and Takeda, 1995). The occurrence of the Kanmon Group decreases to the east because this reagion in covered by post-Cretaceous valucanics.

REFERENCES

Ardell, A.J., Christie, J.M. and McCormick, J.W., 1974. Dislocation images in quartz and the determination of Burgers vectors. *Philos. Mag.*, 29: 1399-1411.

Atherton, M.P., 1976. Crystal growth in metamorphic tectonites. *Trans. Roy. Soc. London*, A283: 255-270.

Amato, J.M., Wright, J.E. Gans, P.B. and Miller, E.L., 1994. Magmatically induced metamorphism and deformation in the Kigluaik gneiss dome, Seward Peninsula, Alaska. *Tectonics*, 13: 515-527.

Aranovich, L.YA. and Podlesskii, K.K., 1983. The cordierite-garnet-sillimanite-quartz equilibrium: Experiments and applications. In Saxena, S.K. ed. *Kinetics and equilibrium in the mineral reactions, Advances in Physical Geochemistry*, 3: pp. 173-198.

Asami, M., 1971. Finding of staurolite-bearing pelitic schist in the Ryoke metamorphic belt of central Japan. *Proc. Japan Acad.*, 47: 551-516.

Asami, M., 1977. Two modes occurrence of staurolite from the Ryoke metamorphic rocks in the Hazu area, central Japan. *J. Mineral., petrol. Econ. Geol.*, 72: 205-219.

Asami, M. and Hoshino, M., 1980. Staurolite-bearing schists from the Hongu-san area in the Ryoke metamorphic belt, central Japan. *J. Geol. Soc. Japan*, 86: 581-591.

Atkin, B.P., 1978. Hercynite as a breakdown product of staurolite from within the aureole of the Ardara Pluton, Co. Donegal, Eire. *Mineral. Mag.*, 42: 237-239

Barker, A.J., 1990. *Introduction to Metamorphic Textures and Microstructures*. Blackie, New York, 162 pp.

Ball, C.J. and Hirsch, P.B., 1955. Surface distribution of dislocations in metals. *Philos. Mag.*, 46: 1343-1411.

Banno, S. and Nakajima, T., 1992. Metamorphic belts of Japanese Islands. *Ann. Rev. Earth Planet. Sci.*, 20: 159-179.

Banno, S., Sakai, C. and Higashino, T., 1986. Pressure-temperature trajectory of the Sanbagawa metamorphism deduced from garnet zoning. *Lithos*, 19: 51-63.

Bartlett, W.L., Friedman, M and Logan, J.M., 1981. Experimental folding and faulting of rocks under confining pressure, Part IX. Wrench faults in limestone layers. *Tectonophysics*, 79: 255-277.

Barton, M.D. and Hanson, R.B., 1989. Magmatism and the development of low-pressure metamorphic belts: Implications from the western United States and thermal modeling. *Geol. Soc. Amer. Bull.*, 101: 1051-1065.

Bateman, R., 1985. Aureole deformation by flattening around a diapir during in situ ballooning: the Cannibal Creek granite. *J. Geol.*, 93: 293-310.

Bergantz, G.W., 1991. Physical and chemical characterization of plutons. In: D.M. Kerrick (Editor), *Contact Metamorphism. Rev. Mineral.*, 26: 13-42.

Blumenfeld, P., Mainprice, D. and Bouchez, J.-L., 1986. C-slip in quartz from subsolidus deformed granite. *Tectonophysics*, 127: 97-115.

Bouchez, J.-L. and Pêcher, A., 1981. The Himalayan Main Central Thrust pile and its quartz-rich tectonites in central Nepal. *Tectonophysics*, 78: 23-50.

Bouchez, J.L. and Diot, H., 1990. Nested granites in question: Contrasted emplacement kinematics of independent magmas in the Zaer pluton, Morocco. *Geology*, 18: 966-969.

Bouchez, J.-L., Mainprice, D.H., Trépied, L. and Doukhan, J.C., 1984. Secondary lineation in a high-T quartzite (Galicia, Spain): An explanation for an abnormal fabric. *J. Struct. Geol.*, 6: 159-165.

Burn, J.P. and Pons, J., 1981. Strain patterns of pluton emplacement in a crust undergoing non-coaxial deformation, Sierra Morena, Southern Spain. *J. Struct. Geol.*, 3: 219-229.

Bussell, M.A., Pitcher, W.S. and Wilson, P.A., 1976. Ring complexes of the Peruvian coastal batholith: a longstanding subvolcanic regime. *Canadian J. Earth Sci*, 13: 1020-1030.

Carlson, W.D., 1989. The significance of intergranular diffusion to the mechanisms and kinetics of porphyroblast crystallization. *Contrib. Mineral. Petrol.*, 103: 1-24.

Carlson, W.D., 1991. Competitive diffusion-controlled growth of porphyloblasts. *Mineral. Mag.*, 55: 317-330.

Cashman, K.V. and Ferry, J.M, 1988. Crystal size distribution (CSD) in rocks and the kinetics and dynamics of crystallization III. Metamorphic crystallization. *Contrib. Mineral. Petrol.*, 99: 401-415.

Cathles, L.M., 1977. An analysis of the cooling of intrusives by ground-water convection which includes boiling. *Econ. Geol.*, 72: 804-826.

Cathles, L.M., 1981. Fluid flow and genesis of hydrothermal ore deposits. *Econ. Geol., 75th Anniv. Vol.*, 424-457.

Chakraborty, S. and Ganguly, J., 1991. Compositional zoning and cation diffusion in garnets. In: J. Ganguly (Editor), *Diffusion, Atomic Ordering, and Mass Transport, Selected Topics in Geochemistry, Adv. Phys. Geochem.*, 8: pp. 120-175.

Chapman, D.S. and Furlong, K.P. 1992. Thermal state of the continental crust. In: D.M. Fountain, R. Arculus and R.W. Kay (Editors), *Continental Lower Crust. Development in Geotectonics* 23: 179-268.

Christian, J.W., 1975. *The theory of transformations in metals and alloys: Part 1 - Equilibrium and general kinetic theory (2nd edn)*. Pergamon Press, Oxford, 586pp.

Christie, J.M. and Green, H.W., 1964. Several new slip mechanisms in quartz. *EOS*, 45: 103.

Christie, J.M. and Ardell, A.J., 1976. Deformation structures in minerals. In: H.-R. Wenk (Editor), Electron Microscopy in Mineralogy, Springer-Verlag, New York, pp. 374-403.

Crank, J., 1975. *The Mathematics of Diffusion*. Oxford University Press, London, 414pp.

DeLong, S.E, Schwarz, W.M. and Anderson, R.N., 1979. Thermal effects of ridge subduction. *Earth Planet. Sci. Lett.*, 44: 239-246.

Dempster, T.J., 1985. Garnet zoning and metamorphism of the Barrovian Type Area, Scotland. *Contrib. Mineral. Petrol.*, 89: 30-38.

De Yoreo, J.J., Lux, D.R. and Guidotti, C.V., 1989a. The role of crustal anatexis and magma migration in the thermal evolution of regions of thickened continental crust. In: J.S. Daly, R.A. Cliff and B.W.D. Yardley (Editors), *Evolution of Metamorphic Belts. Geol. So. Sp. Pub.*, 43: pp. 187-202.

De Yoreo, J.J., Lux, D.R., Guidotti, C.V., Decker, E.R. and Osberg, P.H., 1989b. The Acadian thermal history of western Maine. *J. Metamorphic Geol.*, 7: 169-190.

De Yoreo, J.J., Lux, D.R. and Guidotti, C.V., 1991. Thermal modeling in low-pressure / high-temperature metamorphic belts. *Tectonophysics*, 188: 209-238.

Drury, M.R., 1993. Deformation lamellae in metals and minerals. In: J.N. Boland and J.D. Fitz (Editors), Defects and Processes in the Solid State: Geoscience Application, Elsevier Science Publishers B.V., pp. 195-212.

England, P.C. and Thompson, A.B., 1984. Pressure-temperature-time paths of regional metamorphism I. Heart transfer during the evolution of regions of thickened continental crust. *J. Petrol.*, 25: 894-928.

Elphick, S.C., Ganguly, J. and Loomis, T.P., 1985. Experimental determination of cation diffusivities in aluminosilicate garnets I. Experimental methods and interdiffusion data. *Contrib. Mineral. Petrol.*, 90: 36-44.

Ernst, W.G., 1976. *Petrologic Phase Equilibria.* W.H Freeman, San Francisco.

Fabbri, O., 1994. Ductile extensional deformation in the low P/T Ryoke metamorphic core complex. *Abstract with Programs, 101st Ann. Meet. Geol. Soc. Japan*, pp. 195.

Ferry, J.M., 1983. Regional metamorphism of the Vassalboro Formation, southcentral Maine, USA: A case study of the role of fluid in metamorphic petrogenesis. *J. Geol. Soc. London*, 140: 551-576.

Ferry, J.M., 1986a. Reaction progress: A monitor of fluid-rock interactions during metamorphic hydrothermal events. In: J.V. Walther and B.J. Wood (Editors), *Fluid-Rock Interactions during Metamorphism. Adv. Phys. Geochem.*, 5: 60-88.

Ferry, J.M., 1986b. Infiltration of aqueous fluids and high fluid:rock ratios during greenschist facies metamorphism: A reply. *J Petrol.*, 27: 695-714.

Fisher, G.W., 1978. Rate laws in metamorphism. *Geochim. Cosmochim. Acta*, 42: 1035-1050.

Florence, F.P. and Spear, F.S., 1991. Effects of diffusional modification of garnet growth zoning on P-T calculations. *Contrib. Mineral. Petrol.*, 107: 487-500.

Furlong, K.P., Hanson, R.B., and Bowers, J.R., 1991. Modeling thermal regimes. In: D.M. Kerrick (Editor), *Contact Metamorphism. Rev. Mineral.*, 26: 437-505.

Gapais, D. and Barbarin, B., 1986. Quartz fabric transition in a cooling syntectonic granite (Hermitage Massif, France). *Tectonophysics*, 125: 357-370.

Garbutt, J.M. and Teyssier, C., 1991. Prism <c> slip in the quartzites of the Oakhurst Mylonite Belt, California. J. Struct. Geol., 13: 657-666.

Gleason, G.C., Tullis, J. and Heidelbach, F., 1993. The role of dynamic recrystallization in the development of lattice preferred orientations in experimentally deformed quartz aggregates. J. Struct. Geol., 15: 1145-1168.

Green, T.H., 1992. Experimental phase equilibrium studies of garnet-bearing I-type volcanics and high-level intrusives from Northland, New Zealand. *Trans. Roy. Soc. Edinburgh : Earth Sci.*, 83: 429-438.

Griggs, D.T. and Blacic, J.D., 1965. Quartz: anomalous weakness of synthetic crystals. *Science*, 147: 292-295.

Guidotti, C.V., Micas in metamorphic rocks. In: S.W. Bailey (Editor), *Micas, Reviews in Mineralogy*, 13: 357-468.

Guillope, M. and Poirier, J.P., 1979. Dynamic recrystallization during creep of single crystalline halite: an experimental study. J. Geophys. Res., 84: 5557-5567.

Guineberteau, B., Bouchez, J.L. and Vigneresse, J.L., 1987. The Mortagne granite pluton (France) emplaced by pull-apart along a shear zone: structural and gravimetric arguments and regional implications. *Geol. Soc. Amer. Bull.*, 99: 763-770.

Hacker, B.R., Yin, A., Christie, J.M. and Davis, G.A., 1992. Stress magnitude, strain rate, and rheology of extended middle continental crust inferred from quartz grain sizes in the whipple mountains, California. *Tectonics*, 11: 36-46.

Hanson, R.B., 1992. Effects of fluid production on fluid flow during regional and contact metamorphism. *J. Metamorphic Geol.*, 10: 87-97.

Hanson, R.B. and Barton, M.D., 1989. Thermal development of low-pressure metamorphic belts: Results from two-dimensional numerical models. *J. Geophys. Res.*, 94: 10,363-10,377.

Hara, I., 1962. Studies on the structure of the Ryoke metamorphic rocks of the Kasagi district, Southwest Japan. *J. Sci. Hiroshima Univ., Ser. C*, 4: 163-224.

Hara, I., Higashimoto, S., Mikami, T., Nishimura, Y., Okimura, Y., Sawada, T., Takeda, K., Yokoyama., S. Yokoyama, T., 1979. Paleozoic-Mesozoic Group of the Yasaka Gorge district. *The Yasaka Gorge, Joint Sci. Com. Res. Yasaka Gorge Sci. Reserve*, pp. 283-324. (in Japanese with English abstract)

Hara, I., Shoji, K., Sakurai, Y., Yokoyama, S. and Hide, K., 1980. Origin of the Median Tectonic Line and its initial shape. *Mem. Geol. Soc. Japan*, 18: 27-49.

Hara, I., Sakurai, Y., Okudaira, T., Hayasaka, Y., Ohtomo, Y. and Sakakibara, N, 1991. Tectonics of the Ryoke belt. *Excursion Guidebook of 98th Ann. Meet. Geol. Soc. Japan, Geol. Soc. Japan*, pp. 1-20 (in Japanese).

Hara, I., Shiota, T., Hide, K., Kanai, K., Goto, M., Seki, S., Kaikiri, K., Takeda, K., Hayasaka, Y., Miyamoto, T., Sakurai, Y., Ohtomo, Y., 1992. Tectonic evolution of the

Sambagawa schists and its implications in convergent process. *J. Sci. Hiroshima Univ., Ser. C*, 9: 495-595.

Haselton, H.T., Hovis, G.L., Hemingway, B.S. and Robie, R.A., 1983. Calorimetric investigation of the excess entropy of mixing in analbite-sanidine solid solution: lack of evidence for Na, K short-range order and implications for two-feldspar thermometry. *Amer. Mineral.*, 68: 398-413.

Hayashi, T., 1994. Geological and petrological studies on the Hiroshima Granite in the Togouchi-Yuu-Takehara district, southwest Japan. Ph.D. thesis, Hiroshima Univ., 76pp.

Herzig, C.T., Kimbrough, D.C., Tainosho Y., Kagami, H, Iizumi, S. and Hayasaka, Y., 1995. Early Cretaceous U/Pb zircon ages and Precambrian crustal unheritance in Ryoke Belt granitoids, Kinki and Yanai districts, Japan. *Geochem.l J.* (submitted).

Higashimoto, S., Nureki. T., Hara, I., Tsukuda, E. and Nakajima, T., 1983. Geology of the Iwakuni district. *Quadrangle series, scale 1 : 50,000. Geol. Surv. Japan*, 79 pp. (in Japanese with English abstract).

Hirsch, P.B., Howie, A., Nicholson, R.B., Pashley, D.W. and Whelan, M.J., 1965. *Electron microscopy of thin crystals*. Butterworth Ltd., London, 563 pp.

Hirth, G. and Tullis, J., 1992. Dislocation creep regimes in quartz aggregates. *J. Struct. Geol.*, 14: 145-159.

Hobbs, B.E., 1981. The influence of metamorphic environment upon the deformation of minerals. *Tectonophysics*, 78: 335-383.

Hobbs, B.E., 1984. Point defect chemistry of minerals under a hydrothermal environment. *J. Geophys. Res.*, 89, 4026-4038.

Hobbs, B.E., 1985. The geological significance of microfabric analysis. In: H.-R. Wenk (Editor), *Preferred Orientation in Deformed Metals and Rocks: An Introduction to Modern Texture Analysis*. Academic Press, London, pp. 463-484.

Hobbs, B.E., McLaren, A.C. and Paterson, M.S., 1972. Plasticity of single crystals of synthetic quartz. In: H.C. Heard, I.Y. Borg, N.L. Carter and C.B. Raleigh (Editors), *Flow and Fracture of Rocks*. American Geophysical Union, Geophys. Monograph, 16: pp. 29-53.

Hodges, K.V. and Silverberg, D.S., 1988. Thermal evolution of the Greater Himalaya, Garhwal, India. *Tectonics*, 7: 583-600.

Hoisch, T.D., 1987. Heat transport by fluids during Late Cretaceous regional metamorphism in the Big Maria Mountains, southeastern California. *Geol. Soc. Am. Bull.*, 98: 549-553.

Holdaway, M.J. and Lee, S.M., 1977. Fe-Mg cordierite stability in high-grade pelitic rocks based on experimental, theoretical, and natural observations. *Contrib. Mineral. Petrol.* 63: 175-198.

Honma, H., 1974. Major element chemistry of metamorphic and granitic rocks of the Yanai district in the Ryoke belt. *J. Mineral. petrol. Econ. Geol.*, 69: 193-204.

Honma, H. and Sakai, H., 1975. Oxygen isotope study of metamorphic and granitic rocks of the Yanai district in the Ryoke belt, Japan. *Contrib. Mineral. petrol.*, 52: 107-120.

Hutton, D.H.W., 1982. A tectonic model for the emplacement of the Main Donegal granite, NW Ireland. *J. Geol. Soc. London*, 139: 615-631.

Hutton, D.H.W., 1988. Granite emplacement mechanisms and tectonic controls: inferences from deformation studies. *Trans. Roy. Soc. Edinburgh. Earth Sci.*, 79: 245-255.

Hutton, D.H.W., Dempster, T.J., Brown, P.E. and Becker, S.D., 1990. A new mechanism of granite emplacement: intrusion in active extensional shear zones. *Nature*, 343, 452-455.

Hubbert, M.K., 1940. The theory of ground-water motion. *J. Geol.*, 48: 785-944.

Ikeda, T., 1991. Heterogeneous biotite from Ryoke metamorphic rocks in the Yanai district, southwest Japan. *J. Geol. Soc. Japan*, 97: 537-547.

Ikeda, T., 1993a. Compositional zoning patterns of garnet during prograde metamorphism from the Yanai district, Ryoke metamorphic belt, southwest Japan. *Lithos*, 30: 109-122.

Ikeda, T., 1993b. Homogenization of chemical zoning of garnet of the Ryoke metamorphic rocks from the Yanai district. *Earth Monthly*, 15: 164-167 (in Japanese).

Ishioka, K. 1974. Finding of an orbicular structure at Kinno, Nagano-ken, and its bearing on the genesis of the Tenryukyo granite. *J. Geol. Soc. Japan*, 80: 593-618.

Itaya, T., Hyodo, H. and Fukui, S., 1993. Numerical experiments for recovery of reversed thermal structure in arc-trench system: New constraints on orogenic process. In: M. Komatsu, T. Takeshita and M. Sakakibara (Editors), *Evolution of the arc crust in Southwest Japan. Mem. Geol. Soc. Japan*, 42: pp. 351-357 (in Japanese with English abstract).

Jaeger, J.C., 1964. Thermal effects of intrusions. *Rev. Geophys.*, 2: 44-54.

Kagami, H., Iizumi, S., Tainosho, Y. and Owada, M., 1992. Spatial variations of Sr and Nd isotope ratios of Cretaceous-Paleogene granitoid rocks, southwest Japan arc. *Contrib. Mineral. Petrol.*, 112: 165-177.

Kawakami, S., Kanaori, Y. and Yairi, K., 1991. Deformation structures of granitoids and tectonics associated with their emplacement. *J. Mineral. Petrol. Econ. Geol.*, 86: 125-139 (in Japanese with English abstract).

Kerrick, D.M., 1972. Experimental determination of muscovite + quartz stability with $P_{H_2O} < P_{total}$. American Journal of Science, 272: 946-958.

Kerrick, D.M., Lasaga, A.C. and Raeburn, S.P., 1991. Kinetics of heterogeneous reactions. In: D.M. Kerrick (Editor), *Contact Metamorphism. Rev. Mineral.*, 26: pp. 583-672.

Kock, P.S., Christie, J.M., Ord, A. and George, Jr., R.P., 1989. Effect of water on the rheology of experimentally deformed quartzites. *J. Geophys. Res.*, 94: 13975-13996.

Koide, H., 1958. *Dando granodioritic intrusives and their associated metamorphic complex*. Japan Soc. Prom. Sci., Tokyo, 311pp.

Kojima, G. 1955. Contributions to the knowledge of mutual relations between three metamorphic zones of Chugoku and Shikoku, Southwestern Japan. *J. Hiroshima Univ., Ser. C*, 1: 17-46.

Kojima, G. and Okamura, Y., 1968. On the Kitaoshima granite gneiss complex. *J. Hiroshima Univ., Ser. C*, 5: 295-306.

Kretz, R., 1973. Kinetics of the crystallization of garnet at two localities near Yellowknife. *Canadian. Mineral.*, 12: 1-20.

Kretz, R., 1974. Some models for the rate of crystallization of garnet in metamorphic rocks. *Lithos*, 7: 123-131.

Kronenberg, A.K. and Tullis, J., 1984. Flow strengths of quartz aggregates: grain size and pressure effects due to hydrolytic weakening. *J. Geophys. Res.*, 89: 4281-4297.

Kutsukake, T., 1977. Nature of the Ryoke regional metamorphism and plutonism. *Monograph Assoc. Geol. Coll. Japan*, 20: 37-44 (in Japanese with English abstract).

Law, R.D., Knipe, R.J. and Dayan, H., 1984. Strain path partitioning within thrust sheets: microstructural and petrofabric evidence from the Moine Thrust zone at Loch Eriboll, northwest Scotland. *J. Struct. Geol.*, 6: 477-497.

Liddell, N.A., Phakey, P.P. and Wenk, H.-R., 1976. The microstructure of some naturally deformed quartzites. In: H.-R. Wenk (Editor), *Electron Microscopy in Mineralogy*. Springer-Verlag, New York, pp. 419-427.

Linker, M.F., Kirby, S.H., Ord, A. and Christie, J.M., 1984. Effects of compression direction on the plasticity and rheology of hydrolytically weakened synthetic quartz crystals at atmospheric pressure. *J. Geophys. Res.*, 89: 4241-4255.

Lister, G.S., 1977. Crossed-girdle *c*-axis fabrics in quartzites plastically deformed by plane strain and progressive simple shear. *Tectonophysics*, 39: 51-54.

Lister, G.S., 1981. The effect of the basal-prism mechanism switch on fabric development during plastic deformation of quartzite. *J. Struct. Geol.*, 3: 67-75.

Lister, G.S. and Hobbs, B.E., 1980. The simulation of fabric development during plastic deformation and its application to quartzite: the influence of deformation history. *J. Struct. Geol.*, 2: 355-370.

Lister, G.S. and Dornsiepen, U.F., 1982. Fabric transitions in the Saxony granulite terrain. *J. Struct. Geol.*, 4: 81-92.

Lister, G.S., Paterson, M.S. and Hobbs, B.E., 1978. The simulation of fabric development in plastic deformation and its application to quartzite: the model. *Tectonophysics*, 45: 107-158.

Logan, J.M., Friedman, M., Higgs, N.G., Dengo, C. and Shimamoto, T., 1979. Experimental studies of simulated gouge and their application to studies of natural fault gouge. *Proc. Conf. VIII, Anal. Actual Fault Zones in Bedrock*. U.S. Geol. Surv. Open-File Rept. 79-1239, pp. 305-343

Loomis, T.P., 1983. Compositional zoning of crystal: A record of growth and reaction history. In: S.K. Saxena (Editor), *Kinetics and Equilibrium in Mineral Reaction. Adv. Phys. Geochem.*, 3: pp. 1-61.

Loomis, T.P., Ganguly, J. and Elphick, S.C., 1985. Experimental determination of cation diffusivities in aluminosilicate garnets II. Multicomponent simulation and tracer diffusion coefficients. *Contrib. Mineral. Petrol.*, 90: 45-51.

Loosveld, R.J.H., 1989a. The synchronism of crustal thickening and high T / P metamorphism in the Mount Isa Inlier, Australia 1. An example, the central Soldiers Cap belt. *Tectonophysics*, 158: 173-190.

Loosveld, R.J.H., 1989b. The synchronism of crustal thickening and low-pressure facies metamorphism in the Mount Isa Inlier, Australia 2. Fast convective thinning of mantle lithosphere during crustal thickening. *Tectonophysics*, 165: 191-218.

Lux, D.R., De Yoreo, J.J., Guidotti, C.V. and Decker, E.R., 1986. The role of plutonism in low-pressure/high-temperature metamorphic belt formation. *Nature*, 323: 794-797.

Mahon, K.I., Harrison, T.M. and Drew, D.A. 1988. Ascent of a granitoid diapir in a temperature varying medium. *J. Geophys. Res.* 93: 1174-1188.

Mainprice, D., Bouchez, J.-L., Blumenfeld, P. and Tubiá J.M., 1986. Dominant *c* slip in naturally deformed quartz: Implications for dramatic plastic softening at high temperature. *Geology*, 14: 819-822.

Maruyama. S. and Sakai, H., 1986. Tectonics of Asia as a composite continent. *Monograph Assoc. Geol. Collab. Japan*, 31: 487-518 (in Japanese with English abstract).

McCormick, J.W., 1977. Transmission electron microscopy of experimentally deformed synthetic quartz. Ph.D. thesis, Univ. of California, Los Angeles, 171 pp.

McLaren, A.C., 1991. *Transmission electron microscopy of minerals and rocks*. Cambridge Univ. Press, Cambridge, 387 pp.

Miyashiro, A., 1961. Evolution of metamorphic belts. *J. Petrol.*, 2: 277-311.

Miyashira, A., 1994. *Metamorphic Petrology*. UCL Press, London, 404 pp.

Miyashita, Y. and Komatsu, M., 1993. The relationship between growth of K-feldspar and garnet porphyroblasts and foliations of the Ryoke belt in the Yanai district. *Abstract with Programs, 100th Ann. Meet. Geol. Soc. Japan*, pp. 632 (in Japanese).

Miyashita, Y and Komatsu, M., 1994. K-feldspar porphyroblast growth and kinematics of the Ryoke metamorphic belt in the Yanai area. *Abstract with Programs, 101st Ann. Meet. Geol. Soc. Japan*, pp. 246 (in Japanese).

Nakada, M. and Takeda, Y., 1995. Roles of mantle diapir and ductile lowe crust on island-arc tectonics. *Tectonophysics*, 246: 147-162.

Nakajima, T., 1994. The Ryoke metamorphic belt: crustal section of the Cretaceous Eurasian continental margin. *Lithos*, 33: 51-66.

Nakajima, T., Shirahase, T. and Shibata, K., 1990. Along-arc variation of Rb-Sr and K-Ar ages of Cretaceous granitic rocks in southwest Japan. *Contrib. Mineral. Petrol.*, 104: 381-389.

Nakajima, T., Williams, I.S. and Watanabe, T., 1993. SHRIMP U-Pb ages of the Ryoke and San-yo granitoids in Southwest Japan, *Abstracts with Programs, 100th Ann. Meet. Geol. Soc. Japan*, 584 (in Japanese).

Nicolas, A. and Poirier, J.P., 1976. *Crystalline plasticity and solid state flow in metamorphic rocks.* John Wiley and Sons, London, 444pp.

Nishimura, Y., Isozaki, Y. and Nureki, T., 1985. Sangun-Chugoku Belt and Ryoke belt in the eastern part of Yamaguchi Prefecture. *Excursion Guidebook of 92th Ann. Meet. Geol. Soc. Japan*, 17-49, Geol. Soc. Japan (in Japanese).

Nishiyama, T. and Miyazaki, K., 1994. Crystal size distributions and spatial dispositions of metamorphic minerals. *J. Mineral. Soc. Japan*, 23, 91-103 (in Japanese with English abstract).

Norton, D. and Cathles, L.M., 1979. Thermal aspects of ore deposition. In: H.L. Barnes (Editor), *Geochemistry of Hydrothermal Ore Deposits*, John Wiley and Sons, New York, 2: 611-631.

Norton, D. and Taylor, H.P., 1979. Quantitative simulation of the hydrothermal systems of crystallizing magmas on the basis of transport theory and oxygen isotope data: an analysis of the Skaergaad intrusion. *J. Petrol.*, 20: 421-486.

Nureki, T., 1960. Structural investigation of the Ryoke metamorphic rocks of the area between Iwakuni and Yanai, Southwestern Japan. *J. Sci. Hiroshima Univ., Ser. C*, 3: 69-141.

Nureki, T., 1974. Contact metamorphism in the So-o district, Yamaguchi Prefecture, Japan - with special reference to the occurrence of sillimanite. *Mem. Geol. Soc. Japan* 11: 251-281.

Nureki, T., Enami, M., Shiota, T. and Shibata, T., 1992. Paired metamorphic belts: Ryoke and Sanbagawa. *IGC Field Trip Guide Book*, 5: 103-132.

Ohtomo, Y., 1993. Origin of the Median Tectonic Line. *J. Sci. Hiroshima Univ. Ser C*, 9: 611-699.

Okamura, Y., 1960. Structural and petrological studies on the Ryoke gneiss and granodiorite of the Yanai district, Southwest Japan. *J. Sci. Hiroshima Univ., Ser. C*, 3: 143-213.

Okudaira, T., 1995a. An examination of temperature-time path for the low-pressure facies series Ryoke metamorphism based on chemical zoning in garnets. *J. Metamorphic Geol.* (in press).

Okudaira, T., 1995b. Thermal evolution of the Ryoke metamorphic belt in the Yanai district, southwest Japan. *The Island Arc* (in review)

Okudaira, T., Hara, I., Sakakibara, N., Sakurai, Y. and Hayasaka, Y., 1992. Tectonics of magma arc as inferred from tectono-metamorphic processes of the Ryoke belt of Southwest Japan. *Abstract with Programs, 29th IGC*, vol. 2 of 3, 467.

Okudaira, T., Hara, I., Sakurai, Y. and Hayasaka, Y., 1993. Tectono-metamorphic processes of the Ryoke belt in the Iwakuni-Yanai district, southwest Japan. In: M. Komatsu, T. Takeshita and M. Sakakibara (Editors), *Evolution of the arc crust in Southwest Japan. Mem. Geol. Soc. Japan*, 42: pp. 91-120.

Okudaira, T., Hara, I. and Takeshita, T., 1994. Thermal modeling for the low-pressure facies series Ryoke metamorphism. *Earth Monthly*, 16: 486-489 (in Japanese).

Okudaira, T., Hara, I. and Takeshita, T., 1995a. Emplacement mechanism of the Older Ryoke granites in the Yanai district, southwest Japan, with special reference to extensional deformation in the Ryoke metamorphic belt. *J. Sci. Hiroshima Univ. Ser C*, 10: 357-366.

Okudaira, T., Takeshita, T., Hara, I. and Ando, J., 1995b. A new estimate of the conditions for transition from basal <a> to prism [c] slip in naturally deformed quartz. *Tectonophysics* (in press).

Owada, M., 1989. Geology and chemical composition of granitic rocks in the southern part of the Hidaka metamorphic belt, with special reference to cordierite-bearing granitic rocks. *J. Geol. Soc. Japan*, 95: 227-240 (in Japanese with English Abstract).

Oxburgh, E.R. and Turcotte, D.L., 1971. Origin of paired metamorphic belts and crustal dilation in island arc regions. *J. Geophys. Res.*, 76: 1315-1327.

Paterson, S.R., Vernon, R.H., Fowler, T.K.Jr., 1991. Aureole tectonics. In: M. Kerrick (Editor), *Contact Metamorphism. Rev. Mineral.*, 26: pp. 673-722.

Peacock, S.M., 1989. Numerical constrains on rates of metamorphism, fluid production, and fluid flux during regional metamorphism. *Geol. Soc. Amer. Bull.*, 101: 476-486.

Peacock, S.M., 1991. Thermal modeling of metamorphic pressure-temperature-time paths: A forward approach. In: F.S. Spear and S.M. Peacock (Editors), *Metamorphic Pressure-Temperature-Time Paths. Short Course in Geology*, 7: pp. 57-102.

Perchuk, L.L., 1977. Thermodynamic control of metamorphic processes. In: S.K. Saxena and S. Bhattacharji (Editors), *Energetics of geological processes.* Springer-Verlag, pp. 285-352.

Pitcher, W.S., 1979. The nature, ascent and emplacement of granitic magmas. *J. Geol. Soc. London*, 136: 627-662.

Platt, J.P. and Vissers, R.M.L., 1980. Extensional structures in anisotropic rocks. *J. Struct. Geol.*, 2: 397-410.

Pownceby, M.I., Wall, V.J. and O'Neill, H.St.C., 1987. Fe-Mn partitioning between garnet and ilmenite: experimental calibration and applications. *Contrib. Mineral. Petrol.*, 97: 116-126.

Price, G.P., 1985. Preferred orientations in quartzites. In: H.-R. Wenk (Editor), *Preferred Orientation in Deformed Metals and Rocks: An Introduction to Modern Texture Analysis.* Academic Press, London, pp. 385-406.

Ramsay, J.G., 1989. Emplacement kinematics of a granite diapir: the Chindamora batholith, Zimbabwe. *J. Struct. Geol.*, 11: 191-210.

Ridley, J. and Thompson, A.B., 1986. The role of mineral kinetics in the development of metamorphic microtextures. In: J.V. Walther and B.J. Wood (Editors), *Fluid-Rock Interactions During Metamorphism. Adv. Phys. Geochem.*, 5: pp. 154-193.

Rothstein, D.A. and Hoisch, T.D., 1994. Multiple intrusions and low-pressure metamorphism in the central Old Woman Mountains, south-eastern California: constraints from thermal modelling. *J. Metamorphic Geol.*, 12: 723-734.

Rubey, W.W. and Hubbert, M.K., 1959. Role of fluid pressure in mechanics of overthrust faulting I. Mechanics of fluid-filled porous solids and its applications to overthrust faulting. *Geol. Soc. Amer. Bull.*, 70: 115-166.

Rumble, D., Ferry, J.M. Hoering, T.C. and Boucot, J.B.H. 1982. Fluid flow during metamorphism at the Beaver Brook fossil locality, New Hampshire. *Amer. J. Sci.*, 282: 886-919.

Ryoke Research Group, 1972. The mutual relations of the granitic rocks of the Ryoke metamorphic belt in Central Japan. *Earth Sci.* 26: 205-216 (in Japanese with English abstract).

Ryoke Research Group, 1974. Geology of the Ryoke belt in the southern region to Sakurai, Nara Prefecture, kinki district, Japan. *Earth Sci.*, 28: 103-114 (in Japanese with English abstract).

Sakai, T., Okada, H. and Aihara, A., 1992. Cretaceous and Tertiary active margin sedimentation: Transect of Kyushu. *Paleozoic and Mesozoic Terranes: Basement of the Japanese Island Arcs*, 29th IGC Field Trip Guide Book Vol. 1: pp. 317-354

Sakakibara, N., 1995. Structural evolution of multiple ductile shear zone system in the Ryoke belt, Kinki Province.*J. Sci. Hiroshima Univ.*, 10: 267-332.

Sakurai, Y. and Hara, I., 1979. Studies on the microfabrics of granites, with special reference to their quartz microfabrics. *Mem. Geol. Soc. Japan*, 17: 287-294 (in Japanese with English abstract).

Sakurai, Y., Yoshida, H. and Hara, I., 1983. Intrusion mechanism of a granite batholith. *J. Sci. Hiroshima Univ.*, 8: 103-122.

Sakurai, Y. and Hara, I., 1990. Deformation styles and tectonics of granitic rocks of the Ryoke belt (I) Deformation styles of plagiclase. *Earth Montly*, 12: 457-461 (in Japanese).

Seo, T., Yokoyama, S. and Hara, I., 1981. Metamorphism and tectonism of the Ryoke metamorphic belt. In: I. Hara, (Editor), *Tectonics of Paired Metamorphic Belts*, Hiroshima Univ. Press, pp. 65-72.

Shigeno, H. and Yamaguchi, M., 1976. A Rb-Sr isotopic study of metamorphism and plutonism in the Ryoke belt, Yanai district, Japan. *J. Geol. Soc. Japan*, 82: 687-698 (in Japanese with English abstract).

Shimamoto, T., 1989. Mechanical behavior of simulated halite shear zones: implications for seismicity along subduction plate boundaries. In: S. Karato and M. Toriumi (Editors), *Rheology of Solid and of the Earth*. Oxford Univ. Press, pp. 351-373.

Shimura, T., 1992. Intrusion of granitic magma and uplift tectonics of the Hidaka metamorphic belt, Hokkaido. *J. Geol. Soc. Japan*, 98: 1-20 (in Japanese with English abstract).

Skempton, A.W., 1966. Some observations on tectonic shear zones. *Proc. 1st. Congr. Internat. Soc. Rock Mech. Lisbon*, 1: pp. 329-335.

Sisson, V.B. and Hollister, L.S., 1988. Low-pressure facies series metamorphism in an accretionary sedimentary prism, southern Alaska. *Geology*, 16: 358-361.

Spear, F.S., 1988. Metamorphic fractional crystallization and internal metasomatism by diffusional homogenization of zoned garnets. *Contrib. Mineral. Petrol.*, 99: 507-517.

Spear, F.S., 1989a. Relative thermobarometry and metamorphic P-T paths. In: J.S. Daly, R.A. Cliff and W.D. Yardley (Editors), *Evolution of Metamorphic Belts. Geol. So. Sp. Pub.*, 43: pp. 63-82.

Spear, F.S., 1989b. Petrologic determination of metamorphic pressure-temperature-time paths. In: F.S. Spear and S.M. Peacock (Editors), *Metamorphic Pressure-Temperature-Time Paths. Short Course in Geology*, 7: pp. 1-55.

Spear, F.S., 1991. On the interpretation of peak metamorphic temperatures in light of garnet diffusion during cooling. *J. Metamorphic Geol.*, 9: 379-388.

Spear, F.S., 1993. *Metamorphic Phase Equilibria and Pressure-Temperature-Time Paths.* Mineral. Soc. America, Washington, D.C., 799 pp.

Spence, D.A. and Turcotte, D.L. 1985. Magma-driven propagation of cracks. *J. Geophys. Res.* 90: 575-580.

Spera, F.A. 1980. Thermal evolution of plutons: a parameterized approach. *Science*, 207: 294-301.

Spohn, T. and Schubert, G., 1982. Convective thinning of the lithosphere: A mechanism for the initiation of continental rifting. *J. Geophys. Res.*, 87: 4669-4681.

Spry, A., 1969. *Metamorphic Textures.* Pergamon Press, New York, 352 pp.

Stormer, J.C., 1975. A practical two-feldspar geothermometer. *Am. Mineral.*, 60: 667-674.

Stormer, J.C. and Whitney, J.A., 1977. Two-feldspar geothermometry in granulite facies metamorphic rocks. *Contrib. Mineral. Petrol.*, 65: 123-133.

Sugimura, A. and Uyeda, S, 1973. *Island arcs, Japan and its environs. Develop. Geotectonics*, 3, Elsevier, Amsterdam, 247pp.

Suwa, K., 1973. Metamorphic rocks occurring along the Median Tectonic Line in the Japan Island: Ryoke and Sambagawa metamorphic belts. In: R. Sugiyama (Editor), *Median Tectonic Line,* Tokai Univ. Press, 221-238 (in Japanese with English abstract).

Takami, M., Isozaki, Y., Nishimura, Y. and Itaya, T., 1990. Geochronology of weakly metamorphosed Jurassic accretionary complex (the Kuga Group) in eastern Yamaguchi Prefecture, southwest Japan. *J. Geol. Sci. Japan*, 96: 669-681 (in Japanese with English abstract).

Takeshita, T., 1989. Plastic anisotropy in textured mineral aggregates: theories and geological implications. In: S. Karato and M. Toriumi (Editors), *Rheology of Solid and of the Earth*. Oxford Univ. Press, New York, pp. 237-262.

Takeshita, T. and Wenk, H.-R., 1988. Plastic anisotropy and geometrical hardening in quartzites. *Tectonophysics*, 149: 345-361.

Takeshita, T. and Komatsu, M., 1990. Heat sources of high-temperature metamorphic belts in arc-trench systems: A case study of the Hidaka metamorphic belt. *Earth Monthly*, 12: 536-540 (in Japanese).

Takeshita, T. and Okudaira, T., 1994. Dynamics and thermal modeling in low-pressure / high-temperature metamorphic belts. *Zisin*, 47: 453-467 (in Japanese with English abstract).

Tatsumi, Y., 1995. *Subduction Zone Magmatism - A Contribution to Whole Mantle Dynamics*. University of Tokyo Press, Tokyo, 186pp. (in Japanese).

Thompson, A.B. and England, P.C., 1984. Pressure-temperature-time paths of regional metamorphism II: Their inference and interpretation using mineral assemblages in metamorphic rocks. *J. Petrology*, 25: 929-954.

Thompson, J.B. Jr., 1957. The graphical analysis of mineral assemblages in pelitic schists. *Amer. Mineral.*, 42: 842-858.

Toriumi, M., 1986. Mechanical segregation of garnet in synmetamorphic flow of pelitic schists. *J. Petrol.*, 27: 1359-1408.

Toyoshima, T. and Hara, I., 1989. Hidaka metamorphic belt as a deep-seated fracture zone, with special reference to intrusion mechanism of granitic rocks. *DELP Pub.*, 28: 85-91.

Toyoshima, T., Komatsu, M. and Shimura, T., 1994. Tectonic evolution of lower crustal rocks in an exposed magmatic arc section in the Hidaka metamorphic belt, Hokkaido, northern Japan. *The Island Arcs*, 3: 182-198.

Tracy, R.J., 1982. Compositional zoning and inclusions in metamorphic minerals. In: J.M. Ferry (Editor) *Characterization of Metamorphism through Mineral Equilibria. Rev. Mineral.*, 10: pp. 355-397.

Trépied, L., Doukhan, J.C. and Paquet, J., 1980. Subgrain boundaries in quartz: Theoretical analysis and microscopic observations. *Phys. Chem.. Metals*, 5: 201-218.

Tullis, J., Christie, J.M. and Griggs, D.T., 1973. Microstructures and preferred orientations of experimentally deformed quartzites. *Bull. Geol. Soc. Amer.*, 84: 297-314.

Turcotte, D.L. and Schubert, G., 1982. *Geodynamics*. John Wiley and Sons, New York, 435 pp.

Urai, J.L., Means, W.D. and Lister, G.S., 1986. Dynamic recrystallization in minerals. In: B.E. Hobbs and H.C. Heard (Editors), *Mineral and rock deformation: Laboratory studies*. Am. Geophys. Union, pp. 166-199.

Vance, D. and O'Nions, R.K., 1990. Isotopic chronometry of zoned garnets: growth kinetics and metamorphic histories. *Earth Planet. Sci. Lett.*, 97: 227-240.

Vernon, R.H., 1982. Isobaric cooling of two regional metamorphic complexes related to igneous intrusion in southeastern Australia. *Geology*, 10: 76-81.

Walther, J.V. and Orville, P.M., 1982. Volatile production and transport in regional metamorphism. *Contrib. Mineral. Petrol.*, 79: 252-257.

Walther, J.V. and Wood, B.J., 1984. Rate and mechanism in prograde metamorphism. *Contrib. Mineral. Petrol.*, 88: 246-259.

Weathers, M.S., Cooper, R.F., Kohlstedt, D.L. and Bird, J.M., 1979. Differential stress determined from deformation-induced microstructures of the Moine Thrust. *J. Geophys. Res.*, 84: 7495-7509.

Wells, P.R.A., 1980. Thermal models for the magmatic accretion and subsequent metamorphism of continental crust. *Earth Planet. Sci. Lett.*, 46: 253-265.

Wenk, H.-R., Canova, G., Molinari, A. and Kocks, U.F., 1989. Viscoplastic modeling of texture development in quartzite. *J. Geophys. Res.*, 94: 17895-17906.

Wickham, S.M. and Oxburgh, E.R., 1985. Continental rifts as a setting for regional metamorphism. *Nature*, 318: 330-333.

Wickham, S.M. and Oxburgh, E.R., 1987. Low-pressure regional metamorphism in the Pyrenees and its implications for the thermal evolution of rifted continental crust. *Trans. Roy. Soc. London*, A321: 219-242.

William, M.L. and Grambling, J.A.. 1990. Manganese, ferric ion, and the equilibrium between garnet and biotite. *Amer. Mineral.*, 75: 886-908.

Wood, B.J. and Walther, J.V., 1983. Rates of hydrothemal reactions. *Science*, 222: 413-415.

Yardley, B.W.D., 1977. An empirical study of diffusion in garnet. *Amer. Mineral.*, 62: 793-800.

Yardley, B.W.D., 1989. *An Introduction to Metamorphic Petrology*. Longman Scientific and Technical, Essex, England, 248pp.

Zwart, H.J., 1967. The duality of metamorphic belts. *Geol. Mijnbouw*, 46: 283-309.

参考論文

[1] Tectono-metamorphic processes of the Ryoke belt in the
Iwakuni-Yanai district, southwest Japan
(西南日本岩国－柳井地域領家帯の造構変成過程)
共著者 原 郁夫, 櫻井康博, 早坂康隆
地質学論集 42巻 91-120項 1993年4月 出版 (日本地質学会)

[2] 蛍光X線分析装置(Cr管球)による珪酸塩岩石中の微量元素の定量
共著者 早坂康隆, 星野健一, 池田圭一
地球科学 47巻 5号 439-444項 1993年 9月 出版 (地学団体研究会)

[3] 低圧高温型領家変成作用の熱モデル
共著者 原 郁夫, 竹下 徹
月刊地球 16巻 8号 486-489項 1995年 8月 出版 (海洋出版)

[4] Emplacement mechanism of the older Ryoke granites in the Yanai
district, southwest Japan, with special reference to extensional
deformation in the Ryoke metamorphic belt
(西南日本柳井地域領家変成帯における古期領家花崗岩類の貫入機構と
展張テクトニクス)
共著者 原 郁夫, 竹下 徹
Journal of Science of the Hiroshima university (Earth and Planetary
Science), vol.10, no.2, pp.357-366 1995年 2月 出版 (広島大学理学部出版)

[5] A new estimate of the transition conditions for transition from basal
<a> to prism [c] slip in naturally deformed quartz
(変形石英におけるbasal<a>からprism[c]すべりへの新しい転移温度見積り)
共著者 竹下 徹, 原 郁夫, 安東淳一
Tectonophysics1995年 出版予定 (Elsevier Science社)